# 外部場を利用した組織・構造制御無機材料の新機能発現と機構解明

（研究課題番号 25420709）

平成 25 年度~27 年度科学研究費補助金　（基盤（c））

研究成果報告書

平成 28 年 3 月

研究代表者　　中野裕美・教授
研究者番号 00319500

（豊橋技術科学大学　研究基盤センター）

# はしがき

本冊子は、平成 25 年度から 27 年度の 3 年間にわたり交付された、「**外部場を利用した組織・構造制御無機材料の新機能発現と機構解明**」を研究課題とする科学研究費補助金　基盤（c）（研究課題番号 25420709）の研究成果報告書である。

本研究は、外部場を効率的に利用することにより、原子レベルで構造・組織を制御した無機材料を創製し、新たな機能発現およびそれらの機能向上をめざす研究である。外部場としてはミリ波と高磁場を用い、ミリ波照射によるグリーンプロセッシング、高磁場中での粒子配向プロセッシングを活用した。得られた材料は、より機能向上のために、原子レベルでの組織・構造解析、XRD-リートベルト解析による構造解析、実験データを基にした第一原理計算等によるシミュレーション等により、正確に発現機構を解明し、そこから得られた新知見は材料設計にフィードバックし、学会、論文等で広く公表することができた。

平成 21 年 6 月に豊橋技術科学大学に赴任して以来､少しずつ研究環境を整え、この 3 年間は、環境・生命工学系の学生が少人数ではあるが当研究室に配属されるようになり、着実に研究を遂行することができた。また、次年度につながる興味深い研究シードも得ることができた有意義な研究期間となった。共同研究者の鈴木達博士、連携研究者の京都大学　馬渕守教授には多大なご助言、ご協力をいただいた。また、名古屋工業大学　福田功一郎教授、京都大学　袴田昌高准教授、産業技術総合研究所　湯浅元仁博士、大阪大学　三宅正司名誉教授、（有）MSP　佐治他三郎博士には、多方面からのご協力をいただいた。

今回もすてきな研究者の方々と出会い、ここに一定の成果をまとめられたことを心から喜び、深く感謝の意を表する。

平成 28 年 3 月吉日

豊橋技術科学大学
研究基盤センター
教授　中野裕美

**科学研究費補助金**　（基盤（c））

期間：平成 25 年度から 27 年度

研究課題番号：25420709

研究課題：**外部場を利用した組織・構造制御無機材料の新機能発現と機構解明**

研究目的

本研究は、外部場を効率的に利用することにより、原子レベルで構造・組織を制御した無機材料を創製し、新たな機能発現およびそれらの機能向上をめざす研究である。外部場としてはミリ波と高磁場を用い、ミリ波照射によるグリーンプロセッシング、高磁場中での粒子配向プロセッシングを活用する。得られた材料は、より機能向上のために、原子レベルでの組織・構造解析、XRD-リートベルト解析による構造解析、実験データを基にした第一原理計算等によるシミュレーション等により、正確に発現機構を解明し、得られた新知見は材料設計にフィードバックし、論文等で広く公表する。

研究代表者：中野裕美（豊橋技術科学大学　教授　研究者番号 00319500）

共同研究者　：　鈴木達　（物質・材料研究機構　主席研究員　研究者番号 50267407）

連携研究者　：　馬渕守　（京都大学　教授　研究者番号 00358061）

研究経費：　平成 25 年度　直接経費 1,900 千円　間接経費　570 千円

平成 26 年度　直接経費 1300 千円　間接経費　390 千円

平成 27 年度　直接経費　700 千円　間接経費　210 千円

総合計 5,070 千円（内　間接経費 1,170 千円）

**原著論文(査読付き)**

1. “Synthesis and Photoluminescence of New Phosphor $Ba_{0.79}Al_{10.9}O_{17.14}:Eu^{2+}$”, S. Furuya, A. Okuzumi, H. Nakano, *J. Soc. of Powder Tech., Jpn*. in press
2. “Decoupling grain growth from densification during sintering of oxide nano-particles”, Y. Kinemuchi, H. Nakano, K. Kato, K. Ozaki, K. Kobayashi, *RSC Advance*, in press
3. “Electron density distribution and disordered crystal structure of 12H-SiAlON, $SiAl_5O_2N_5$” H. Banno, T. Hanai, T. Asaka, K. Kimoto, H. Nakano, K. Fukuda, *Powder Diffr. J.*, in press.
4. “Enhancement of photoluminescence intensity and structural change by doping of $P^{5+}$ ion for $Ca_{2-x/2}(Si_{1-x}P_x)O_4:Eu^{2+}$ green phosphor”, S. Furuya, H.Nakano, N. Yokoyama, H. Banno, K. Fukuda, *J. Alloys and Compd.* Vol. 658, pp.147-151 (2016).
5. “Crystal structures and enhancement of photoluminescence intensities by effective doping for lithium tantalate phosphors”, H. Ichioka, S.Furuya, T. Asaka, H. Nakano, and K. Fukuda, *Powder Diffr. J.*, Vol. 30(4), pp. 326-332 (2015).
6. “Microstructural comparison between Nb- and Ta-systems in $Li_{1+x-y}M_{1-x-3y}Ti_{x+4y}O_3$ (M = $Nb^{5+}$, $Ta^{5+}$) solid solution with superstructure” H. Nakano, S. Suehiro, S. Furuya, K. Fukuda, *J. Alloy. Compd.*, Vol. 618, pp. 504-507 (2015).
7. “Extraordinary diffusion in Co/Cu grain boundaries” H. Nakano, M. Yuasa, H. Miyamoto, N. Miyazawa, M. Mabuchi, *Scripta Mater.*, Vol. 101, pp. 52-55 (2015).
8. “Synthesis and structural analysis of $Li_{1+x-y}M_{1-x-3y}Ti_{x+4y}O_3$ (M: Ta, Nb) solid solutions with superstructure” S. Suehiro, H. Nakano, *J. Soc. Powder. Tech., Jpn.*, Vol. 51 (3), pp. 136-141 (2014).
9. “Synthesis and luminescence enhancement of $Eu^{3+}$, $Sm^{3+}$ co-doped $Li_{1.11}Ta_{0.89}Ti_{0.11}O_3$ phosphor” H. Nakano, S. Furuya, K. Fukuda, S. Yamada, *Mater. Res. Bull.*, Vol. 60, pp. 766-770 (2014).
10. “{10-12} twins in rolled Mg-Zn-Ca alloy with high formability” H. Nakano, M. Yuasa, M. Mabuchi, Y. Chino, *J. Mater. Res.*, Vol. 29 (24), pp. 3024-3031 (2014).
11. “Twinning behavior of AZ31 Mg alloy alternately compressed in two orthogonal directions” H. Kwon, H. Nakano, M. Mabuchi, Y. Chino, *Philosophical Magazine*, Vol. 94 (34), pp. 3960-3977 (2014).
12. “Preparation of textured $Li_{1+x-y}Nb_{1-x-3y}Ti_{x+4y}O_3$ solid solution in a high magnetic field”, H. Nakano, S. Suehiro, T. S. Suzuki, *Materials Science Forum* Vols. 783-786 (2014) pp. 2480-2484.

13. “Synthesis of a rare-earth doped LNT (Li-Nb-Ti-O) phosphor by millimeter-wave heating” H. Nakano, S. Suehiro, T. Saji, and S. Miyake, *J. Alloy. Compd.*, Vol. 552, pp. 475-479(2013).
14. “Crystal Structure and Oxide-Ion Diffusion of Nano-Crystalline, Compositionally Homogeneous Ceria-Zirconia $Ce_{0.5}Zr_{0.5}O_2$ up to 1176 K” M. Yashima, T. Sekikawa, D. Sato, H. Nakano, K. Omoto, *Cryst. Growth Des.*, Vol. 13 (2), pp. 829–837 (2013).
15. “Rapid synthesis of $Eu^{3+}$-doped LNT (Li-Nb-Ti-O) phosphor by millimeter-wave heating” H. Nakano, K. Ozono, T. Saji, S. Miyake, H. Hayashi, *Opt. Mater.*, Vol. 35, pp. 2045-2048 (2013).
16. “Microstructural Behavior of γ-$Fe_2O_3$ Formation in Reactions between Layered Iron Oxychloride and Sodium n-Pentoxide” T. Shiono, F. Tando, H. Nakano, Y. Sugahara , *Solid State Sci.*, Vol. 19, pp. 156-161 (2013).
17. “Synthesis of new $RE^{3+}$ doped $Li_{1+x}Ta_{1-x}Ti_xO_3$ (RE: Eu, Sm, Er, Tm, and Dy) phosphors with various emission colors” H. Nakano, S. Suehiro, S. Furuya, H. Hayashi, S. Fujihara, *Materials*, Vol. 6, pp. 2768-2776 (2013).
18. “Softening due to disordered grain boundaries in nanocrystalline Co” M. Yuasa, M. Hakamada, H. Nakano, M. Mabuchi, Y. Chino, *J. Phys.: Condens. Matter*, Vol. 25(34), pp. 345702 (1)-(10) (2013).
19. “Syntheses and crystal structures of $Li(Ta_{0.89}Ti_{0.11})O_{2.945}$ and $(Li_{0.977}Eu_{0.023})(Ta_{0.89}Ti_{0.11})O_{2.968}$” T. Uchida, S. Suehiro, T. Asaka, H. Nakano, K. Fukuda, *Powder Diffr. J.*, Vol. 28 (3), pp. 178-183 (2013).
20. “Crystal Structure, Optical Properties and Electronic Structure of Novel Calcium Strontium Tungsten Oxynitrides $Ca_xSr_{1-x}WO_2N$” M. Yashima, U. Fumi, H. Nakano, K. Omoto, J. Hester, *J. Phys. Chem. C*, Vol. 117 (36), pp. 18529-18539 (2013).

国際会議発表

21. “Effect of heat treatment on crystal structure and photoluminescence of$(Ca_{2-x/2-y}Eu_y)(Si_{1-x}P_x)O_4$ phosphor”, N. Yokoyama, S. Furuya, H. Nakano, H., Banno, K. Fukuda, *IGNITE2016*, Jan 27-29, Penang, Malaysia, (2016).
22. “Influence of $Pr^{3+}$ co-doping on photoluminescence intensity of $Li_{1.11}Ta_{0.89}Ti_{0.11}O_3$:$Eu^{3+}$ phosphor”, S. Furuya, N. Yokoyama, H. Nakano, S. Fujihara, *The 11th Pacific Rim Conference of Ceramic Societies*,Aug. 30-Sep. 4, (2015), Jeju, Korea.

23. "Synthesis of $Ca_{2-x/2}(Si_{1-x}P_x)O_4:Eu^{2+}$ green phosphor and influence of $P^{4+}$ ion on luminescence intensity", S. Furuya, N. Yokoyama, H. Nakano, H., Banno, K. Fukuda, *The 11th Pacific Rim Conference of Ceramic Societies*,Aug. 30-Sep.4, (2015), Jeju, Korea.
24. "Fabrication of *c*-axis oriented $Li_{1+x-y}Nb_{1-x-3y}Ti_{x+4y}O_3$ solid solution by slip casting in a high magnetic field", H. Nakano, S.Furuya, T.S. Suzuki, S. Osato, *ICCCI2015*, Kurashiki, July 8-10 (2015).
25. "Synthesis and luminescence property of $RE^{3+}$doped $Li_{1.11}(Ta_{1-z}Nb_z)_{0.89}Ti_{0.11}O_3$ ($0 \leq z \leq 1.0$, *RE*: Sm, Dy, Tm or Er) phosphor", S. Furuya, H. Nakano, H. Hayashi, S.Yamada, *K-J ceramics 31*, Changwon, Korea, 11/26-29 (2014)CD.
26. "Synthesis and luminescence property of $Li_{1.11}Ta_{0.89}Ti_{0.11}O_3$: $Eu^{3+}$, $Sm^{3+}$ red phosphor", H. Nakano, Syohei Furuya, Suzuya Yamada、*K-J ceramics 31*, Changwon, Korea, 11/26-29 (2014) CD.
27. **[Invite]** "Nanoscale phenomena by *in-situ* TEM observation", H. Nakano, *ELECTROCERAM XIV*, Bucharest, Jun 16-20, (2014) CD.
28. "Synthesis of *c*-axis oriented LNT(Li-Nb-Ti-O)solid solution for anisotropic electric property", S. Suehiro, H. Nakano, T. Suzuki, *ELECTROCERAM XIV*, Bucharest, Jun 16-20, (2014) CD.
29. **[Invite]** "Preparation of textured $LiNbTiO_3$ solid solution in a high magnetic field and sintering by millimeter-wave heating", H, Nakano, S.Shiho, T. Susuki, T. Saji, S. Miyake, Intl' Conf. on Processing and manufacturing of advanced materials (THERMEC), 3-12, Dec 2~8, Rio Hotel, Las Vegas, USA (2013), pp 441-442.
30. "Preparation of oriented $Li_{1+x-y}Nb_{1-x-3y}Ti_{x+4y}O_3$ solid solution with superstructure by slip casting in a high magnetic field" H. Nakano, S. Suehiro, T. S. Suzuki, Y. Sakka, *ECERS2013*, Limoges, France, (2013) CD.
31. "Synthesis and structural analysis of $Li_2O$-$Ta_2O_5$-$TiO_2$ (LTT) phosphor", S. Suehiro, H. Nakano, T. Uchida, T. Asaka, and K. Fukuda, *ECERS2013*, Limoges, Franc, Jun23-27, (2013) CD.
32. "Preparation of oriented $Li_{1+x-y}Nb_{1-x-3y}Ti_{x+4y}O_3$ solid solution with superstructure by slip casting in a high magnetic field", H. Nakano, S. Suehiro, Tohru S. Suzuki and Yoshio Sakka, *ECERS2013*, Limoges, Franc, Jun23-27, (2013) CD.
33. "Synthesis, structure analysis and magnetic properties of $Sr_xLa_{1-x}MnTrO_6$ solid solution", N. Kamegashira, Md. Tahidul Haque, H. Satoh, H. Nakano, *ECERS2013*, Limoges, Franc, Jun23-27, (2013) CD.

34. “Microstructure and Mechanical Properties of Nanostructured Co-Cu Alloy Films Processed by Electrodeposition” M. Yuasa, H. Nakano, M. Mabuchi, *Journal of Physics: Conference Series*, Vol. 417, 012064 (pp.5) (2013).

**国内学会発表**

35. 組成・構造制御によるBa-Al-O系新蛍光体材料の合成，古谷彰平，奥住明日香，楠美智子，林裕之，中野裕美，日本セラミックス協会年会，早稲田大学，3/14-16 (2016).
36. 錯体重合法を用いた$Zn_2Ti_xSn_{1-x}O_4$:Eu ($0 \leq x \leq 1$) 蛍光体の合成，平靖之，中村稀星，寺澤みゆり，中野裕美，日本セラミックス協会，早稲田大学，3/14-16 (2016).
37. シリケート蛍光体 $(Ca_{2-x/2-y}Eu_y\square_{x/2})(Si_{1-x}P_x)O_4$の結晶構造制御と緑色発光強度， 横山宣幸，古谷彰平，中野裕美，坂野広樹，福田功一郎，日本セラミックス協会東海支部学術研究発表会，名古屋大学，12/12 (2015).
38. 組成制御によるBa-Al-O系新蛍光体材料の合成と評価，奥住明日香，古谷彰平，中野裕美，粉体工学会秋期研究発表会，大阪南港ATC，10/13-14，(2015) pp.44-45.
39. *c*-軸配向$Si_3N_4$セラミックスの異方的な焼結収縮挙動と微構造発達，高橋 拓実，多々見 純一，田中 諭，中野 裕美，日本セラミックス協会秋季シンポジウム，富山大学 9/16-18 (2015)，3A05.
40. 緑色発光シリケート蛍光体 $(Ca_{2-x/2}(Si_{1-x}P_x)O_4$: $Eu^{2+})$ の$P^{5+}$イオン添加による発光強度向上と結晶構造変化，横山宣幸，古谷彰平，中野裕美，坂野広樹，福田功一郎，日本セラミックス協会秋季シンポジウム，富山大学，9/16-18 (2015) 1PL01.
41. 近紫外及び青色励起$Li_{1.11}Ta_{0.89}Ti_{0.11}O_3$:$Eu^{3+}$ 赤色蛍光体の$Sm^{3+}$恭添加による発光強度向上とそのメカニズム，古谷彰平，中野裕美，林裕之，福田功一郎，セラミック材料部門委員会学術講演会，京都工芸繊維大学， 7/14 (2015) pp.21-22.
42. 共沈法を用いた$Zn_2Ti_xSn_{1-x}O_4$:Eu ($o < x < 1$) 蛍光体の合成，平靖之，三村和仙，中野裕美，セラミック材料部門委員会学術講演会，京都工芸繊維大学 7/14 (2015) pp. 17-18.
43. 超構造を形成するLi- (M, Sb)-Ti-O（M: Nb, Ta）系固溶体と赤色蛍光体の合成，末廣志穂，古谷彰平，中野裕美，林裕之，日本セラミックス協会年会 岡山大学， 3/18-20 ，(2015) 1P065.
44. 近紫外線励起赤色蛍光体Li $Ta_{0.89}Ti_{0.11}O_{2.945}$:$Sm^{3+}$のMgO 添加による 発光特性の向上と結晶構造，市岡裕晃，古谷彰平，中野裕美，浅香透，福田功一郎，中野裕美，日本セラミックス協会年会，岡山大学 3/18-20（2015）1P062.

45. 液相法を用いた$Zn_2Ti_xSn_{1-x}O_4$:Eu（0＜$x$ ＜1）蛍光体の合成，平靖之，三村和仙，中村稀星，鈴木瞭汰，中野裕美， 日本セラミックス協会年会，岡山大学， 3/18-20（2015）1L21.
46. 赤色蛍光体$Li_{1.11}Ta_{0.89}Ti_{0.11}$:$Eu^{3+}$の共添加($Sm^{3+}$ or $Pr^{3+}$)による発光強度向上，古谷彰平，横山宣幸， 中野裕美，林裕之，山田鈴弥，日本セラミックス協会，東海支部学術講演会，名工大，12/6 (2014) p.3.
47. 近紫外励起 Li-Ta-Ti-O 系赤色蛍光体の $Sm^{3+}$共添加による発光強度向上，古谷彰平，中野裕美，福田功一郎，山田鈴弥，日本セラミックス協会秋季シンポジウム，鹿児島大学，9/9-11 (2014) 1PE01.
48. 近紫外線励起赤色蛍光体 Li（$Ta_{1-x}Ti_x$）$O_{3-x/2}$:$Eu^{3+}$（ $x$ = 0, 0.11, 0.25） の電子密度分布と結晶構造，発光特性，市岡裕晃，古谷彰平，中野裕美，浅香透，福田功一郎，日本セラミックス協会年会，慶応大，3/17-19 (2014) 1P181.
49. 高配向 LNT セラミックス作製のための粉砕条件の検討，末廣志穂，中野裕美，武田忠彦, 木村善衛, 鈴木達, 目義雄, 日本セラミックス協会年会, 慶応大, 3/17-19 (2014) 1P105.
50. $c$ 軸配向 $Si_3N_4$ セラミックスの焼結収縮と粒成長の異方性， 高橋拓実，多々見純一，田中諭，中野裕美，日本セラミックス協会年会，慶応大，3/17-19 (2014) 2G09.
51. 蛍光体セラミックスのミリ波加熱法による低温短時間合成に関する研究，中野裕美，佐治他三郎，三宅正司，第５２回セラミックス基礎科学討論会，ウインクあいち，1/9-10 (2014) p.239.
52. Li-M-Ti-O (M:Nb,Ta)系固溶体を母体とした近紫外励起蛍光体の合成，古谷彰平，末廣志穂, 中野裕美, 林裕之, 山田鈴弥, 日本セラミックス協会東海支部学術研究発表会、名城大，12/7（2013）p. 83.
53. 近紫外励起用蛍光体の発光特性に及ぼす MgO 添加効果， 古谷彰平，末廣志穂，中野裕美，林裕之，山田鈴弥，第 26 回秋季シンポジウム，信州大学 9/4-6 (2013) 1PB01.
54. 構造制御された Li-M-Ti-O 系（M:Ta, Nb） 固溶体の合成と構造解析，中野裕美，末廣志穂，第４９回夏期シンポジウム 7/18-19 ホテルマウント富士，(2013) P.8.
55. ペロブスカイト型混合伝導体 $PrBa_{1-x}Sr_xCo_2O_{6-\delta}$（0 < $x$ < 1）における Sr 濃度 $x$ による陽イオン規則度と結晶構造の制御，北川恵美，チンイジン，史宇飛，尾本和樹，藤井孝太郎，八島正知，James Hester，中野裕美， 日本セラミックス協会年会，東工大，3/17-19 (2013) 2K08.

56. ナノセリア―ジルコニア $Ce_{0.5}Zr_{0.5}O_2$ の結晶構造変化と酸素拡散，八島正和，関川和宏, 佐藤大祐, 尾本和樹, 中野裕美, 日本セラミックス協会年会, 東工大, 3/17-19 (2013) 2K04

57. Li-M-Ti-O (M:Nb or Ta)系蛍光体の合成と RGB 色の発光強度比較，末廣志穂，中野裕美，林裕之，山田鈴弥，藤原忍，日本セラミックス協会年会，東工大，3/17-19 (2013) 1P079.

58. 近紫外線励起赤色蛍光体 $Li(Ta_{0.89}Ti_{0.11})O_{2.945}:Eu^{3+}$ の電子密度分布と結晶構造，内田 智裕，末廣 志穂，中野 裕美，浅香　透，福田 功一郎，日本セラミックス協会年会，東工大，3/17-19 (2013) 1K22.

59. ナトリウムを内包したソーダライト型アルミノゲルマニウム酸塩の合成，平靖之，矢吹渓, 五十嵐睦夫, 中野裕美, 日本セラミックス協会年会, 東工大, 3/17-19 (2013) 1P194.

60. 反応拡散による結晶配向セラミックスの新規作製方法, 内田智裕, 中野裕美, 浅香透, 福田功一郎，　日本セラミックス協会年会，東工大，3/17-19 (2013) 1P218.

**招待講演**

61. EMAP 研究会 20 周年　大阪大学　(2016.3.18)
タイトル：ミリ波加熱法によるセラミックス蛍光体合成への応用と課題

62. 若手研究者・技術者を対象とした工場見学および交流会　化学工業会東海支部主催 (2016.2.19)
タイトル：研究は正確な観察・解析からはじまる～研究と家庭の両立のための工夫～

63. 東三河産官学交流サロン,アークリッシュホテル（豊橋）　(2016.01.19)
タイトル：新規蛍光体材料技術とダイバーシティ社会に向けて

64. 大学院エネルギー科学研究科講演会　　京都大学にて　(2016.12.11)
タイトル：ダイバーシティ社会に向けて

65. 技術情報協会主催　技術セミナーにて　(2015.01.23)
タイトル：高演色性のためのセラミックス蛍光体の創成

66. 愛知の大学　学びフォーラム　愛知大学にて(2015.08.05)
タイトル：リケジョのススメ~研究っておもしろい～

67. 京都大学資源エネルギーシステム学研究室　特別講演　(2014.12.12)
タイトル：TEM の基礎

68. ElectroceramicsXIV (ルーマニア、ブカレスト) にて招待講演(2014.6.16～20)
タイトル：Nanoscale phenomena by in-situ TEM observation

69. 第 52 回セラミックス基礎科学討論会にて，名古屋 (2014.1.9～10)
タイトル：蛍光体セラミックスのミリ波加熱法による低温短時間合成に関する研究
70. Thermec 2013 にて,ラスベガス (2013.12.2～6）
タイトル：Preparation of textured Li-Nb-Ti-O solid solution in high magnetic field and sintering by millimeter-wave heating
71. 稲沢市成人大学　講演　(2013.10.04)
タイトル：ミクロの世界の不思議を見てみよう
72. 京都大学資源エネルギーシステム学研究室　特別講演　(2013.09.09)
タイトル：TEM 観察からわかる微構造と物性の関係

**著書、解説等**

73. "新版　入門機器分析化学"　編著者，　庄野利之脇田久伸ほか，三共出版（株）中野 11.2 章担当　（2015 年　12 月）
74. "白色ＬＥＤ用近紫外励起赤色蛍光体の創成と母体構造の特徴"　中野裕美、福田功一郎、ケミカルエンジニアリング、12 月号（2014)1～5.

**研究グループ受賞**

75. 平成 28 年 Best Poster Award　IGNITE2016
Effect of heat treatment on crystal structure and photoluminescence of $(Ca_{2-x/2-y}Eu_y)(Si_{1-x}P_x)O_4$ phosphor, N. Yokoyama, S. Furuya, H. Nakano, H. Banno, K. Fukuda, Penang, Malaysia,1/27-29
76. 平成 27 年ベストポスター賞　粉体工学会
組成制御による Ba-Al-O 系新蛍光体材料の合成と評価，奥住明日香，古谷彰平，中野裕美，粉体工学会秋期研究発表会，大阪南港 ATC，10/13-14
77. 平成 26 年若手優秀ポスター賞 ハイブリッド材料研究会
近紫外励起 Li-Ta-Ti-O 系赤色蛍光体の $Sm^{3+}$共添加による発光強度向上，古谷彰平，中野裕美，福田功一郎，山田鈴弥，日本セラミックス協会秋季シンポジウム，鹿児島大学，9/9-11

Li-(Nb,Ta)-Ti-O 系酸化物の研究論文

ミリ波、磁場による外部場活用他

Journal of Alloys and Compounds 552 (2013) 475–479

Contents lists available at SciVerse ScienceDirect

Journal of Alloys and Compounds

journal homepage: www.elsevier.com/locate/jalcom

# Synthesis of a rare-earth doped LNT (Li–Nb–Ti–O) phosphor by millimeter-wave heating

Hiromi Nakano [a,*], Shiho Suehiro [a], Tasaburo Saji [b], Syoji Miyake [b]

[a] Toyohashi University of Technology, Tempaku, Toyohashi 441-8580, Japan
[b] MSP Corp., Takaida, Higashiosaka 577-0053, Japan

ARTICLE INFO

*Article history:*
Received 5 October 2012
Received in revised form 6 November 2012
Accepted 10 November 2012
Available online 19 November 2012

*Keywords:*
Sintering
Phosphors
Luminescence
X-ray diffraction
SEM

ABSTRACT

Phosphors based on the $Li_{1+x-y}Nb_{1-x-3y}Ti_{x+4y}O_3$ (LNT, $0.05 \leqslant x \leqslant 0.25$, $y = 0$) solid solution as host material that emit with bright red, green and blue (RGB) colors have been investigated. Rare-earth (RE)-doped LNT phosphors ($RE^{3+}$: Eu, Sm, Er, Tm) are traditionally prepared by sintering at 1373 K in a conventional electric furnace (EF) for 24 h. However, a fast synthetic technique that uses less energy is required to improve the applicability of these materials. In the present study, LNT:$RE^{3+}$ phosphors were successfully synthesized by millimeter-wave (MM) heating at 1173 K for only 1 h. Bright RGB color emissions were obtained, with LNT:$Eu^{3+}$ and LNT:$Sm^{3+}$ exhibiting red emission, LNT:$Tm^{3+}$ blue emission and LNT:$Er^{3+}$ green emission. The highest photoluminescence (PL) intensity, which was achieved for the composition $Li_{1.11}Nb_{0.85}Ti_{0.11}O_3$ doped with 2.5 wt.% of $(RE)_2O_3$, was almost equivalent to that of the specimen obtained upon EF heating.



## 1. Introduction

In the ternary $Li_2O$–$Nb_2O_5$–$TiO_2$ system, $Li_{1+x-y}Nb_{1-x-3y}Ti_{x+4y}O_3$ ($0.11 \leqslant x \leqslant 0.33$, $0 \leqslant y \leqslant 0.09$) (LNT) forms with a superstructure, and this is known as the M-phase. Since the discovery of the M-phase by Castrejon et al. [1,2], such structures have been investigated [3–6]. The superstructure of the M-phase is formed by periodical insertion of the intergrowth layer in the matrix having a trigonal structure. The relationship between dielectric property and period of the intergrowth layer of the M-phase has been studied [7,8]. Application of the unique structure as a host material of the phosphor, new phosphors have been investigated based on the LNT or related structure by a conventional electric furnace [9–11]. A homogeneous material was, however, synthesized at 1373 K for 24 h after calcination at 1273 K for 3 h. A fast synthesizing technique that uses lower energy is required for application of this material. Heating by millimeter-wave (MM) radiation has certain advantages in industrial processes or applications from the viewpoints of the homogeneity of large materials, control of grain growth, and densification at low temperature [12]. So, we have succeeded in synthesizing LNT solid solution having a superstructure by millimeter-wave heating for only 1 h above 1173 K [13].

In this time, the $RE^{3+}$-doped LNT phosphor was synthesized by MM radiation at 1173 K for 1 h. As a result, the PL intensity was almost equivalent to that of the specimen obtained upon electric furnace heating.

* Corresponding author. Tel.: +81 532 44 6606; fax: +81 532 44 6610.
*E-mail address:* hiromi@crfc.tut.ac.jp (H. Nakano).

0925-8388/$ - see front matter © 2012 Elsevier B.V. All rights reserved.
http://dx.doi.org/10.1016/j.jallcom.2012.11.058

## 2. Experimental procedure

The starting materials used were $Li_2CO_3$, $Nb_2O_5$ and $TiO_2$ (>99.9% grade) to prepare the solid solution of LNT. The compositions of the LNT solid solutions prepared in this work followed the formula $Li_{1+x-y}Nb_{1-x-3y}Ti_{x+4y}O_3$ with $0.05 \leqslant x \leqslant 0.25$, $y = 0$. The $TiO_2$ content of the specimens was varied from 5 to 20 mol%. The powders were mixed and pressed in air at 1173 K or 1273 K for 1 h by millimeter-wave heating. The millimeter-wave heating equipment consists of a 24 GHz gyrotron millimeter-wave generator and a multi-mode chamber (MSP Corp., Japan). The specimens were surrounded by a heat insulator, and their temperature was measured with a thermocouple placed near the specimens. The total number of specimens in the MM chamber was the same each time. The electric power (intensity of the electric-field) is an important factor in the MM heating technique, and the optimal electric power was controlled about 2.5 kW for synthesis of the present phosphor materials. The heating rate was approximately 30 K/min, and the specimen was cooled down in the chamber after sintering. As s comparison material, the mixed powders were also sintered at 1273 K for 3 h and 1373 K for 24 h in a conventional electric furnace (EF).

Structural analysis was carried out by X-ray diffraction (XRD) using a RINT 2500 (Rigaku Co., Ltd., Japan) operating at 40 kV and 200 mA. Microstructure images were observed by a scanning electron microscope (SEM) (SU8000, Hitachi Co., Ltd., Japan) operating at 3 kV. High-resolution TEM (HRTEM) images were observed by a device (2100 F, JEOL Co., Ltd., Japan) operating at 200 kV and equipped with energy-dispersed spectroscopy (EDS).

Excitation and emission spectra of the sintered samples were measured by a spectrometer (model FP-6500, JASCO).

## 3. Results and discussion

The intensity of an electric field is an important factor in the MM heating technique [13]. The intensity of the electric-field in the applicator is in proportion to the millimeter-wave electric power. The electric power could be controlled by the thickness of

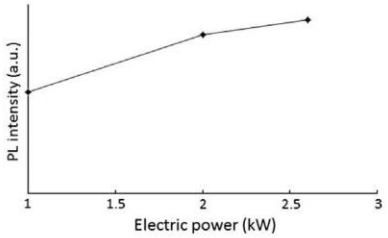


**Fig. 1.** Relationship between millimeter-wave electric power (intensity of electric field) and the PL intensity of $Li_{1.25}Nb_{0.75}Ti_{0.25}O_3$:$Eu^{3+}$.

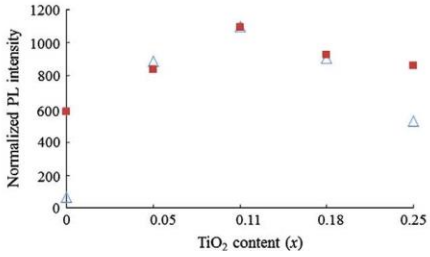


**Fig. 2.** Relationship between PL intensity and $TiO_2$ content in the $Li_{1+x}Nb_{1-x}Ti_xO_3$ host material. Triangle: heating at 1173 K for 1 h by MM heating; square: heating at 1273 K for 3 h and 1373 K for 24 h by EF heating.

a heat insulator surrounding the specimen. As the first step in this work, the phosphor of $Li_{1.25}Nb_{0.75}Ti_{0.25}O_3$ ($x = 0.25$, $y = 0$) was synthesized using various electric powers at 1173 K for 1 h. Fig. 1 shows the relationship between millimeter-wave electric power (intensity of electric field) and the PL intensity of $Li_{1.25}Nb_{0.75}Ti_{0.25}O_3$:$Eu^{3+}$. At above 3 kW, the specimen melted and the phosphor's surface became glassy. The result revealed that the intensity of the electric-field affect the sintering of the phosphor. The optimal electric furnace was found to be about 2.5 kW for synthesis of the above phosphor materials. The effect of the electric field in synthesis by MM heating, the so-called "non-thermal effect", can be explained as activity on the ceramic's surface caused by irradiation of electromagnetic waves [12,13]. In general, rare-earth oxides, with the exceptions of $CeO_{2-x}$ and $Tb_2O_3$, do not easily absorb microwave or millimeter-wave energies [12]. By controlling the millimeter-wave electric power, we could successfully apply this technique to the synthesis of materials containing rare-earth ions.

The optimal $TiO_2$ concentrations were determined for the LNT:$Eu^{3+}$ phosphor synthesized at 1173 for 1 h by MM heating. The phosphor was also prepared by sintering at 1273 K for 3 h and 1373 K for 24 h in a conventional electric furnace (EF). Red emission of the $Eu^{3+}$-doped LNT was observed upon excitation at a wavelength of 398 nm due to an intraconfigurational $^7F_0$–$^5L_6$ transition. The maximum emission peak at around 625 nm is associated with the hypersensitive electric-dipole $^5D_0$–$^7F_2$ transition in the $Eu^{3+}$ ion. The optimal $TiO_2$ concentration was then determined at the maximum emission peak upon excitation at around 398 nm [9]. Fig. 2 shows the relationship between PL intensity and $TiO_2$ content at a fixed $Eu_2O_3$ concentration of 2.5 wt.%. The optimal $Eu_2O_3$ concentration was found to be 2.5 wt.% in terms of the PL intensity [9]. The resulting LNT phosphor with composition $Li_{1.11}Nb_{0.89}Ti_{0.11}O_3$ ($x = 0.11$, $y = 0$) was found to have the highest PL intensity. This intensity was clearly improved by the addition of $TiO_2$, which could affect the coordination state of the $Eu^{3+}$ ion and/or induce a structural distortion around this ion [10,11].

Fig. 3 shows the XRD patterns for the superstructure-containing LNT at 1173 K for 1 h (a) and for the LNT:$Eu^{3+}$ phosphors synthesized at 1173 K for 1 h (b) and at 1273 K for 1 h (c). In Fig. 3(a), the superstructure formed as satellite peaks around the (012) peak. The periods of the satellite reflections increase with increasing Ti content. TEM image also showed that the $Li_{1.25}Nb_{0.75}Ti_{0.25}O_3$ with no $Eu^{3+}$ ion had the superstructure homogeneously at 1173 K for 1 h (see Fig. 4(a)). The superstructure is formed by periodical insertion of the intergrowth layer in the matrix. The superstructure was disturbed by the dispersion of $Eu^{3+}$ ion into the LNT host material. After MM heating at 1173 K, the superstructure in the $Li_{1.25}Nb_{0.75}Ti_{0.25}O_3$ ($x = 0.25$, $y = 0$) host material was only partially formed, as shown in Fig. 3(b) and Fig. 4(b). In contrast, no satellite reflection was observed after heating to 1273 K, even in the $Li_{1.25}Nb_{0.75}Ti_{0.25}O_3$ host material (see Fig. 3(c)). Thus, the PL intensity for the phosphor synthesized at 1173 K was almost identical to that for its counterpart synthesized at 1273 K, although their structures differed slightly. These findings suggest that the $Eu^{3+}$ ion is dispersed into the LNT host material during the early stages of MM irradiation at 1273 K, thereby preventing the intergrowth layer from forming in the matrix. They also suggest that the PL intensity is related to the $TiO_2$ content rather than the presence of a superstructure in the host material. This change in the crystal structure was also investigated by SEM. The grain morphology of the LNT containing the superstructure was found to be plate-like and to form during the grain-growth process over a long time period [11], as shown in Fig. 5(a). Doping with $Eu^{3+}$ ions resulted in a change in the grain morphology of the LNT:$Eu^{3+}$ to spherical (see Fig. 5(b) and (c)). The fact that the grains of this phosphor grew upon MM heating at 1173 K for only 1 h suggests that this

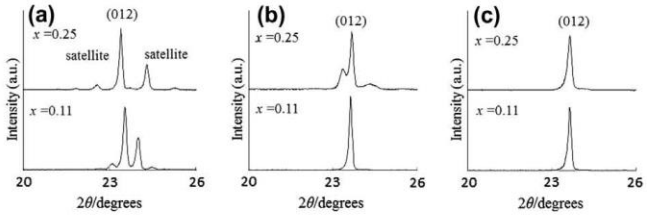


**Fig. 3.** XRD patterns of $L_{1+x}Nb_{1-x}Ti_xO_3$ ($x = 0.11$ and 0.25) with non-dope $Eu^{3+}$ at 1173 K for 1 h (a), LNT:$Eu^{3+}$ synthesized at 1173 K for 1 h (b) and LNT:$Eu^{3+}$ synthesized at 1273 K for 1 h (c).

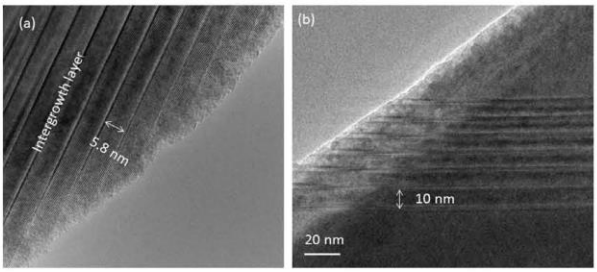


**Fig. 4.** TEM images of $Li_{1.25}Nb_{0.75}Ti_{0.25}O_3$ at 1173 K for 1 h (a) and $Li_{1.25}Nb_{0.75}Ti_{0.25}O_3:Eu^{3+}$ at 1173 K for 1 h (b).

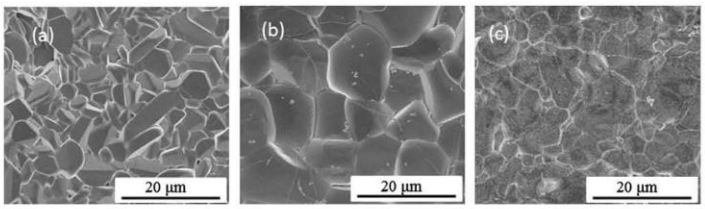


**Fig. 5.** Morphologies of LNT with non-dope $Eu^{3+}$ (a), LNT:$Eu^{3+}$ formed by EF heating (b) and LNT:$Eu^{3+}$ formed by MM heating (c).

technique can be considered to be a highly efficient for the formation of LNT:$RE^{3+}$ phosphors, as reported previously [14].

Fig. 6 shows the XRD patterns for $Li_{1.11}Nb_{0.89}Ti_{0.11}O_3$ doped with 2.5 wt.% $(RE)_2O_3$ synthesized by MM heating at 1173 K for 1 h (a) and EF heating at 1273 K for 3 h and 1373 K for 24 h (b). All structures were found to be trigonal ($R3c$). Furthermore, no secondary phases were detected in the LNT:$RE^{3+}$ synthesized by MM heating for even only 1 h. This finding suggests that the rare-earth is completely doped as an activator in the host material and may occupy both the octahedral $Li^+$ and $Nb^{5+}$ sites in the host structure [14,15].

Fig. 7 shows the excitation and emission spectra of LNT:$RE^{3+}$. Red emission was also observed for the $Sm^{3+}$-doped LNT upon excitation at 410 nm due to the $^6H_{5/2}$–$^6P_{3/2}$ transition. Upon excitation at 410 nm, the photoluminescence spectra showed emission peaks at 568 ($^4G_{5/2}$–$^6H5_{/2}$) and 609 nm ($^4G_{5/2}$–$^6H_{7/2}$), with an intense red emission at 651 nm ($^4G_{5/2}$–$^6H_{9/2}$, see Fig. 7(b)). A green emission peak at 526 nm ($^4S_{3/2}$–$^4I_{15/2}$) was observed for LNT:$Er^{3+}$ upon excitation at 551 nm ($^4I_{15/2}$–$^2H_{11/2}$, Fig. 7(c)). Likewise, bright blue emission was observed at 359 nm ($^1D_2$–$^3F_4$ transition) for the LNT:$Tm^{3+}$ phosphor upon excitation at 462 nm ($^3H_6$–$^1D_2$, Fig. 7(d)). These maximum PL intensities were compared for

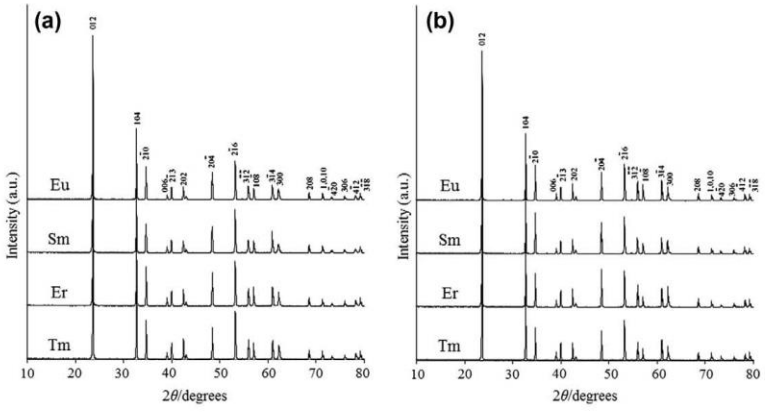


**Fig. 6.** XRD patterns for $L_{1.11}Nb_{0.89}Ti_{0.11}O_3:RE^{3+}$ synthesized at 1173 K for 1 h by MM heating (a) and at 1273 K for 3 h and 1373 K for 24 h by EF heating (b).

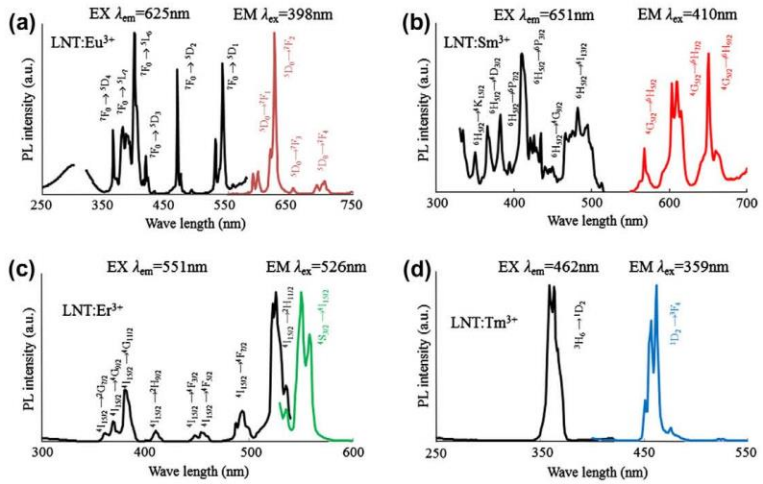


**Fig. 7.** Excitation and emission spectra of $L_{1.11}Nb_{0.89}Ti_{0.11}O_3$:$RE^{3+}$ ($RE^{3+}$: Eu, Sm, Er, Tm) by MM heating at 1173 K for 1 h.

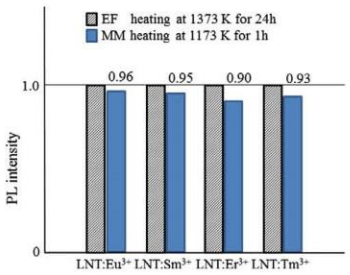


**Fig. 8.** Comparison of PL intensity for the phosphors between EF heating at 1273 K for 3 h and 1373 K for 24 h and MM heating at 1173 K for 1 h.

**Table 1**
Chromaticity ($x$, $y$) of LNT:$RE^{3+}$.

| RE | EF heating | | MM heating | |
|---|---|---|---|---|
| | $x$ | $y$ | $x$ | $y$ |
| Eu | 0.674 | 0.326 | 0.675 | 0.325 |
| Sm | 0.631 | 0.369 | 0.631 | 0.369 |
| Er | 0.316 | 0.677 | 0.322 | 0.671 |
| Tm | 0.142 | 0.038 | 0.150 | 0.052 |

phosphors synthesized by EF heating at 1273 K for 3 h and 1373 K for 24 h and MM heating at 1173 K for 1 h after normalization with respect to the phosphors synthesized by EF heating, as shown in Fig. 8. The results revealed that the PL intensities of the phosphors synthesized by MM heating were found to be almost identical to those for their counterparts obtained upon EF heating.

The chromaticity ($x$, $y$) of the LNT:$RE^{3+}$ phosphors in the red, green, and blue color regions is shown in Table 1. In general, the PL behavior of the $RE^{3+}$-doped phosphors is not affected by the host material's structure due to the 4f-4f transitions. Consequently, the chromaticity is almost identical for the materials obtained MM and EF heating.

## 4. Conclusions

LNT:$RE^{3+}$ phosphors have been successfully synthesized by millimeter-wave (MM) heating at 1173 K for only 1 h. The resulting materials showed RGB color emission, with LNT:$Eu^{3+}$ and LNT:$Sm^{3+}$ exhibiting red emission, LNT:$Tm^{3+}$ blue emission, and LNT:$Er^{3+}$ green emission. Phosphors with the optimal composition $Li_{1.11}Nb_{0.89}Ti_{0.11}O_3$ doped with 2.5 wt.% $(RE)_2O_3$ were synthesized by MM and FE heating and their PL intensities compared. The highest PL intensity for the material obtained upon MM heating was found to be almost equivalent to that for the specimen obtained upon EF heating. MM irradiation can therefore be considered to be a highly efficient, energy-saving method for the formation of LNT:$RE^{3+}$ phosphors.

## Acknowledgment

We thank Mr. Keita Ozono and Dr. Hiroyuki Hayashi for help of our experiment. This work was partially supported by a research granted from The Murata Science Foundation (2012).

## References

[1] M.E. Villafuerte-Castrejon, J.A. Gracia, E. Cisneros, R. Valenzuela, A.R. West, J. Brit. Ceram. Soc. 83 (1984) 143–145.
[2] M.E. Villafuerte-Castrejon, A. Aragon-Pina, R. Valenzuela, A.R. West, J. Solid State Ceram. 71 (1987) 103–108.
[3] R.I. Smith, A.R. West, Mat. Res. Bull. 27 (1992) 277–285.
[4] H. Hayashi, H. Nakano, K. Suzumura, K. Urabe, A.R. West, Forth Ceram. Soc. 2 (1995) 391–398.
[5] H. Hayashi, K. Urabe, K. Niihara, Key Eng. Mater. 161–163 (1999) 501–504.
[6] L. Farber, I. Levin, A. Borisevichi, I.E. Grey, R.S. Roth, P.K. Davies, J. Solid State Chem. 166 (2002) 81–90.
[7] A.Y. Borisevich, P.K. Davies, J. Am. Ceram. Soc. 85 (2002) 573–578.
[8] Y. Yamamoto, H. Hayashi, T. Sekino, T. Nakayama, T. Kondo, M. Wada, T. Adachi, K. Niihara, Mater. Res. Innovat. 7 (2003) 74–79.
[9] H. Hayashi, H. Nakano, J. Alloys Comp. 502 (2010) 360–364.
[10] H. Hayashi, H. Nakano, M.I. Jones, J. Ceram. Soc. Jpn. 118 (2010) 226–230.

[11] H. Nakano, K. Ozono, H. Hayashi, S. Fujihara, J. Am. Ceram. Soc. 95 (2012) 2795–2797.
[12] Y. Makino, ISI International 47 (2007) 539–544.
[13] Tsaburo Saji, Kinzoku 76 (8) (2006) 65–71. in Japanese.
[14] H. Nakano, T. Saji, M. Yuasa, M. Shoji, M. Mamoru, J. Ceram. Soc. Jpn. 119 (2011) 808–812.
[15] Lorenzo, H. Jaffrezic, B. Roux, G. Boulon, J. Garcia-Sole, Appl. Phys. Lett. 67 (1995) 3735–3737.

*Materials* **2013**, *6*, 2768-2776; doi:10.3390/ma6072768

OPEN ACCESS

*materials*

**ISSN 1996-1944**

www.mdpi.com/journal/materials

*Article*

# Synthesis of New $RE^{3+}$ Doped $Li_{1+x}Ta_{1-x}Ti_xO_3$ (RE: Eu, Sm, Er, Tm, and Dy) Phosphors with Various Emission Colors

**Hiromi Nakano [1,*], Shiho Suehiro [1], Shohei Furuya [1], Hiroyuki Hayashi [2] and Shinobu Fujihara [3]**

[1] Toyohashi University of Technology, Tempaku, Toyohashi 441-8580, Japan; E-Mails: s113517@edu.tut.ac.jp (S.S.); s123440@edu.tut.ac.jp (S.F.)

[2] KRI, Inc., Chudoji Minami-machi, Shimogyo-ku, Kyoto 600-8813, Japan; E-Mail: h-hayasi@kri-inc.jp

[3] Keio University, Yokohama 223-8522, Japan; E-Mail: shinobu@applc.keio.ac.jp

* Author to whom correspondence should be addressed; E-Mail: hiromi@crfc.tut.ac.jp; Tel.: +81-532-44-6606; Fax: +81-532-44-6610.

*Received: 19 April 2013; in revised form: 5 May 2013 / Accepted: 8 June 2013 / Published: 11 July 2013*

**Abstract:** New phosphors with various emission colors for $RE^{3+}$ doped $Li_{1+x}Ta_{1-x}Ti_xO_3$ (LTT) (RE: Eu, Sm, Er, Tm, and Dy) were synthesized by electric furnace at 1423 K for 15 h. The microstructure of the host material and the photoluminescence (PL) property were determined and compared to those of $RE^{3+}$ doped $Li_{1+x}Nb_{1-x}Ti_xO_3$ (LNT). In the LTT phosphor, the highest PL intensity was achieved for the mixture composition $Li_{1.11}Ta_{0.89}Ti_{0.11}O_3$ with a $LiTaO_3$ structure, although it has an M-phase superstructure. In the LTT host material, the effective activators were $Eu^{3+}$ and $Sm^{3+}$ ions, in contrast to the LNT host material. Here, we discuss the relationship between PL property and the host material's structure.

**Keywords:** solid solution; host material; phosphor; structure; photoluminescence

## 1. Introduction

In the ternary $Li_2O$-$M_2O_5$-$TiO_2$ system, $Li_{1+x-y}M_{1-x-3y}Ti_{x+4y}O_3$ (M: Nb or Ta, $0.06 \leq x \leq 0.33$, $0 \leq y \leq 0.17$) forms with a superstructure, and this is known as the M-phase. Since the discovery of the M-phase for $Li_{1+x-y}Nb_{1-x-3y}Ti_{x+4y}O_3$ (LNT) by Castrejon *et al.* [1,2], such structures have been investigated [3–6]. The M-phase superstructure is formed by periodical insertion of an intergrowth

layer in the matrix having a trigonal structure. The relationship between dielectric property and period of the intergrowth layer of the M-phase has been studied [7,8]. To apply this unique structure to the host material of a phosphor, new phosphors have been investigated based on LNT synthesized by a conventional electric furnace [9,10]. A homogeneous material was, however, synthesized at 1373 K for 24 h. We have succeeded in synthesizing an LNT solid solution having a superstructure by millimeter-wave heating for only 1 h above 1173 K [11]. The technique has also been applied to the synthesis of rare-earth doped LNT phosphor [12,13]. The photoluminescence (PL) intensity of LNT:$Eu^{3+}$ at 625 nm was much higher than that of $LiNbO_3$:Eu.[12] Rare-earth-doped $LiTaO_3$ ($RE^{3+}$: $Pr^{3+}$ [14], $Er^{3+}$ [15], $Tb^{3+}$ [16] $Eu^{3+}$ [17] and $Tm^{3+}$ [18]) have also been reported by other groups. Recently, we have reported a new red phosphor based on the quaternary $Li_{1+x}(Ta_{1-z}Nb_z)_{1-x}Ti_xO_3$ (LTNT, $0.05 \le x \le 0.25$, $0 \le z \le 0.625$ ) solid solution as a host material. The PL intensity of the LTNT:$Eu^{3+}$ phosphor was found to be dependent on the concentration of $Eu^{3+}$, $Ti^{4+}$, $Nb^{5+}$, and $Ta^{5+}$ ions [19].

In this work, rare-earth doped $Li_{1+x}Ta_{1-x}Ti_xO_3$ (LTT) phosphors with various emission colors were synthesized by an electric furnace and compared to LNT phosphors for annealing condition, host material's structure, and PL property.

## 2. Results and Discussion

As we reported previously for the $Li_{1+x-y}Nb_{1-x-3y}Ti_{x+4y}O_3$ (LNT, $0 \le x \le 0.25$, $y = 0$) system [12], the PL intensity was clearly improved by the addition of $TiO_2$, which could affect the coordination state of the $Eu^{3+}$ ion and/or induce a structural distortion around this ion. The most important factor is thus expected to be the $TiO_2$ content in the $Li_{1+x}Ta_{1-x}Ti_xO_3$ (LTT) solid solution. The optimal $TiO_2$ concentration was then determined at the maximum emission peak upon excitation at around 399 nm. Red emission of the $Eu^{3+}$-doped LTT was observed at an excitation wavelength of 399 nm due to the intraconfigurational $^7F_0$-$^5L_6$ transition. The maximum emission peak at around 624 nm is associated with the hypersensitive electric-dipole $^5D_0$-$^7F_2$ transition in the $Eu^{3+}$ ion. Figure 1 shows the relationships among the PL intensity, internal quantum efficiency, and the $TiO_2$ content in the ternary Li-Ta-Ti-O system upon varying the $TiO_2$ content from $x = 0$ to 0.25 at a fixed $Eu_2O_3$ concentration of 2.5 wt %. The highest PL intensity is found for the composition of $Li_{1.11}Ta_{0.89}Ti_{0.11}O_3$ ($x = 0.11$, $y = 0$), where the chemical composition is based on the mixture ratio. The internal quantum efficiency revealed a high value of 84.8%, but the highest value appeared in $Li_{1.18}Ta_{0.82}Ti_{0.18}O_3$ with $x = 0.18$. The discrepancy in the $x$ values that give the highest PL intensity and the highest quantum efficiency may come from the different measurement apparatus. Because the integrating sphere was used in the internal quantum efficiency measurement, the "$x = 0.18$" value is supposed to be more appropriate to discuss the relationship between the host crystal composition and the emission properties. The incorporation of $Eu^{3+}$ ions in the crystal structure of LTT would cause the overlapping of orbitals with the adjacent anions, resulting in efficient red-light emission due to the hypersensitive $^5D_0$-$^7F_2$ transition in $Eu^{3+}$.

The LNT phosphor with composition of $Li_{1.11}Nb_{0.89}Ti_{0.11}O_3$: $x = 0.11$ was also found to have the highest PL intensity [9]. Here, the host material's structure was compared between LNT and LTT. In $Li_{1.11}Nb_{0.89}Ti_{0.11}O_3$, the superstructure is formed by periodical insertion of the intergrowth layer with 14.3 nm spacing into a matrix with a trigonal structure (Figure 2b), and satellite reflections appeared around the (012) in the XRD pattern (Figure 2a). The superstructure was formed by doping of the $Ti^{4+}$

ion, and the period was controlled by the Ti content, as described in our previous paper [11]. On the other hand, $Li_{1.11}Ta_{0.89}Ti_{0.11}O_3$ has no superstructure but only a basic structure of $LiTaO_3$ (Figure 2c). The results revealed that the composition area of the M-phase with a superstructure is different between LNT and LTT. In our recent paper [20], the refined structure was compared between $LiTaO_3$ and $Li_{1.11}Ta_{0.89}Ti_{0.11}O_3$ by the Rietveld method from powder X-ray diffraction data. The composition was determined as $Li(Ta_{0.89}Ti_{0.11})O_{2.945}$ from the final structure model, in which the Ti ion is located at the Ta site. By doping of the $Ti^{4+}$ ion into $LiTaO_3$, the <Li-O> distance of the ($LiO_{12}$) polyhedron in the $LiTaO_3$ structure (*R*3*c*) changed from 0.274 nm to 0.270 nm, and the [(Ta,Ti)$O_6$] octahedra are all comparable with each other. As a result, the structure is stable without a superstructure.

**Figure 1.** Relationships among PL intensity, internal quantum efficiency, and $TiO_2$ content in $Li_{1+x}Ta_{1-x}Ti_xO_3$ host material.

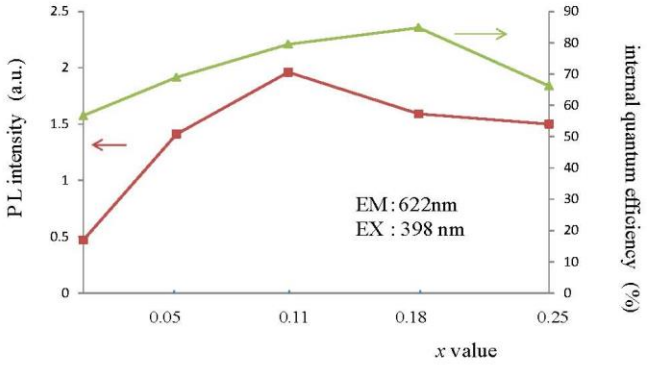


**Figure 2.** Structures of $Li_{1.11}M_{0.89}Ti_{0.11}O_3$ (M: Nb or Ta) host material: (**a**–**b**) LNT; and (**c**) LTT.

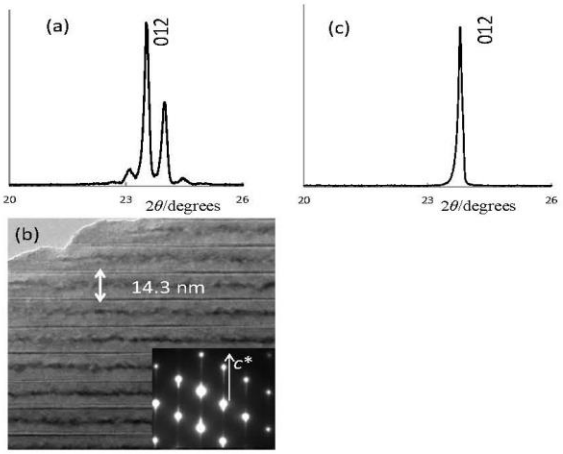

In $Eu^{3+}$-doped LNT phosphor, an annealing time of 24 h is preferable to that of 10 h because the superstructure forms during long-time annealing [10]. In the previous work, PL intensity might have been related to the structural distortion due to the superstructure. Indeed, PL intensity increased with increasing sintering time. In the LTT, the relationship between the annealing time and PL intensity should be clear. Figure 3 shows this relationship in $Li_{1.11}Ta_{0.89}Ti_{0.11}O_3:Eu^{3+}$ phosphor. The results show that the best annealing time is 15 h. For shorter annealing time, a small amount of $EuTaO_4$ was detected around 30 degrees in Figure 4. To diffuse the $Eu^{3+}$ ion into the $LiTaO_3$ structure homogeneously as an activator, the annealing time needs to be 15 h. We confirmed that the $Eu^{3+}$ ion is randomly distributed over the Li site because the electron-density peak at the Li/Eu site of Eu-doped LTT was higher than that at the Li site of LTT [20]. The composition determined by the Rietveld method was $(Li_{0.977}Eu_{0.023})(Ta_{0.89}Ti_{0.11})O_{2.968}$, which has a small amount of oxygen vacancies. The crystal structure of $LiTaO_3$ is flexible with respect to the substitutions of Eu for Li and Ti for Ta, in which the <Li-O> distance of the ($LiO_{12}$) polyhedron is 0.270 nm and 0.272 nm in $Li(Ta_{0.89}Ti_{0.11})O_{2.945}$ and $(Li_{0.977}Eu_{0.023})(Ta_{0.89}Ti_{0.11})O_{2.968}$, respectively.

**Figure 3.** Relationship between PL intensity and annealing time in $Li_{1.11}Ta_{0.89}Ti_{0.11}O_3:Eu^{3+}$ phosphor.

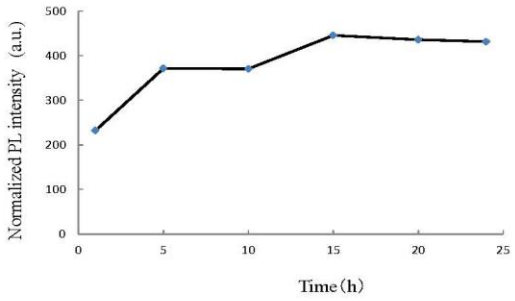


**Figure 4.** XRD patterns of $Li_{1.11}Ta_{0.89}Ti_{0.11}O_3:Eu^{3+}$ phosphors for various annealing times.

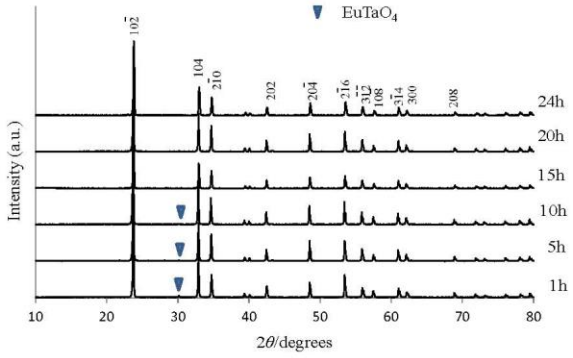

The LTT phosphors with various emission colors were synthesized while doping with trivalent ions of Sm, Er, Tm and Dy. The host material of $Li_{1.11}Ta_{0.89}Ti_{0.11}O_3$ was used at a fixed $RE_2O_3$ concentration of 2.5 wt %. Figure 5 shows the XRD patterns of LTT:$RE^{3+}$ phosphors annealed for 15 h. All structures were $LiTaO_3$-type, and no impurity phase was detected. The results show that the rare-earth ion diffused into the host material homogeneously and that rare-earth ions might also be located at the Li site. Emission peaks were compared between LNT:$RE^{3+}$ and LTT:$RE^{3+}$ phosphor, as shown in Figure 6. It should be mentioned here that the respective f-f excitations were much stronger than any possible charge-transfer excitations for the present LNT:$RE^{3+}$ and LTT:$RE^{3+}$ phosphors. The excitation wavelengths were then chosen with the strongest f-f excitations observed in each phosphor. Red emission of the $Eu^{3+}$-doped LTT was obviously brighter than that of LNT phosphor. Red emission was also observed for the $Sm^{3+}$-doped LNT upon excitation at around 411 nm due to the $^6H_{5/2}$-$^6P_{3/2}$ transition. Upon excitation at 411 nm, the photoluminescence spectra showed emission peaks at 568 nm ($^4G_{5/2}$-$^6H_{5/2}$), 607 nm ($^4G_{5/2}$-$^6H_{7/2}$), and 651 nm ($^4G_{5/2}$-$^6H_{9/2}$). The splitting of the 607 nm emission is prominent in LNT phosphor. Therefore it seems that the peak intensity ratio of LTT phosphor at 607/651 nm is larger than that of LNT phosphor. This would be caused by the difference in the overlapping of orbitals with the adjacent anions (Ta/Nb). A green emission peak at 527 nm ($^4S_{3/2}$-$^4I_{15/2}$) was observed for LNT:$Er^{3+}$ upon excitation at 552 nm ($^4I_{15/2}$-$^2H_{11/2}$). Blue emission was observed at 360 nm ($^1D_2$-$^3F_4$ transition) for the LNT:$Tm^{3+}$ phosphor upon excitation at 463 nm ($^3H_6$-$^1D_2$). Yellow emission peaks at 584 nm ($^4F_{9/2}$-$^6H_{13/2}$) were observed for LNT:$Dy^{3+}$ upon excitation at 355 nm ($^6H_{15/2}$ -$^4M_{15/2}$). The highest emission peak intensity was compared between LNT:$RE^{3+}$ and LTT:$RE^{3+}$. Green and Blue emissions of LNT phosphor were brighter than those of LTT phosphor. The internal quantum efficiency of these phosphors were low level; 23% for LTT:$Sm^{3+}$, 22% for LTT:$Er^{3+}$, 35% for LTT:$Tm^{3+}$, and 28% for LTT:$Dy^{3+}$.

**Figure 5.** XRD patterns of $Li_{1.11}Ta_{0.89}Ti_{0.11}O_3$:$RE^{3+}$ (RE: Dy. Tm, Er, Sm, Eu) for 15 h annealing.

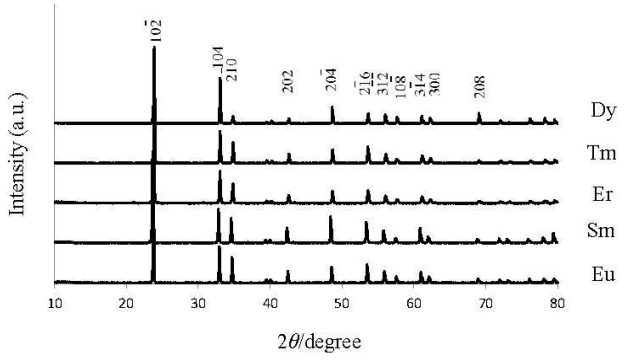

**Figure 6.** Comparison of PL intensity between LNT:$RE^{3+}$ and LTT:$RE^{3+}$. Dotted line: LNT:$RE^{3+}$, solid line: LTT:$RE^{3+}$.

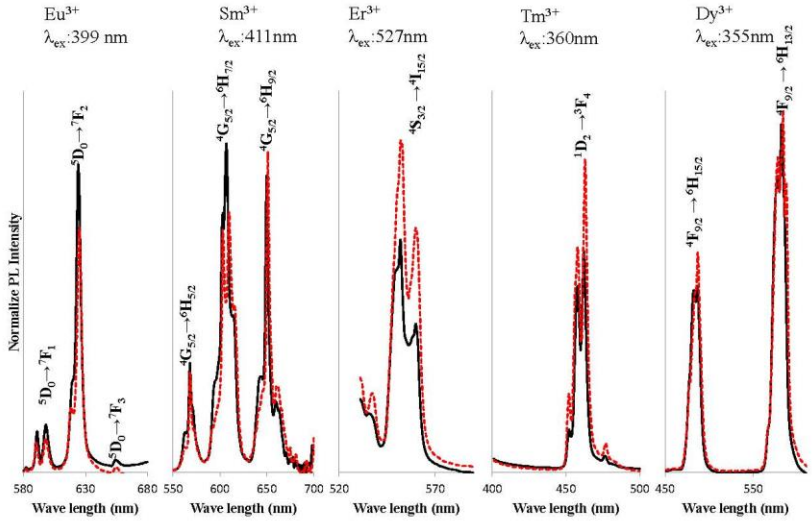


In contrast, the most effective activator was the $Eu^{3+}$ ion in the LTT host material. The red emission intensity excited at 339 nm of LTT: $Eu^{3+}$ phosphor is three times higher than that of $Y_2O_2S$: $Eu^{3+}$ (4.3 at %), which is well known as a red phosphor. It is assumed that small differences in the lattice site between LNT and LTT host materials would affect the transition probability of the respective $RE^{3+}$ ions. The combination of the host material and the emitting $RE^{3+}$ ion is of great significance in designing new phosphors. A more detailed structural analysis, and the relevant theoretical calculations, will be performed in the near future.

Table 1 shows the chromaticity (*x*, *y*) of the LNT:$RE^{3+}$ and LTT:$RE^{3+}$ phosphors in the red, green, blue and yellow color regions. In general, the PL behavior of the $RE^{3+}$-doped phosphors is not affected by the host material's structure due to the 4f-4f transitions. In Sm phosphor, however, the difference in the emission intensity ratio at 606/650 nm affected the chromaticity.

**Table 1.** Chromaticity (*x*, *y*) of LNT and LTT phosphors.

| Activator | LTT:$RE^{3+}$ | | LNT:$RE^{3+}$ | |
|---|---|---|---|---|
| | *X* | *Y* | *X* | *Y* |
| Eu | 0.673 | 0.327 | 0.676 | 0.324 |
| Sm | 0.622 | 0.378 | 0.630 | 0.370 |
| Er | 0.307 | 0.685 | 0.347 | 0.647 |
| Tm | 0.144 | 0.033 | 0.143 | 0.033 |
| Dy | 0.418 | 0.425 | 0.433 | 0.423 |

## 3. Experimental Procedure

The starting materials used were $Li_2CO_3$, $Ta_2O_5$ and $TiO_2$ (>99.9% grade) to prepare the solid solution of LTT. The compositions of the LTT solid solutions prepared in this work followed the formula $Li_{1+x-y}Ta_{1-x-3y}Ti_{x+4y}O_3$ with $0.05 < x < 0.25$, $y = 0$ as a host material. Rare earths ($Eu_2O_3$, $Sm_2O_3$, $Er_2O_3$, $Tm_2O_3$ and $Dy_2O_3$ > 99.9% grade) were doped in the host material. These powders were mixed and pressed in air at 1423 K for 1 h to 24h in a conventional electric furnace. As comparison materials, the rare earth doped $Li_{1+x}Nb_{1-x}Ti_xO_3$ (LNT) phosphors were also sintered at 1373 K for 24 h [13].

Structural analysis was carried out by X-ray diffraction (XRD) using a RINT 2500 (Rigaku Co., Ltd., Tokyo, Japan) operating at 40 kV and 200 mA. Microstructure images were observed by a scanning electron microscope (SEM) (SU8000, Hitachi Co., Ltd., Tokyo, Japan) operating at 3 kV. High-resolution TEM (HRTEM) images were observed by a device (2100 F, JEOL Co., Ltd., Tokyo, Japan) operating at 200 kV and equipped with energy-dispersed spectroscopy (EDS).

Excitation and emission spectra of the obtained samples were measured by a spectrometer (model FP-6500, JASCO international Co., Ltd., Tokyo, Japan). Quantum efficiency was measured by a spectral radiometer (MCPD-7000, Otsuka Electronics Co., Ltd., Osaka, Japan).

## 4. Conclusions

New phosphors have been successfully synthesized by doping rare-earth materials into a $Li_{1+x}Ta_{1-x}Ti_xO_3$ solid solution as a host material. The host material's structure and photoluminescence (PL) property was compared to the $RE^{3+}$-doped $Li_{1+x}Nb_{1-x}Ti_xO_3$ (LNT). The resulting materials showed various color emissions, with LNT:$Eu^{3+}$ and LNT:$Sm^{3+}$ exhibiting red emission, LNT:$Tm^{3+}$ blue emission, LNT:$Er^{3+}$ green emission, and LTT:$Dy^{3+}$ yellow emission. The host material's structure of LTT phosphor with the optimal composition $Li_{1.11}Nb_{0.89}Ti_{0.11}O_3$ was not a superstructure. Therefore, the distortion due to superstructure did not affect the PL intensity in the LTT phosphor. The annealing time to synthesize the homogeneous phosphor was reduced from 24 h to 15 h. By doping $Ti^{4+}$ and $Eu^{3+}$ ions into the $LiTaO_3$, the <Li-O> distance of the $[LiO_{12}]$ polyhedron in the $LiTaO_3$ structure (*R*3*c*) changed without a superstructure. This change affected the interaction with the adjacent anions, and the emission from the $Eu^{3+}$ ion in the Li site achieved a high value of internal quantum efficiency. In the LTT host material, the most effective activator was the $Eu^{3+}$ ion. On the other hand, the emission intensities of Er- and Tm-doped LTT phosphors were lower that of LNT phosphor. We conclude that small differences in the lattice site between LNT and LTT host materials would affect the emission energy of the $RE^{3+}$ ions.

## Acknowledgments

We thank S. Yamada of Denki Kagaku Kogyo Co., Ltd. for help wtih our experiment. This work was partially supported by a research granted from The Murata Science Foundation (2012).

**References**


1. Villafuerte-Castrejon, M.E.; Gracia, J.A.; Cisneros, E.; Valenzuela, R.; West, A.R. New rutile solid solutions $Ti_{1-4x}Li_xM_{3x}O_2$:M = Nb, Ta, Sb. *J. Brit. Ceram. Soc.* **1984**, *83*, 143–145.
2. Villafuerte-Castrejon, M.E.; Aragon-Pina, A.; Valenzuela, R.; West, A.R. Compound and solid-solution formation in the system $Li_2O$-$Nb_2O_5$-$TiO_2$. *J. Solid State Ceram.* **1987**, *71*, 103–108.
3. Smith, R.I.; West, A.R. Characterization of an incommensurate LiTiNb oxide. *Mater. Res. Bull.* **1992**, *27*, 277–285.
4. Hayashi, H.; Nakano, H.; Suzumura, K.; Urabe, K.; West, A.R. Superstructure in LiTiNb oxides. *Forth Ceram. Soc.* **1995**, *2*, 391–398.
5. Hayashi, H.; Urabe, K.; Niihara, K. Preparation of stoichiometric crystalline $Li(Nb,Ti)O_3$ solid solutions by sol-gel processing with metal alkoxides. *Key Eng. Mater.* **1999**, *501*, 161–163.
6. Farber, L.; Levin, I.; Borisevichi, A.; Grey, I.E.; Roth, R.S.; Davies, P.K. Structural study of $Li_{1+x-y}Nb_{1-x-3y}Ti_{x+4y}O_3$ solid solutions. *J. Solid State Chem.* **2002**, *166*, 81–90.
7. Borisevich, A.Y.; Davies, P.K. Crystalline structure and dielectric properties of $Li_{1+x-y}Nb_{1-x-3y}Ti_{x+4y}O_3$ M-phase solid solutions. *J. Am. Ceram. Soc.* **2002**, *85*, 573–578.
8. Yamamoto, Y.; Hayashi, H.; Sekino, T.; Nakayama, T.; Kondo, T.; Wada, M.; Adachi, T.; Niihara, K. Microstructure and dielectric properties of sintered Li-Nb-Ti-O solid solution ceramics having superstructure. *Mater. Res. Innov.* **2003**, *7*, 74–79.
9. Hayashi, H.; Nakano, H. Evolution and preparation of $Li_{1+x-y}Nb_{1-x-3y}Ti_{x+4y}O_3$ solid solution with superstructure as new phosphor. *J. Alloy. Compd.* **2010**, *502*, 360–364.
10. Hayashi, H.; Nakano, H.; Jones, M.I. Microstructure and luminescence of Eu-doped $Li_{1+x-y}Nb_{1-x-3y}Ti_{x+4y}O_3$ solid solutions with superstructure. *J. Ceram. Soc. Jpn.* **2010**, *118*, 226–230.
11. Nakano, H.; Saji, T.; Yuasa, M.; Shoji, M.; Mamoru, M. Rapid synthesis and structural analysis of Li-Nb-Ti-O solid solutions with superstructure by millimeter-wave heating. *J. Ceram. Soc. Jpn.* **2011**, *119*, 808–812.
12. Naknao, H.; Ozono, K.; Saji, T.; Miyake, S.; Hiroyuki, H. Rapid synthesis of $Eu^{3+}$-doped LNT (Li-Nb-Ti-O) phosphor by millimeter-wave heating. *Opt. Mater.* **2012**, in press.
13. Nakano, H.; Suehrio, S.; Saji, T.; Miyake, S. Synthesis of a rare-erath doped LNT (Li-Nb-Ti-O) phosphor by millimemetr-wave heating. *J. Alloy. Compd.* **2013**, 475–479.
14. Gryk, D.; Dyl, D.; Ryba-Romanowski, W.; Grinberg, M.; Spectral properties of $LiTaO_3$:$Pr^{3+}$ under high hydrostatic pressure. *J. Phys. Condens. Matter* **2005**, *17*, 5383–5395.
15. Kostritskii, S.M.; Maring, D.B.; Tavlykasev, R.F.; Ramaswamy, R.V. Energy transfer upconversion in Er-doped $LiTaO_3$. *Appl. Phys. Lett.* **2000**, *76*, 2161–2163.
16. Ryba-Romanowski, W.; Golab, S.; Dominiak-Dzik, G.; Paltnikov, M.N.; Sidorov, N.V. Influence of temperature on luminescence of terbium ions in $LiNbO_3$. *J. Appl. Lett.* **2001**, *78*, 3610–3611.
17. Gasparotto, G.; Cebin, M.A.; Goes, M.S.; Lima, S.A.M.; Davolos, M.R.; Varela, J.A.; Paiva-Santos, C.O.; Zaghete, M.A. Correlation between the spectroscopic and structural properties with the occupation of $Eu^{3+}$ sites in powdered $Eu^{3+}$-doped $LiTaO_3$ prepared by the pechini method. *J. Appl. Phys.* **2009**, *106*, 3506–3509.

18. Sokolska, I.; Ryba-Romanowski, W.; Golab, S.; Baba, M.; Swirkowicz, M.; Lukasiewicz, T. Spectroscopy of $LiTaO_3$:$Tm^{3+}$ crystals. *J. Phys. Chem. Solids* **2000**, *61*, 1573–1581.
19. Nakano, H.; Ozono, K.; Hayashi, H.; Fujihara, S. Synthesis and luminescent properties of a new $Eu^{3+}$-doped $Li_{1+x}(Ta_{1-z}Nb_z)_{1-x}Ti_xO_3$ red phosphor. *J. Am. Ceram. Soc.* **2012**, 2795–2797.
20. Uchida, T.; Suehiro, S.; Asaka, T.; Nakano, H.; Fukuda, K. Syntheses and crystal structures of $Li(Ta_{0.89}Ti_{0.11})O_{2.945}$ and $(Li_{0.977}Eu_{0.023})(Ta_{0.89}Ti_{0.11})O_{2.968}$. *Powder Diffr.* **2013**, in press.

Optical Materials 35 (2013) 2045–2048

Contents lists available at SciVerse ScienceDirect

Optical Materials

journal homepage: www.elsevier.com/locate/optmat

# Rapid synthesis of $Eu^{3+}$-doped LNT (Li–Nb–Ti–O) phosphor by millimeter-wave heating

Hiromi Nakano [a,*], Keita Ozono [a], Tasaburo Saji [b], Syoji Miyake [b], Hiroyuki Hayashi [c]

[a] Toyohashi University of Technology, Tempaku, Toyohashi 441-8580, Japan
[b] MSP Corp., Takaida, Higashiosaka 577-0053, Japan
[c] KRI, Inc., Chudoji Minami-machi, Shimogyo-ku, Kyoto 600-8813, Japan

ARTICLE INFO

*Article history:*
Available online 3 November 2012

*Keywords:*
Millimeter-wave heating
Superstructure
oxide
Photoluminescence

ABSTRACT

We have been investigated a new phosphor containing the LNT ($Li_{1+x-y}Nb_{1-x-3y}Ti_{x+4y}O_3$ ($0.11 \leqslant x \leqslant 0.33$, $0 \leqslant y \leqslant 0.09$) with the superstructure as a host material. An $Eu^{3+}$-doped LNT has prepared by sintering at 1373 K for 24 h by a conventional electric furnace before. A fast synthesizing technique that uses lower energy is required for application of the materials. In the present study, the $Eu^{3+}$-doped LNT phosphor has been successfully synthesized by millimeter-wave (MM) heating at 1173 K for 1 h. A bright red emission was observed at an excitation wavelength of 398 nm. The maximum emission peak observed at around 625 nm is associated with the intra-4f shell $^5D_0$–$^7F_2$ transition in $Eu^{3+}$ ions. The photoluminescence (PL) intensity of the specimen by MM heating was nearly equivalent to that of the specimen obtained by electric furnace heating. MM radiation can therefore be considered to be a highly efficient, energy-saving method for the formation of $Eu^{3+}$-doped LNT phosphors.



## 1. Introduction

In the $Li_2O$–$Nb_2O_5$–$TiO_2$ system, $Li_{1+x-y}Nb_{1-x-3y}Ti_{x+4y}O_3$ ($0.11 \leqslant x \leqslant 0.33$, $0 \leqslant y \leqslant 0.09$) (LNT) forms with a superstructure, and this is known as the M-phase. Since the discovery of the M-phase by Villafuerte-Castrejon et al. [1,2], such structures have been investigated [3–6]. The superstructure of the M-phase is formed by periodical insertion of the intergrowth layer in the matrix having a trigonal structure. The relationship between dielectric property and period of the intergrowth layer of the M-phase has been studied [7,8]. Hayashi and Nakano have developed a new red phosphor containing LNT as host material that has an emission peak of around 625 nm upon excitation at 398 nm in $Eu^{3+}$-doped LNT [9,10]. Many studies of rare-earth doped $LiNbO_3$ have concentrated on the optical properties of $LiNbO_3$ crystal as an excellent laser host matrix [11]. Indeed, as the LNT host material is a polycrystalline ceramic, it can be synthesized in a conventional electric furnace. The photoluminescence (PL) intensity of LNT:Eu at 625 nm was much higher than that of $LiNbO_3$:Eu [9].

A homogeneous material was, however, synthesized at 1373 K for 24 h after calcination at 1273 K for 3 h. A fast synthesizing technique that uses lower energy is required for application of this material. Heating by millimeter-wave (MM) radiation has certain advantages in industrial processes or applications from the viewpoints of the homogeneity of large materials, control of grain growth, and densification at low temperature [12].

Recently, we have succeeded in synthesizing LNT solid solution having a superstructure by millimeter-wave heating for only 1 h above 1173 K [13].

In this time, the $Eu^{3+}$-doped LNT phosphor was synthesized by MM radiation at 1173 K for 1 h. The PL intensity was almost equivalent to that of the specimen obtained upon electric furnace heating. Furthermore, the structure and grain morphologies of these phosphors were analyzed and the results of that study will be described below in more detail.

## 2. Experimental procedure

The starting materials used were $Li_2CO_3$, $Nb_2O_5$ and $TiO_2$ (> 99.9% grade) to prepare the solid solution of LNT. The compositions of the LNT solid solutions prepared in this work followed the general formula $Li_{1+x-y}Nb_{1-x-3y}Ti_{x+4y}O_3$ with $0.05 \leqslant x \leqslant 0.25$, $y = 0$. The $TiO_2$ content of the specimens was varied from 5 to 20 mol%. The powders were mixed and pressed in air at 1173 K for 1 h by millimeter-wave heating. The millimeter-wave heating equipment consists of a 24 GHz gyrotron millimeter-wave generator and a multi-mode chamber (MSP Corp., Japan). The specimens were surrounded by a heat insulator, and their temperature was measured with a thermocouple placed near the specimens. The total number of specimens in the MM chamber was the same each time because the electric power was controlled. The electric power is an

* Corresponding author.
*E-mail address:* hiromi@crfc.tut.ac.jp (H. Nakano).

0925-3467/$ - see front matter © 2012 Elsevier B.V. All rights reserved.
http://dx.doi.org/10.1016/j.optmat.2012.09.021

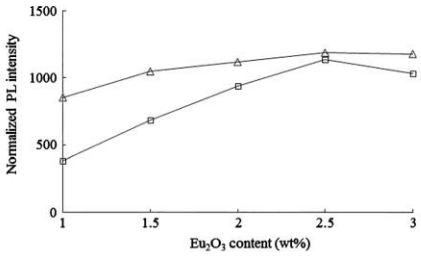


**Fig. 1.** Relationship between $Eu_2O_3$ content and PL intensity. Triangle: EF heating, square: MM heating.

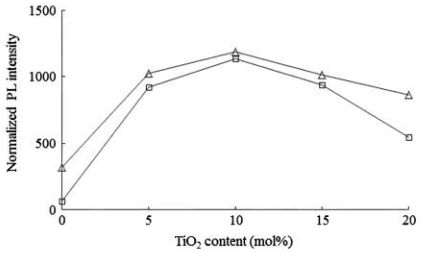


**Fig. 2.** Relationship between $TiO_2$ content and PL intensity. Triangle: EF heating, square: MM heating.

important factor in the MM heating technique, and the optimal electric power was found to be 2 kW for synthesis of the present phosphor materials. The heating rate was approximately 30 K/min, and the specimen was cooled down in the chamber after sintering. As a result, we could successfully apply this technique to the synthesis of the materials. As comparison materials, the mixed powders were also sintered at 1273 K for 3 h and 1373 K for 24 h in a conventional electric furnace (EF).

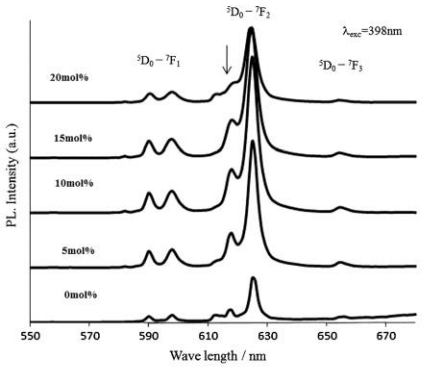


**Fig. 3.** Emission spectra excited by 398 nm of $Eu^{3+}$-doped LNT with various $TiO_2$ content for the samples produced using the MM method.

Structural analysis was carried out by X-ray diffraction (XRD) using a RINT 2500 (Rigaku Co., Ltd., Japan) operating at 40 kV and 200 mA. Microstructure images were observed by a scanning electron microscope (SEM) (SU8000, Hitachi Co., Ltd., Japan) operating at 3 kV. High-resolution TEM (HRTEM) images were observed by a device (2100 F, JEOL Co., Ltd., Japan) operating at 200 kV and equipped with energy-dispersed spectroscopy (EDS).

Excitation and emission spectra of the sintered samples were measured by a spectrometer (model FP-6500, JASCO).

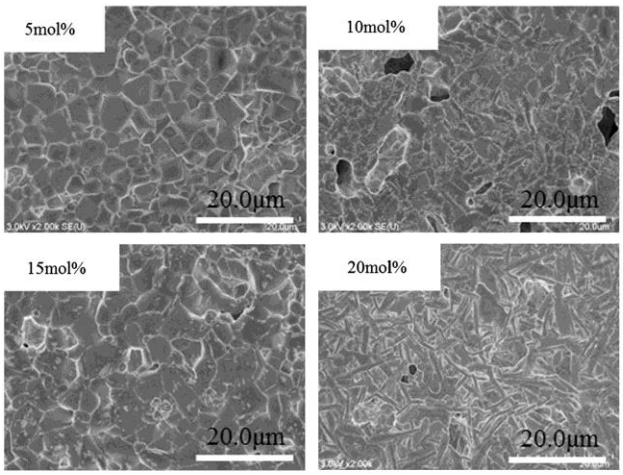


**Fig. 4.** Grain morphologies of $Eu^{3+}$-doped LNT with various $TiO_2$ content for the samples produced using the MM method.

### 3. Results and discussions

Red emission of the $Eu^{3+}$-doped LNT was observed at an excitation wavelength of 398 nm [9]. The maximum emission peak observed at around 625 nm is associated with the intra-4f shell $^5D_0$–$^7F_2$ transition in $Eu^{3+}$ ions. In order to improve the PL intensity of the phosphor produced using MM radiation, the optimal concentration of $TiO_2$ or $Eu_2O_3$ was determined by measuring the effect of additives on the PL intensity at the maximum emission peak. Thus, the $Eu_2O_3$ content was varied from 1.0 to 3.0 wt.% in LNT ($x = 0.11$, $y = 0$). Fig. 1 shows the relationship between $Eu_2O_3$ content and PL intensity after MM heating and EF heating, respectively. The PL intensity was normalized with respect to a reference value. In the case of MM heating, the selective-heating effect of additives such as rare-earth ions has been reported previously, and it should be controlled constantly when synthesizing rare-earth phosphors [12]. The optimal concentration of $Eu_2O_3$ was found to be 2.5 wt.%, with the trend of this effect being the same for both samples. The $TiO_2$ content was subsequently varied from 0 to 20 mol%, $Li_{1+x-y}Nb_{1-x-3y}Ti_{x+4y}O_3$ ($0 \leqslant x \leqslant 0.25$, $y = 0$), at a fixed $Eu_2O_3$ concentration of 2.5 wt.%. Fig. 2 shows the relationship between $TiO_2$ content and PL intensity. The LNT phosphor doped with 10 mol% $TiO_2$ ($x = 0.11$, $y = 0$) was found to have the highest PL intensity. Indeed, increasing the value of $y$ in LNT resulted in a decrease in the PL intensity, as we reported previously [9]. This result shows that the PL intensity is clearly improved by addition of $TiO_2$. We next studied whether $TiO_2$ influences the coordination of the $Eu^{3+}$ ion and/or induces a structural distortion around this ion (Fig. 3).

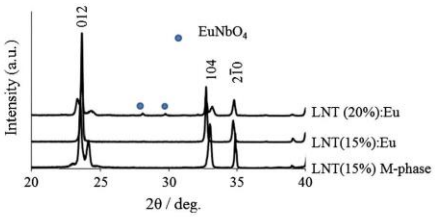


**Fig. 5.** XRD patterns of LNT and $Eu^{3+}$-doped LNT for the samples produced using the MM method.

The emission peak intensity ratio at around 617 nm (indicated by arrow) decreased with increasing $TiO_2$ content due to a change in the crystal structure around the $Eu^{3+}$ ion induced by the $Ti^{4+}$ ion [9]. This change in the crystal structure was also investigated by SEM (Fig. 4). Consequently, although the grain morphology of the LNTs containing 5–15 mol% $TiO_2$ was spherical in shape, it became plate-like in the LNT containing 20 mol% $TiO_2$. Above 10 mol% $TiO_2$ in the LNT solid solution, and in the absence of the $Eu^{3+}$ ion, the superstructure was formed by periodical insertion of the intergrowth layer into the trigonal [13]. The phase containing the superstructure is called the M-phase and the morphology of its grains is plate-like. However, as can be seen from the XRD patterns, the $Eu^{3+}$-doped LNT did not form such a superstructure, even when

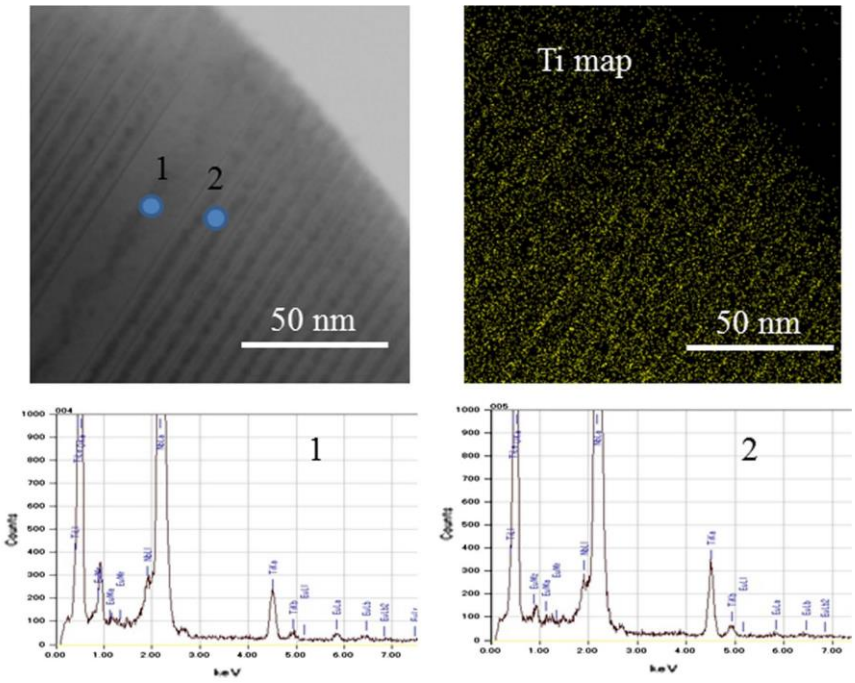


**Fig. 6.** STEM image, Ti mapping and point analysis of $Eu^{3+}$-doped LNT with $TiO_2$ 20 mol% for the samples produced using the MM method.

doped with 15 mol% $TiO_2$. Fig. 5 shows the XRD patterns of LNT doped with 15 mol% $TiO_2$ (M-phase) and the $Eu^{3+}$-doped LNTs containing 15 and 20 mol% $TiO_2$. The satellite peak caused by the periodical structure in the LNT solid solution can be seen in the region of the (012) peak in the M-phase [13]. In contrast, the $Eu^{3+}$-doped LNT containing 15 mol% $TiO_2$ shows no such superstructure. A small satellite peak was detected close to the (012) at concentrations above 20 mol% $TiO_2$. Likewise, the two peaks that appear at around 34° are due to the $LiNbO_3$ matrix structure and the M-phase, respectively. This result confirms that the periodic structure is disturbed by dispersion of $Eu^{3+}$ ion into the LNT matrix. The $Eu^{3+}$ ion may occupy the octahedral $Li^+$ site in the host structure [14], thus preventing periodic intergrowth layer in the LNT matrix. A small amount of $EuNbO_4$ was formed in the LNT doped with 20 mol% $TiO_2$. Microstructural analysis of the $Eu^{3+}$-doped LNT was performed using a TEM equipped with EDS. Fig. 6 shows the STEM image, Ti mapping image and EDS spectra in $Eu^{3+}$-doped LNT doped with 20 mol% $TiO_2$. These images show that the intergrowth layer is inserted non-homogeneously into the LNT matrix. Furthermore, the Ti mapping image shows that the Ti content of the intergrowth layer is higher than that of the LNT matrix and that the intergrowth layer has a rock-salt type $Li_2TiO_3$ structure. The peak intensities were measured and the atomic ratios of Ti/Nb and Eu/Nb were calculated at many points. At typical measurement points, the ratios showed differences of Ti/Nb: 0.047 and Eu/Nb: 0.226 at No. 1 and Ti/Nb: 0.076 and Eu/Nb: 0.205 at No. 2 in Fig. 6. The Eu content of the intergrowth layer was lower than that of the LNT matrix, and above 20 mol% $TiO_2$, the excess $Eu^{3+}$ ion remains as $EuNbO_4$. The Eu content of the intergrowth layer was lower than that of the LNT matrix, and above 20 mol% $TiO_2$, the excess $Eu^{3+}$ ion remains as $EuNbO_4$. In the case of EF heating, the LNT:Eu sintered for 24 h was higher than that of the LNT:Eu sintered for 10 h thus suggesting that the $Eu^{3+}$ ion disperses slowly into the LNT matrix over 24 h [10]. In contrast, the $Eu^{3+}$ ion disperses rapidly into the LNT matrix in only 1 h under MM heating, thus meaning that the PL intensity of the LNT phosphor is almost the same as that of the LNT obtained by EF heating.

## 4. Conclusions

In summary, an $Eu^{3+}$-doped LNT phosphor has been successfully synthesized by millimeter-wave (MM) heating at 1173 K for 1 h. MM radiation can thus be considered a highly efficient, energy-saving method for the formation of $Eu^{3+}$-doped LNT phosphors.

(1) The optimal $Eu_2O_3$ content as an additive was shown to be 2.5 wt.% in the LNT host material.
(2) Upon $Eu_2O_3$ addition, formation of the superstructure and periodical insertion of the intergrowth layer are disturbed in the LNT host matrix.
(3) The $TiO_2$ content in the LNT material also affects the structure of the host matrix, with a $TiO_2$ content of 10 mol% in the LNT producing the highest PL intensity.

## Acknowledgements

This work was partially supported by a Grant-in-Aid for Scientific Research (c) No. 21560704 (H.N.) by the Japan Society for the Promotion of Science and by the Takahashi Industrial and Economic Research Foundation.

## References

[1] M.E. Villafuerte-Castrejon, J.A. Gracia, E. Cisneros, R. Valenzuela, A.R. West, J. Br. Ceram. Soc. 83 (1984) 143–145.
[2] M.E. Villafuerte-Castrejon, A. Aragon-Pina, R. Valenzuela, A.R. West, J. Solid State Ceram. 71 (1987) 103–108.
[3] R.I. Smith, A.R. West, Mat. Res. Bull. 27 (1992) 277–285.
[4] H. Hayashi, H. Nakano, K. Suzumura, K. Urabe, A.R. West, Forth Ceram. Soc. 2 (1995) 391–398.
[5] H. Hayashi, K. Urabe, K. Niihara, Key Eng. Mater. 161–163 (1999) 501–504.
[6] L. Farber, I. Levin, A. Borisevichi, I.E. Grey, R.S. Roth, P.K. Davies, J. Solid State Chem. 166 (2002) 81–90.
[7] A.Y. Borisevich, P.K. Davies, J. Am. Ceram. Soc. 85 (2002) 573–578.
[8] Y. Yamamoto, H. Hayashi, T. Sekino, T. Nakayama, T. Kondo, M. Wada, T. Adachi, K. Niihara, Mater. Res. Innovations 7 (2003) 74–79.
[9] H. Hayashi, H. Nakano, J. Alloys Compd. 502 (2010) 360–364.
[10] H. Hayashi, H. Nakano, M. I Jones, J. Ceram. Soc. Jpn. 118 (2010) 226–230.
[11] D. Hreniak, W. Strek, A. Speghini, M. Bettinelli, G. Boulon, Y. Guyot, Appl. Phys. Lett. 88 (2006) 161118-1–161118-3.
[12] Y. Makino, ISI International 47 (2007) 539–544.
[13] H. Nakano, T. Saji, M. Yuasa, M. Shoji, M. Mamoru, J. Ceram. Soc. Jpn. 119 (2011) 808–812.
[14] H. Lorenzo, B. Jaffrezic, G.Boulon. Roux, J. Garcia-Sole, Appl. Phys. Lett. 67 (1995) 3735–3737.

## TECHNICAL ARTICLE

# Syntheses and crystal structures of $Li(Ta_{0.89}Ti_{0.11})O_{2.945}$ and $(Li_{0.977}Eu_{0.023})(Ta_{0.89}Ti_{0.11})O_{2.968}$

Tomohiro Uchida,[1] Shiho Suehiro,[2] Toru Asaka,[1] Hiromi Nakano,[2] and Koichiro Fukuda[1,a)]
[1]*Department of Environmental and Materials Engineering, Nagoya Institute of Technology, Nagoya 466-8555, Japan*
[2]*Department of Environmental and Life Sciences, Toyohashi University of Technology, Toyohashi 441-8580, Japan*

(Received 16 October 2012; accepted 30 December 2012)

Crystal structures of $Li(Ta_{0.89}Ti_{0.11})O_{2.945}$ and $(Li_{0.977}Eu_{0.023})(Ta_{0.89}Ti_{0.11})O_{2.968}$ were investigated by laboratory X-ray powder diffraction. Both title compounds were trigonal with space group *R*3*c* and $Z = 6$. The hexagonal unit-cell dimensions were $a = 0.514\ 82\ 9(2)$ nm, $c = 1.377\ 61\ 2(4)$ nm, and $V = 0.316\ 21\ 6(2)$ nm$^3$ for the former compound and $a = 0.517\ 71\ 2(2)$ nm, $c = 1.373\ 50\ 0(6)$ nm, and $V = 0.318\ 81\ 2(3)$ nm$^3$ for the latter. The initial structural models, being isostructural with $LiTaO_3$, were refined by the Rietveld method. The maximum-entropy method-based pattern fitting (MPF) method was subsequently used to confirm the validity of the structural models, in which conventional structure bias caused by assuming intensity partitioning was minimized. Atomic arrangements of the final structural models were in excellent agreement with the three-dimensional electron-density distributions determined by MPF. © *2013 International Centre for Diffraction Data*.
[doi:10.1017/S0885715613000018]

Key words: lithium tantalate, x-ray powder diffraction, Rietveld method, phosphor

### I. INTRODUCTION

The crystal structure of $LiTaO_3$ (space group *R*3*c*) is isomorphous with that of $LiNbO_3$, which is closely related to those of corundum and ilmenite (Megaw, 1973). The room-temperature structure of $LiTaO_3$ has been determined by single-crystal X-ray diffraction and neutron diffraction methods (Abrahams and Bernstein, 1967; Abrahams *et al.*, 1967; Ohgaki *et al.*, 1989; Hsu *et al.*, 1997). The Li and Ta atoms are on the triad axis with Wyckoff position 6*a* (Figure 1). The Li atom has 12 O-atom neighbors with the three of the longest (=0.345 nm) 12 Li–O bonds, and the $TaO_6$ polyhedron shows two types of bond lengths of 0.191 and 0.207 nm. The Li atom is displaced along the *c*-axis with respect to the double oxygen layers by ca. 0.060 nm, and the Ta atom is ca. 0.020 nm from the midpoint between the oxygen layers (Hsu *et al.*, 1997).

A combined use of the Rietveld method (Rietveld, 1967), the maximum-entropy method (MEM) (Takata *et al.*, 2001), and the MEM-based pattern fitting (MPF) method (Izumi, 2004) has enabled us to determine three-dimensional electron-density distributions (EDD), which efficiently disclose new structural details. The Rietveld method and MEM have a drawback in determining the EDD from X-ray powder diffraction (XRPD) data because the observed structure factors, $F_o$(Rietveld), are biased toward the structural model assuming intensity partitioning. On the other hand, the MPF method can minimize the structural bias. Thus, the MEM and MPF analyses are alternately repeated (REMEDY cycle) until the reliability indices reach the minima (Izumi *et al.*, 2001). Crystal structures are represented not by structural parameters but by 3D EDD in MPF.

Recently, $LiTaO_3$ crystal, when it is codoped with $Eu^{3+}$ and $Ti^{4+}$, has been found to demonstrate excellent performance as the red phosphor under direct excitation of the 4*f* electron at 541 nm (Nakano *et al.*, 2012). In order to clarify the highly efficient photoluminescence mechanism and further improve the performance, detailed structural information is necessary for this material. In the present study, we prepared two types of powder specimens, $Ti^{4+}$-doped $LiTaO_3$ and $Eu^{3+}$- and $Ti^{4+}$-codoped $LiTaO_3$, to investigate the crystal structures from XRPD data. The *z* coordinates of Li/Eu sites have been differed prominently among the three isomorphous structures.

### II. EXPERIMENTAL

#### A. Syntheses

Two types of powder specimens with starting compositions of $Li(Ta_{0.89}Ti_{0.11})O_{2.945}$ (sample LTTO) and $(Li_{0.977}Eu_{0.023})(Ta_{0.89}Ti_{0.11})O_{2.968}$ (LETTO) were prepared from the reagent-grade chemicals $Li_2CO_3$, $Eu_2O_3$, $Ta_2O_5$, and $TiO_2$. Each of the well-mixed chemicals was pressed into pellets, heated at 1273 K for 3 h and continuously at 1423 K for 24 h, and followed by cooling to ambient temperature by cutting furnace power. The densely sintered pellets were finely ground to obtain powder specimens.

#### B. Characterization

A diffractometer (X'Pert PRO Alpha-1, PANalytical B.V., Almelo, the Netherlands), equipped with an incident-beam Ge (111) Johansson monochromator to obtain Cu$K\alpha_1$ radiation and a high-speed detector, was used in the Bragg–Brentano geometry. The X-ray generator was operated at 45 kV and 40 mA. An automatic divergence slit was used to keep a constant illuminated length of 5 mm on the specimen surface. Other experimental conditions were: continuous scan,

a)Author to whom correspondence should be addressed. Electronic mail: fukuda.koichiro@nitech.ac.jp

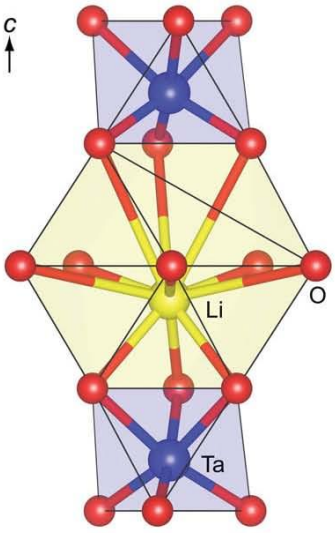


Figure 1. Part of the crystal structure of $LiTaO_3$ viewed along [110], showing coordination polyhedra for Li and Ta. Structural parameters determined by Hsu *et al.* (1997).

TABLE I. Crystal data for $Li(Ta_{0.89}Ti_{0.11})O_{2.945}$.

| Chemical composition | $Li(Ta_{0.89}Ti_{0.11})O_{2.945}$ |
|---|---|
| Space group | *R*3*c* (No. 161) |
| *a*/nm | 0.514 82 9(2) |
| *c*/nm | 1.377 61 2(4) |
| *V*/nm$^3$ | 0.316 21 6(2) |
| *Z* | 6 |
| $D_x$/Mgm$^{-3}$ | 6.943 |

experimental $2\theta$ range from 20.0 to 135.5°, 13 823 total data points, and 4.1 h total experimental time. The crystal-structure models, equidensity isosurfaces of EDD, and two-dimensional EDD maps were visualized with the computer program VESTA (Momma and Izumi, 2008). Distortion parameters for the coordination polyhedra were determined using the computer program IVTON (Balic-Zunic and Vickovic, 1996).

## III. RESULTS AND DISCUSSION

### A. Crystal structure refinements and electron density distributions

Initial structural parameters of $Li(Ta_{0.89}Ti_{0.11})O_{2.945}$ (sample LTTO) were taken from those determined by Hsu *et al.* (1997) for $LiTaO_3$ (space group *R*3*c*). There are three independent sites (i.e., one Li site located at the Wyckoff position 6*a*, one Ta/Ti site at 6*a*, and one O site at 18*b*) in a hexagonal unit cell ($Z = 6$). Structural parameters of all atoms were refined by the Rietveld method using the computer program RIETAN-FP (Izumi and Momma, 2007) with the profile intensity data of LTTO in the whole $2\theta$ range. A Legendre polynomial with 12 adjustable parameters was fitted to background intensities. The split Pearson VII function (Toraya, 1990) was used to fit the peak profiles. The refinement resulted in the reliability (*R*) indices of $R_{wp} = 10.60\%$, $S$ $(=R_{wp}/R_e) = 1.37$, $R_p = 7.49\%$, $R_B = 3.40\%$, and $R_F = 1.51\%$ (Young, 1993). Crystal data are given in Table I, and the final atomic positional parameters and isotropic atomic displacement parameters (ADPs) are given in Table II. The MPF method was subsequently applied, so as to extract structural details and consequently improve the EDD. The EDD with $104 \times 104 \times 276$ pixels in the unit cell, the spatial resolution of which is approximately 0.005 nm, were obtained from the MPF method using the computer programs RIETAN-FP and Dysnomia (Izumi and Momma, 2010). After three REMEDY cycles, $R_{wp}$, $S$, $R_p$, $R_B$, and $R_F$ further decreased to 10.13, 1.31, 6.85, 1.36, and 0.67%, respectively. Subtle EDD changes as revealed by MPF significantly improve the $R_B$ and $R_F$ indices. The decreases in *R* indices demonstrate that the crystal structure can be seen more clearly from EDD instead of from the conventional structural parameters reported in Table II. Observed, calculated, and difference XRPD patterns for the final MPF are plotted in Figure 2(a).

The XRPD peaks of $(Li_{0.977}Eu_{0.023})(Ta_{0.89}Ti_{0.11})O_{2.968}$ (sample LETTO) were successfully indexed with a hexagonal unit cell, the refined unit-cell volume of which was about 0.82% larger than that of $Li(Ta_{0.89}Ti_{0.11})O_{2.945}$. The $Eu^{3+}$ ions were assumed to be randomly distributed over the Li site. The refinement process was very similar to that of LTTO. The Rietveld refinement in the $2\theta$ range from 20.0 to 135.0° resulted in the *R* indices of $R_{wp} = 7.87\%$, $S = 1.22$, $R_p = 6.03\%$, $R_B = 1.72\%$, and $R_F = 1.03\%$. Crystal data are given in Table III, and the final atomic positional parameters and isotropic ADPs are given in Table IV. We also applied the MPF method to obtain lower *R* indices ($R_{wp} = 7.82\%$, $S = 1.21$, $R_p = 6.00\%$, $R_B = 1.20\%$, and $R_F = 0.70\%$) after three REMEDY cycles. Observed, calculated, and difference XRPD patterns for the final MPF are plotted in Figure 2(b).

Figure 3 shows the refined crystal structures of Li $(Ta_{0.89}Ti_{0.11})O_{2.945}$ and $(Li_{0.977}Eu_{0.023})(Ta_{0.89}Ti_{0.11})O_{2.968}$, both of which have been confirmed to be isomorphous with that of $LiTaO_3$. The individual equidensity isosurfaces of 3D EDD (Figure 4) are in reasonably good agreement with the corresponding atom arrangements (Figure 3). The two-dimensional EDD maps on the (110) planes show that the positions of Li and/or Eu atoms are successfully disclosed by the EDD (Figure 5). The electron-density peaks at the Li/Eu site of $(Li_{0.977}Eu_{0.023})(Ta_{0.89}Ti_{0.11})O_{2.968}$ (ca. 0.05 nm$^{-3}$) were

TABLE II. Structural parameters and isotropic atomic displacement parameters ($100 \times B$/nm$^2$) for $Li(Ta_{0.89}Ti_{0.11})O_{2.945}$.

| Site | Wyckoff position | *g* | *x* | *y* | *z* | $100 \times B$/nm$^2$ |
|---|---|---|---|---|---|---|
| Li | 6*a* | 1 | 0 | 0 | 0.2828(9) | 1.6(2) |
| Ta/Ti | 6*a* | 0.89/0.11 | 0 | 0 | 0 | 0.29(7) |
| O | 18*b* | 0.9817 | 0.0471(9) | 0.3261(13) | 0.0974(3) | 0.55(9) |

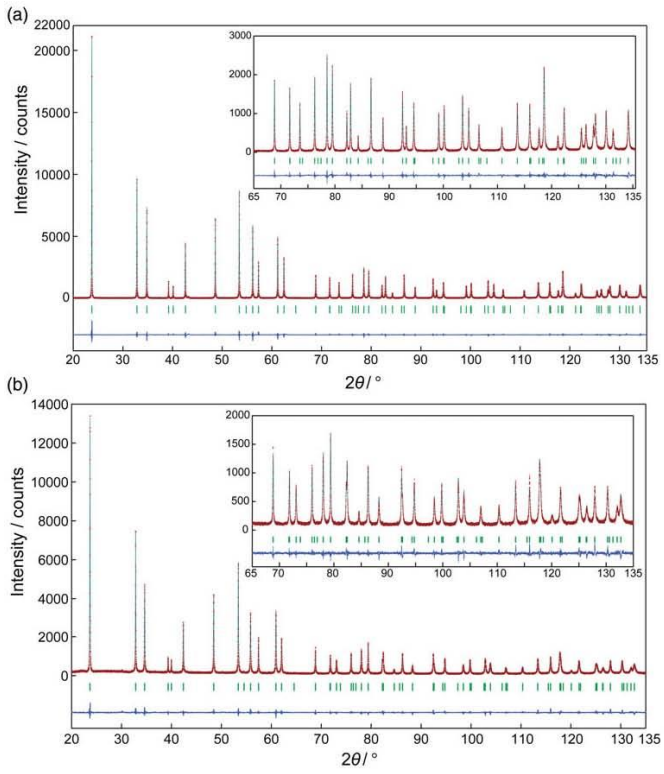


Figure 2. (a) Comparison of the observed diffraction patterns (symbol:+) with the corresponding calculated patterns (upper solid line). The difference curve is shown in the lower part of each diagram. The vertical bars indicate the positions of possible Bragg reflections. The profile intensities collected for samples (a) LTTO. (b) Comparison of the observed diffraction patterns (symbol:+) with the corresponding calculated patterns (upper solid line). The difference curve is shown in the lower part of each diagram. The vertical bars indicate the positions of possible Bragg reflections. The profile intensities collected for samples LETTO.

TABLE III. Crystal data for $(Li_{0.977}Eu_{0.023})(Ta_{0.89}Ti_{0.11})O_{2.968}$.

| Chemical composition | $(Li_{0.977}Eu_{0.023})(Ta_{0.89}Ti_{0.11})O_{2.968}$ |
|---|---|
| Space group | *R3c* (No. 161) |
| *a*/nm | 0.517 71 2(2) |
| *c*/nm | 1.373 50 0(6) |
| *V*/nm$^3$ | 0.318 81 2(3) |
| *Z* | 6 |
| $D_x$/Mgm$^{-3}$ | 7.004 |

higher than those at the Li site of $Li(Ta_{0.89}Ti_{0.11})O_{2.945}$ (ca. 0.03 nm$^{-3}$), although the electron-density peaks at the Ta/Ti sites of these compounds were nearly the same (ca. 1.5 nm$^{-3}$), which indicates that the Li and Eu atoms undoubtedly occupy the same site in the former structure. We found the peak positions of EDD from the 3D pixel data and compared them with the coordinates of all atoms that were determined by the Rietveld method. The positional deviations of all atoms in the unit cell were found to be necessarily less than

TABLE IV. Structural parameters and isotropic atomic displacement parameters ($100 \times B$/nm$^2$) for $(Li_{0.977}Eu_{0.023})(Ta_{0.89}Ti_{0.11})O_{2.968}$.

| Site | Wyckoff position | *g* | *x* | *y* | *z* | $100 \times B$/nm$^2$ |
|---|---|---|---|---|---|---|
| Li/Eu | 6*a* | 0.977/0.023 | 0 | 0 | 0.2307(5) | 0.6(1) |
| Ta/Ti | 6*a* | 0.89/0.11 | 0 | 0 | 0 | 0.46(2) |
| O | 18*b* | 0.9894 | 0.0435(9) | 0.3246(15) | 0.0960(4) | 0.54(7) |

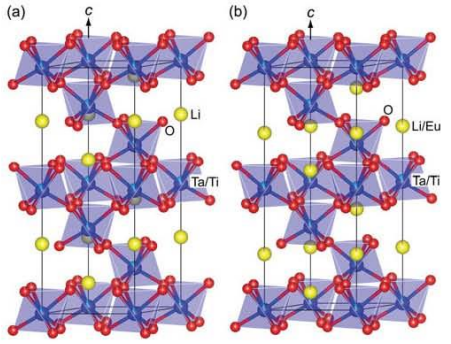


Figure 3. (a) Crystal structure of $Li(Ta_{0.89}Ti_{0.11})O_{2.945}$. Because the occupancy of oxygen site is less than unity, the O atoms are displayed as red circle graphs for occupancy. Blue and cyan bicolor balls are for Ta (blue) and Ti (cyan) sites. (b) Crystal structure of $(Li_{0.977}Eu_{0.023})(Ta_{0.89}Ti_{0.11})O_{2.968}$. Because the occupancy of oxygen site is less than unity, the O atoms are displayed as red circle graphs for occupancy. Blue and cyan bicolor balls are for Ta (blue) and Ti (cyan) sites. Yellow and magenta bicolor balls are for Li (yellow) and Eu (magenta) sites.

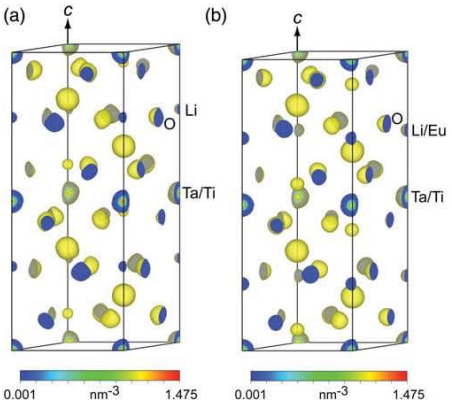


Figure 4. (a) Three-dimensional electron-density distributions determined by MPF with the structural models for $Li(Ta_{0.89}Ti_{0.11})O_{2.945}$. Isosurfaces expressed in smooth shading style for an equidensity level of 0.005 $nm^{-3}$. (b) Three-dimensional electron-density distributions determined by MPF with the structural models for $(Li_{0.977}Eu_{0.023})(Ta_{0.89}Ti_{0.11})O_{2.968}$. Isosurfaces expressed in smooth shading style for an equidensity level of 0.005 $nm^{-3}$.

0.003 nm, which is within the resolution limit of the 3D EDD. We therefore concluded that the present structural models reasonably and satisfactorily represent the corresponding crystal structures of $Li(Ta_{0.89}Ti_{0.11})O_{2.945}$ and $(Li_{0.977}Eu_{0.023})(Ta_{0.89}Ti_{0.11})O_{2.968}$.

### B. Structure description

Selected interatomic distances, together with their standard deviations, are listed in Tables V and VI. The average ionic radii of $Ta^{5+}$ and $Ti^{4+}$ in the six-fold coordination [$r(Ta^{5+}(6)) = 0.064$ nm, $r(Ti^{4+}(6)) = 0.0605$ nm, and $r(O^{2-}(6)) = 0.140$ nm (Shannon, 1976)] predicts the interatomic distance (weighted according to site occupancy) of 0.204 nm for (Ta, Ti)–O. This predicted value is in good agreement with the corresponding average interatomic distances, <(Ta,Ti)–O>, of 0.198 nm for $Li(Ta_{0.89}Ti_{0.11})O_{2.945}$ and 0.199 nm for $(Li_{0.977}Eu_{0.023})(Ta_{0.89}Ti_{0.11})O_{2.968}$. The oxidation state of Li site in $Li(Ta_{0.89}Ti_{0.11})O_{2.945}$ is estimated to be 0.93 by the bond valence sum (Brown and Altermatt, 1985; Brese and O'Keeffe, 1991), which agrees well with 1.0 for $Li^+$. The <Li–O> distance of $[LiO_{12}]$ polyhedron in $LiTaO_3$ is 0.274 nm, which is compatible with those of $Li(Ta_{0.89}Ti_{0.11})O_{2.945}$ (0.270 nm) and $(Li_{0.977}Eu_{0.023})(Ta_{0.89}Ti_{0.11})O_{2.968}$ (0.272 nm).

With $[(Ta,Ti)O_6]$ octahedra in $LiTaO_3$, $Li(Ta_{0.89}Ti_{0.11})O_{2.945}$, and $(Li_{0.977}Eu_{0.023})(Ta_{0.89}Ti_{0.11})O_{2.968}$, the ratios of volumes of the circumscribed sphere and the polyhedron ($=V_S/V_P$) range from 3.13 to 3.15 (Table VII). Because the $V_S/V_P$-value for the regular octahedron is 3.1416 (Makovicky and Balic-Zunic, 1998), the relevant polyhedra can be described as slightly distorted octahedra. The corresponding distortion-parameter values are close to each other among the three compounds, indicating that the $[(Ta,Ti)O_6]$ octahedra are all comparable with each other. There are four ideal polyhedra with 12 vertices; they are cuboctahedron ($V_S/V_P = 1.7772$), anticuboctahedron (1.7772), icosahedron (1.6516), and maximum volume hexagonal prism (2.0944) (Makovicky and Balic-Zunic, 1998). These $V_S/V_P$ values are quite different from those of $[(Li,Eu)O_{12}]$, ranging from 2.26 to 2.31 (Table VII); these polyhedra are distinct from

TABLE V. Selected bond lengths (nm) for $Li(Ta_{0.89}Ti_{0.11})O_{2.945}$.

| | |
|---|---|
| Li–O | 0.1994(4) × 3 |
| Li–O | 0.2611(12) × 3 |
| Li–O | 0.2999(12) × 3 |
| Li–O | 0.3182(6) × 3 |
| <Li–O> | 0.270 |
| (Ta/Ti)–O | 0.1890(5) × 3 |
| (Ta/Ti)–O | 0.2067(5) × 3 |
| <(Ta/Ti)–O> | 0.198 |
| Li–Li | 0.3756(12) |
| (Ta/Ti)–(Ta/Ti) | 0.3756(0) |
| Li–(Ta/Ti) | 0.2992(13) |
| | 0.3053(3) |
| | 0.3376(7) |

TABLE VI. Selected bond lengths (nm) for $(Li_{0.977}Eu_{0.023})(Ta_{0.89}Ti_{0.11})O_{2.968}$.

| | |
|---|---|
| (Li/Eu)–O | 0.2022(3) × 3 |
| (Li/Eu)–O | 0.2432(7) × 3 |
| (Li/Eu)–O | 0.3190(8) × 3 |
| (Li/Eu)–O | 0.3234(5) × 3 |
| <(Li/Eu)–O> | 0.272 |
| (Ta/Ti)–O | 0.1917(6) × 3 |
| (Ta/Ti)–O | 0.2058(6) × 3 |
| <(Ta/Ti)–O> | 0.199 |
| (Li/Eu)–Li/Eu) | 0.3765(6) |
| (Ta/Ti)–(Ta/Ti) | 0.3765(0) |
| (Li/Eu)–(Ta/Ti) | 0.3116(2) |
| | 0.3168(7) |
| | 0.3305(3) |

TABLE VII. Polyhedral distortion parameters for $LiTaO_3$, $Li(Ta_{0.89}Ti_{0.11})O_{2.945}$, and $(Li_{0.977}Eu_{0.023})(Ta_{0.89}Ti_{0.11})O_{2.968}$.

| Compound | Polyhedron | $\Delta$/nm | $r_S$/nm | $V_S$/nm$^3$ | $\sigma$ | $V_P$/nm$^3$ | $V_S/V_P$ |
|---|---|---|---|---|---|---|---|
| $LiTaO_3$* | $[LiO_{12}]$ | 0.064 | 0.269 | 0.0986 | 0.821 | 0.0427 | 2.309 |
| | $[TaO_6]$ | 0.014 | 0.198 | 0.0327 | 1 | 0.0104 | 3.144 |
| $Li(Ta_{0.89}Ti_{0.11})O_{2.945}$ | $[LiO_{12}]$ | 0.024 | 0.269 | 0.0964 | 0.830 | 0.0426 | 2.263 |
| | $[(Ta,Ti)O_6]$ | 0.015 | 0.197 | 0.0321 | 1 | 0.0102 | 3.147 |
| $(Li_{0.977}Eu_{0.023})(Ta_{0.89}Ti_{0.11})O_{2.968}$ | $[(Li,Eu)O_{12}]$ | 0.047 | 0.270 | 0.0981 | 0.826 | 0.0429 | 2.287 |
| | $[(Ta,Ti)O_6]$ | 0.012 | 0.198 | 0.0326 | 1 | 0.0104 | 3.135 |

$\Delta$ = centroid-to-cation distance; $r_S$ = radius of sphere fitted to ligands; $V_S$ = sphere volume; $\sigma$ = sphericity; $V_P$ = volume of coordination polyhedron. For explanation, see Makovicky and Balic-Zunic (1998).
*Structural parameters by Hsu *et al.* (1997).

any of the four ideal ones. As for the O-atom arrangements, all the polyhedra are equivalent since the corresponding $r_S$, $V_S$, $\sigma$, and $V_P$ values are almost the same. On the other hand, the centroid-to-Li/Eu distances ($\Delta$-value) widely vary from 0.024 to 0.064. Accordingly, the prominent difference among the three compounds is the $\Delta$-value for $[(Li,Eu)O_{12}]$. Here we define displacement vector $\boldsymbol{\Delta}$, which connects the centroid to the Li/Eu site of the $[(Li,Eu)O_{12}]$ polyhedron, to more clearly describe the characteristics of the crystal structure not only by the magnitude of $\boldsymbol{\Delta}$ but also by its direction. With $Li(Ta_{0.89}Ti_{0.11})O_{2.945}$ Figure 6(a), the vector $\boldsymbol{\Delta}$ is in the [001] direction with the magnitude of 0.024 nm, whereas the $\boldsymbol{\Delta}$ vectors for $LiTaO_3$ (Figure 1) and $(Li_{0.977}Eu_{0.023})(Ta_{0.89}Ti_{0.11})O_{2.968}$ [Figure 6(b)] are in the [00$\bar{1}$] direction with the magnitudes of, respectively, 0.064 and 0.047 nm.

We have confirmed that the crystal structure of $LiTaO_3$ is flexible with respect to the substitutions of Eu for Li ($Eu/(Li+Eu) \leq 0.023$) and Ti for Ta ($Ti/(Ta+Ti) \leq 0.11$]. The replacement is accompanied by the displacement of the Li/Eu site along the *c*-axis, keeping both $[(Li,Eu)O_{12}]$ and $[(Ta,Ti)O_6]$ polyhedra almost undistorted. The incorporation of $Eu^{3+}$ ions into the crystal structure of $Li[Ta_{0.89}Ti_{0.11}]O_{2.945}$ would cause the overlapping of orbitals with the adjacent anions, resulting in the efficient red-light emission because of the hypersensitive $^5D_0$–$^7F_2$ transition in $Eu^{3+}$ (Nakano *et al.*, 2012). A more detailed discussion on the photoluminescence of this material should be made based on the comparison between the electronic states of $(Li_{0.977}Eu_{0.023})(Ta_{0.89}Ti_{0.11})O_{2.968}$ and $Li(Ta_{0.89}Ti_{0.11})O_{2.945}$, which would be determined from calculation by, for example, density functional theory. The reliable structural parameters, which are indispensable for the calculation, are now available for both compounds.

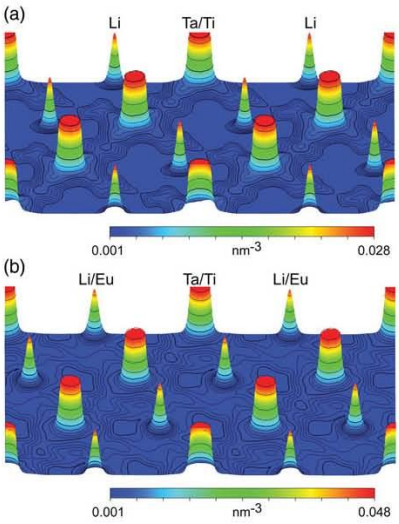


Figure 5. (a) Bird's eye views of electron densities of the Li and Ta/Ti atoms on the (110) planes of $Li(Ta_{0.89}Ti_{0.11})O_{2.945}$. (b) Bird's eye views of electron densities of the Li/Eu and Ta/Ti atoms on the (110) planes of $(Li_{0.977}Eu_{0.023})(Ta_{0.89}Ti_{0.11})O_{2.968}$.

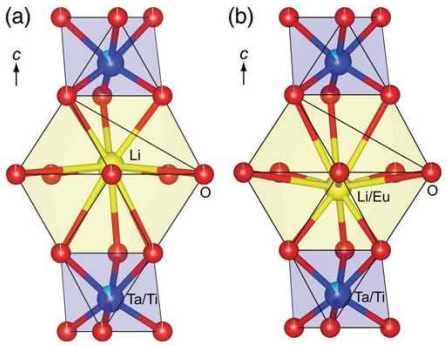


Figure 6. (a) Comparison of parts of the crystal structures $Li(Ta_{0.89}Ti_{0.11})O_{2.945}$, viewed along [110]. (b) Comparison of parts of the crystal structures $(Li_{0.977}Eu_{0.023})(Ta_{0.89}Ti_{0.11})O_{2.968}$, viewed along [110].

## IV. CONCLUSION

We determined the crystal structures of $Li(Ta_{0.89}Ti_{0.11})O_{2.945}$ and $(Li_{0.977}Eu_{0.023})(Ta_{0.89}Ti_{0.11})O_{2.968}$, each of which consists of two types of polyhedra $[(Li,Eu)O_{12}]$ and $[(Ta,Ti)O_6]$. The validity of the structural models was confirmed by the EDD determined by MPF. The two-dimensional EDD maps on (110) showed that the positions of Li/Eu sites were successfully disclosed by the EDD. The substitutions of Eu for Li and Ti for Ta in the crystal structure of $LiTaO_3$ displaced the Li/Eu site along the *c*-axis, keeping the two types of polyhedra almost undistorted.

## ACKNOWLEDGMENTS

The study was partly supported by a Grant-in-Aid for Scientific Research (No. 24360273) from the Japan Society for the Promotion of Science (K. F.) and by a research granted from The Murata Science Foundation (H. N.).

Abrahams, S. C. and Bernstein, J. L. (**1967**). "Ferroelectric lithium tantalate–1. single crystal X-ray diffraction study at 24°C," J. Phys. Chem. Solids **28**, 1685–1692.

Abrahams, S. C., Hamilton, W. C., and Sequeira, A. (**1967**). "Ferroelectric lithium tantalate–2. Single crystal neutron diffraction study at 24°C," J. Phys. Chem. Solids **28**, 1693–1698.

Balic-Zunic, T. and Vickovic, I. (**1996**). "IVTON – a program for the calculation of geometrical aspects of crystal structures and some crystal chemical applications," J. Appl. Crystallogr. **29**, 305–306.

Brese, N. E. and O'Keeffe, M. (**1991**). "Bond-valence parameters for solids," Acta Crystallogr., Sect. B: Struct. Sci. **47**, 192–197.

Brown, I. D. and Altermatt, D. (**1985**). "Bond-valence parameters obtained from a systematic analysis of the inorganic crystal structure database," Acta Crystallogr., Sect. B: Struct. Sci. **41**, 244–247.

Hsu, R., Maslen, E. N., Du Boulay, D., and Ishizawa, N. (**1997**). "Synchrotron X-ray studies of $LiNbO_3$ and $LiTaO_3$," Acta Crystallogr. B Struct. Sci. **53**, 420–428.

Izumi, F. (**2004**). "Beyond the ability of Rietveld analysis: MEM-based pattern fitting," Solid State Ion. **172**, 1–6.

Izumi, F., Kumazawa, S., Ikeda, T., Hu, W.-Z., Yamamoto, A., and Oikawa, K. (**2001**). "MEM-based structure-refinement system REMEDY and its applications," Mater. Sci. Forum **378–381**, 59–64.

Izumi, F. and Momma, K. (**2007**). "Three-dimensional visualization in powder diffraction," Solid State Phenom. **130**, 15–20.

Izumi, F. and Momma, K. (**2010**). "Analyses of magnetic structures and nuclear-density distribution by the structure-refinement and three-dimensional visualization systems RIETAN-FP-VENUS (in Japanese)," J. Vac. Soc. Jpn **53**, 706–712.

Makovicky, E. and Balic-Zunic, T. (**1998**). "New measure of distortion for coordination polyhedra," Acta Crystallogr. B Struct. Sci. **B54**, 766–773.

Megaw, H. D. (**1973**). *Crystal Structures: A Working Approach* (W. B. Saunders Company, Philadelphia). pp. 233–241.

Momma, K. and Izumi, F. (**2008**). "VESTA: A three-dimensional visualization system for electronic and structural analysis," J. Appl. Crystallogr. **41**, 653–658.

Nakano, H., Ozono, K., Hayashi, H. and Fujihara, S. (**2012**). "Synthesis and luminescent properties of a new $Eu^{3+}$-Doped $Li_{1+x}(Ta_{1-z}Nb_z)_{1-x}Ti_xO_3$ red phosphor," J. Am. Ceram. Soc. **95**, 2795–2797.

Ohgaki, M., Tanaka, K., and Marumo, F. (**1989**). "Anharmonic thermal vibration in a crystal of lithium(I) tantalum(V) trioxide, $LiTaO_3$," Mineral. J. **14**, 373–382.

Rietveld, H. M. (**1967**). "Line profiles of neutron powder-diffraction peaks for structure refinement," Acta Crystallogr. **22**, 151–152.

Shannon, R. D. (**1976**). "Revised effective ionic radii and systematic studies of interatomic distances in halides and chalcogenides," Acta Crystallogr. **A32**, 751–767.

Takata, M., Nishibori, E., and Sakata, M. (**2001**). "Charge density studies utilizing powder diffraction and MEM. Exploring of high Tc superconductors, C60 superconductors and manganites," Z. Kristallogr. **216**, 71–86.

Toraya, H. (**1990**). "Array-type universal profile function for powder pattern fitting," J. Appl. Crystallogr. **23**, 485–491.

Young, R. A. (**1993**). "Introduction to the Rietveld method," in The Rietveld Method, edited by R. A. Young (Oxford University Press, Oxford, UK), pp. 1–38.

*Materials Science Forum Vols. 783-786 (2014) pp 2480-2484*

*doi:10.4028/www.scientific.net/MSF.783-786.2480*

# Preparation of textured $Li_{1+x-y}Nb_{1-x-3y}Ti_{x+4y}O_3$ solid solution in a high magnetic field

Hiromi Nakano [1, a], Shiho Suehiro [1,b] Tohru S. Suzuki [2,c]

[1] Toyohashi University of Technology, 1-1 Hibariga-oka, Tempaku, Toyohashi, 441-8580, Japan

[2] National Institute for Materials Science, 1-2-1 Sengen, Tsukuba, 305-0047, Japan

[a]hiromi@crfc.tut.ac.jp, [b] s113517@edu.tut.ac.jp, [c] suzuki.tohru@nims.go.jp

**Keywords:** magnetic field, grain orientation, structure, TEM, superstructure

**Abstract.** In the $Li_2O$-$Nb_2O_5$-$TiO_2$ system, $Li_{1+x-y}Nb_{1-x-3y}Ti_{x+4y}O_3$ ($0.06 \leq x \leq 0.33$, $0 \leq y \leq 0.09$) (LNT) forms with a superstructure, which is the so-called M-phase. In this work, as a first step toward application of the unique qualities of an electro-ceramic with an anisotropic structure, we prepared an oriented LNT balk ceramic by slip casting in a strong magnetic field of 12 T. The direction of the magnetic field was parallel to the casting direction. The compact was densified by cold isostatic pressing and then heated at 1373 K. The obtained specimen was analyzed by X-ray diffraction, scanning electron microscope, and transmission electron microscope. Consequently, the *c*-axis of the LNT powders was aligned parallel to the magnetic field and a high orientation degree was achieved in a strong magnetic field of 12 T.

## Introduction

In the $Li_2O$-$Nb_2O_5$-$TiO_2$ system, $Li_{1+x-y}Nb_{1-x-3y}Ti_{x+4y}O_3$ ($0.06 \leq x \leq 0.33$, $0 \leq y \leq 0.09$) (LNT) forms with a superstructure, and this is known as the M-phase. The superstructure of the M-phase is formed by periodical insertion of an intergrowth layer in a matrix having a trigonal structure. Since the discovery of the M-phase by Castrejon et al. [1, 2], related structures have been investigated [3–6]. The relationship between dielectric property and the period of the intergrowth layer of the M-phase has also been studied [7, 8]. To apply this unique structure as a host material of phosphor, new phosphors were investigated based on LNT or related structures using a conventional electric furnace [9-10].

The controlled development of texture has recently become a topic of interest in ceramic processing, since it allows improved tailoring of the materials' properties. The anisotropy structure of an M-phase solid solution was synthesized, in which rod-precipitates were arranged regularly by a crystal growth method [11]. Oriented thin film of $Li_{1.18}Nb_{0.82}Ti_{0.18}O_3$ on the $Al_2O_3$ (0001) substrate was prepared by a sol-gel and spin-coating process, but the orientation degree was low [12]. A strong magnetic field has been used to control the development of texture, even in weakly magnetic ceramics such as $Al_2O_3$, ZnO, AlN, SiC, and $TiO_2$ [13-17]. The LNT crystal reported here has an asymmetric unit cell and thus very feeble anisotropic magnetic susceptibility.

In this paper, as a first step toward the application of the unique qualities of an electro-ceramic with an anisotropy structure, we prepare highly oriented LNT bulk ceramics by slip casting in a strong magnetic field of 12 T.

## Experimental procedure

The starting materials used were $Li_2CO_3$, $Nb_2O_5$ and $TiO_2$ (> 99.99% grade) to prepare the solid solution of LNT. The compositions of the LNT solid solutions prepared in this work followed the general formula $Li_{1+x-y}Nb_{1-x-3y}Ti_{x+4y}O_3$with $0.05 \leq x \leq 0.18$, $y = 0$, $TiO_2$ content of the specimens was varied from 5 mol% to 20 mol%. The powders were mixed and calcined at 1273 K for 3 h and continuously at 1393 K for over 24 h by an electric furnace in air. The annealing at 1373 K was repeated until the X-ray diffraction (XRD) patterns of resultant powders were free of impurity peaks.

The calcined LNT ceramic with superstructure was pulverized for 1h to16 h by ball-milling (BM) and then used to prepare slurries. Aqueous slurries containing 16.7 wt% solids were prepared with added polyelectrolyte (poly ammonium acrylate A-6114, Toaghosei, Co., Japan) to ensure dispersion. A strong magnetic field of 12 T was applied to the slurries during slip casting. The direction of the magnetic field was parallel to the casting direction. The green compact was densified by cold isostatic pressing at 392 MPa and then sintered at 1373 K for 2 h or 15 h. Structure analysis was carried out by X-ray diffraction (XRD) using a RINT 2500 (Rigaku Co., Ltd. Japan) operating at 40 kV and 200 mA. Microstructure images were observed by scanning electron microscope (SEM) using SU8000 (Hitachi, Tokyo, Japan) operating at 3 kV. High-resolution transmission electron microscope TEM image and selected area electron diffraction (SAED) pattern was observed by 2100 F (JEOL, Tokyo, Japan) operating at 200 kV equipped with energy-dispersed spectroscopy (EDS).

**Results and discussions**

The calcined $Li_{1.18}Nb_{0.82}Ti_{0.18}O_3$ possessed a superstructure, which was determined by XRD. The powders had plate-like shapes and were agglomerated. The agglomerated powders were pulverized to fine particles by ball-milling for 1 h to 16 h. The grain sizes and morphologies of the powders after milling were observed by SEM. The grain size of powder milled for 8 h was obviously larger than that of powder milled for 16 h. The grain sizes were below 5 μm for 16 h. Those powders were used to prepare slurries and make oriented compacts by slip casting in a magnetic field of 12 T. The compact was densified by cold isostatic pressing and then sintered at 1373 K for 15 h.

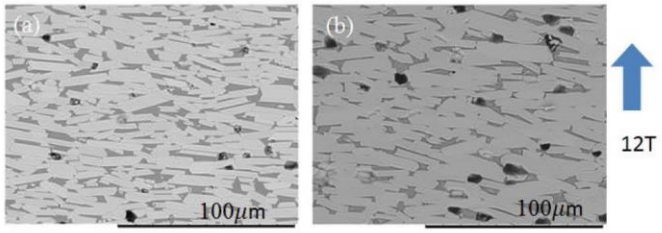


Fig. 1 SEM images of sintered $Li_{1.18}Nb_{0.82}Ti_{0.18}O_3$ specimens parallel to magnetic direction. Powders were used after ball-milling for 8 h (a) and 16 h (b).

Figure 1 shows SEM images of sintered $Li_{1.18}Nb0_{.82}Ti_{0.18}O_3$ specimens on a plane parallel to the magnetic direction. The grains in the oriented compacts after sintering had a plate-like shape. The aspect ratios of the grains in both specimens were 4, although the grain size in the compact using powder milled for 16 h was larger than that milled for 8 h because a small grain grows faster than a larger grain by annealing. Dark-contrast grains indicated $Li_2TiO_3$ solid solution formed as an impurity phase in the $Li_2TiO_3$-$LiNbO_3$ system [18].

Figure 2 shows XRD patterns of random and oriented specimens using powder after ball-milling for 8 h or 16 h. The profiles were taken from the top (T) and side (S) faces, which were perpendicular and parallel to the magnetic d irection, respectively. On the S surface, the peak intensities of (*hk*0) and (*h*00) were high. On the other hand, on the T surface, (00*l*) peaks and satellite peaks were strongly detected. The (104), (108) and (1010) reflections were also detected, which are tilted slightly (less than 6 degrees) from *c*-axis. The adopted lattice constants are $a \cong 0.53$ nm, $c \cong 1.33$ nm [19]. In the BM-8h-T face, many small peaks were detected, marked by triangles in the figure, and used as indices except for (00*l*). The intensities of peaks except for (00*l*) peaks were obviously low in the BM-16h-T face. The peak at around 18 degrees was caused by the $Li_2TiO_3$ solid solution, and the (002) peak was

also strongly oriented. These results show that small grains were preferable for preparation of high-orientation bulk material.

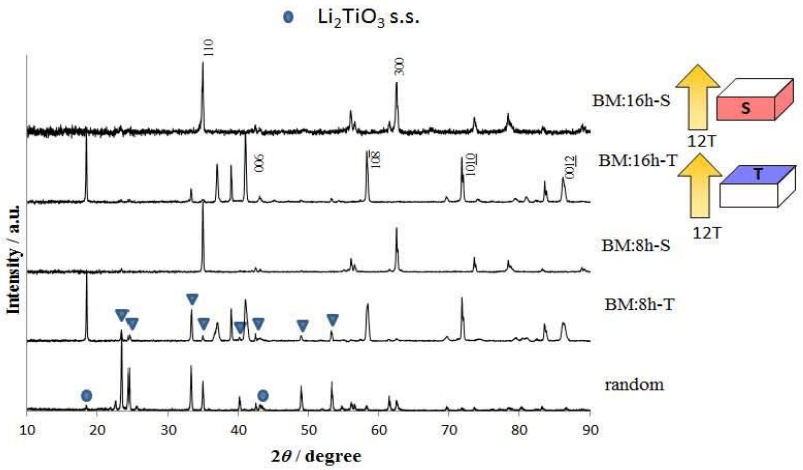


Fig. 2 XRD patterns of random and oriented specimens using powder after ball-milling for 8 h or 16 h.

Next, oriented specimens with various Ti content were synthesized, and the orientation degrees were compared. Chemical compositions of LNT were $Li_{1.05}Nb_{0.95}Ti_{0.05}O_3$ (5 mol%), $Li_{1.11}Nb_{0.89}Ti_{0.11}O_3$ (10 mol%), and $Li_{1.25}Nb_{0.75}Ti_{0.25}O_3$ (20 mol%). Fine powders were used after milling for 16 h by BM. The compact was next densified by cold isostatic pressing and then heated at 1373 K for 2 h.

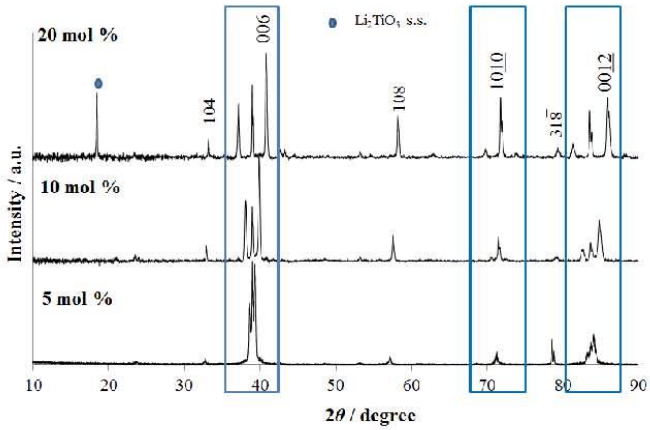


Fig. 3 XRD patterns of oriented specimen with various Ti content (T face).

Figure 3 shows XRD patterns of oriented specimens with various Ti content (T face). The $Li_2TiO_3$ solid solution was not formed in the solid solution system with Ti content below 10 mol%. The 00*l*

peak shifted to a high angle with increasing Ti content because the lattice constant of the *c*-axis became short with increasing Ti content [19]. The satellite peaks were detected around the peaks of (006), (10$\underline{1}$0) and (00$\underline{2}$0). The spacing of satellite reflections was wider with increasing Ti content. This means that the period of the intergrowth layer became narrow with increasing Ti content. The superstructure is formed by periodical insertion of an intergrowth layer in a matrix having a trigonal structure, and the period is controlled by Ti content. The structure was stable due to the formation of the superstructure, which is composed through an anisotropic arrangement of the Ti ions [17]. We noticed that the peaks of (006) and (00$\underline{1}$2) were not a single one, even in the phase of 5 mol%, which is outside the area of the M-phase [3].

Figure 4 shows TEM images taken from the [010] zone axis of grains and selected area electron diffraction (SAED) pattern in the oriented specimens with various Ti content. The SAED pattern showed that the satellite reflections were observed clearly between fundamental reflections along the *c*-axis only in Fig. 4(f). In Fig. 4(b) and 4(d), weak streaks along the *c*-direction were observed. However, TEM images revealed that all specimens had superstructures with a homogeneous period of an intergrowth layer. In the specimen of 5 mol%, a very long period was formed and thus no satellite peak has been previously observed in an XRD pattern without orientation.

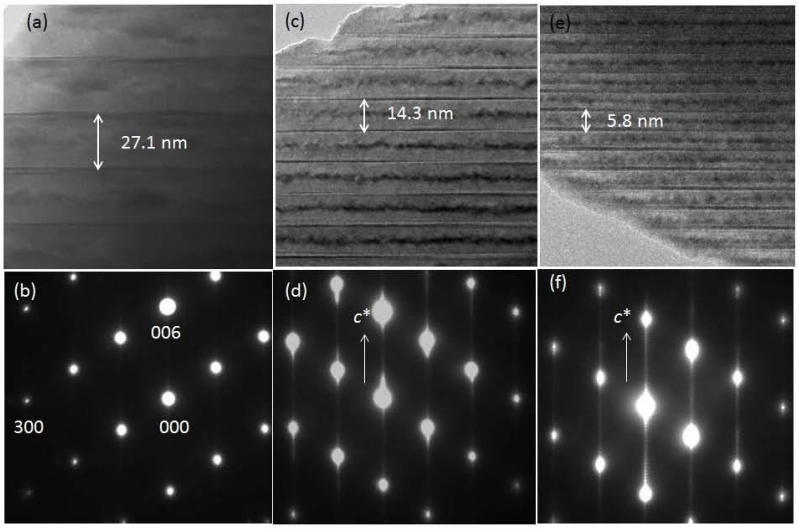


Fig. 4 TEM images and SAED patterns of LNT with Ti content of 5 mol % (a-b), 10 mol % (c-d) and 20 mol % (e-f) taken along the [010] zone axis.

The degree of crystalline orientation was determined by Lotgering factor (LF) [14]. The factor was calculated from the intensity of the T surface with or without a magnetic field. The results revealed that LF is increasing with degreasing the Ti content. In the specimen of 5 mol%, orientation degree of 85% was achieved.

The electric resistivity was measured on the S face and T face only recently. An anisotropic electric property appeared obviously in the oriented bulk ceramics like a single crystal. The electric resistivity on the S face is higher than that on the T face. The specimen with large Ti content showed lower electric resistivity. The intergrowth layers might form an electric conduction path. The detailed data of the electric properties will be reported elsewhere near future.

## Conclusion

Oriented balk ceramic has been successfully prepared in the $Li_2O$-$Nb_2O_5$-$TiO_2$ system, which has a superstructure as the M-phase. The calcined LNT powder with superstructure was pulverized by ball-milling and then used to prepare slurries. A strong magnetic field of 12 T was applied to the slurries during slip casting. The direction of the magnetic field was parallel to the casting direction. Consequently, the *c*-axis of the LNT powders was aligned parallel to the magnetic field. Satellite reflections around (00*l*) were detected clearly along the *c*-axis in the oriented crystalline phase even at Ti 5 mol%, which was caused by the periodic insertion of the intergrowth layer parallel to the (00*l*) plane. An anisotropic property appeared obviously in the oriented bulk ceramics. The electric resistivity on the S face, parallel to the *c*-direction, is higher than that on the T face, perpendicular to the *c*-direction.

## Acknowledgement

This work was partially supported by a Grant-in-Aid for Scientific Research (c) No. 25420709 by the Japan Society for the Promotion of Science.

## References

[1] M. E. Villafuerte-Castrejon, J. A. Gracia, E. Cisneros, R. Valenzuela, A. R. West, J. Brit. Ceram. Soc. 83 (1984) 143-145.
[2] M. E. Villafuerte-Castrejon, A. Aragon-Pina, R. Valenzuela, A. R. West, J. Solid State Ceram. 71 (1987) 103 -108.
[3] R. I. Smith, A. R. West, Mat. Res. Bull. 27 (1992) 277-285.
[4] H. Hayashi, H. Nakano, K. Suzumura, K. Urabe, A. R. West, Forth Ceram. Soc. 2 (1995) 391-398.
[5] H. Hayashi, K. Urabe, K. Niihara, Key Engineering materials 161-163 (1999) 501-504.
[6] L. Farber, I. Levin, A. Borisevichi, I. E. Grey, R. S. Roth, P. K. Davies, J. Solid State Chem. 166 (2002) 81-90.
[7] A. Y. Borisevich, P. K. Davies, J. Am. Ceram. Soc. 85 (2002) 573-578.
[8] Y. Yamamoto, H. Hayashi, T. Sekino, T. Nakayama, T. Kondo, M. Wada, T. Adachi, K. Niihara, Materials Research Innovations 7 (2003) 74-79.
[9] H. Hayashi, H. Nakano, J. Alloys and Compd. 502 (2010) 360-364.
[10] H. Hayashi, H. Nakano, M. I. Jones, J. Ceram. Soc. Jpn. 118(3) (2010) 226-230.
[11] Y. Yamamoto, T. Sekino, T. Kusunose, T. Nakayama, Y. Morimoto, S. Miyazawa, K. Niihara, J. Cry. Growth 264 (2004) 445-451.
[12] Y. Yamamoto, T. Sekino, H. Hayashi, T. Nakayama, T. Kusunose, K. Niihara, Mater. Lett. 57 (2003) 2702-2706.
[13] Y. Kinemuchi, H. Nakano, H. Kaga, S. Tanaka, K. Uematzu, K.Watari, J. Am. Ceram. Soc. 94 (2011) 2339-2343.
[14] T. S. Suzuki, Y. Sakka, Scripta Materiallia 52 (2005) 583-586.
[15] T. S. Suzuki, T. Uchikoshi, Y. Sakka, J. Europ. Ceram. Soc. 30 (2010) 2813-2717.
[16] L. Zhang, J. Vleugels, O. V. Biest, J. Am. Ceram. Soc. 93(10) (2010) 3148-3152.
[17] T. S. Suzuki, Y. Sakka, Jpn. J. Appl. Phys. 41 (2002) L1272-1274.
[18] M. E. Villafuerte-castrejon, J. A. Garcia, E. Cisneros, R. Valenzuela, A. R. West, Br. Ceram. Trans. J. 83 (1984) 143-145.
[19] H. Nakano, T. Saji, M. Yuasa, S. Miyake, M. Mabuchi, J. Ceram. Soc. Jpn. 119(11) (2011) 808-812.

Materials Research Bulletin 60 (2014) 766–770

Contents lists available at ScienceDirect

Materials Research Bulletin

journal homepage: www.elsevier.com/locate/matresbu

# Synthesis and luminescence enhancement of $Eu^{3+}$, $Sm^{3+}$ co-doped $Li_{1.11}Ta_{0.89}Ti_{0.11}O_3$ phosphor

Hiromi Nakano [a,*], Shohei Furuya [a], Koichiro Fukuda [b], Suzuya Yamada [c]

[a] Department of Environmental and Life Sciences, Toyohashi University of Technology, Toyohashi 441-8580, Japan
[b] Department of Materials Science and Engineering, Nagoya Institute of Technology, Nagoya 466-8555, Japan
[c] Central Research Institute, Denki Kagaku Kogyo K.K., Machida 194-8560, Japan

ARTICLE INFO

*Article history:*
Received 14 February 2014
Received in revised form 22 July 2014
Accepted 19 September 2014
Available online 29 September 2014

*Keywords:*
Oxides
Luminescence
X-ray diffraction
Phosphors

ABSTRACT

Phosphors based on the $Li_{1+x}Ta_{1-x}Ti_xO_3$ solid solutions ($0.05 \le x \le 0.25$) as host materials were investigated. The optimal composition of the host for red-light emitting phosphor was found to be $Li_{1.11}Ta_{0.89}Ti_{0.11}O_3$ ($x = 0.11$) when activated with $Eu^{3+}$. In this work, in order to further enhance the emission intensity, a series of $Eu^{3+}$- and $Sm^{3+}$-doped $Li_{1.11}Ta_{0.89}Ti_{0.11}O_3$ phosphors was synthesized by solid-state reaction. The phosphor doped with 2.5 wt% $Eu_2O_3$ and 0.1 wt% $Sm_2O_3$ showed the highly efficient red-light emission upon excitation at 399 nm, with the internal quantum efficiency being 98%. Its PL intensity was *ca.* 1.4 times higher than that of the 2.5 wt% $Eu^{3+}$-doped $Li_{1.11}Ta_{0.89}Ti_{0.11}O_3$ phosphor, indicating that the small amount of $Sm^{3+}$ acted as an effective sensitizer.



## 1. Introduction

In the ternary $Li_2O$–$Nb_2O_5$–$TiO_2$ system, the compounds with the general composition $Li_{1+x-y}Nb_{1-x-3y}Ti_{x+4y}O_3$ (LNT), known as the "*M*-phase" solid solutions, form superstructures, where M = Nb or Ta with $0.06 \le x \le 0.33$ and $0 \le y \le 0.17$. Since the discovery of the *M*-phase for LNT by Castrejon et al. [1,2], the physical properties as well as the crystal structures of the solid solutions have been investigated in detail [3–6]. The *M*-phase superstructures have been found to be formed by the periodical insertion of intergrowth layers in the matrix having a trigonal structure. The relationship between dielectric properties and periods of the intergrowth layers of the *M*-phase have been studied successively [7,8].

The LNT compounds have been applied to the host materials of new phosphors [9,10]. The photoluminescence (PL) intensities at 625 nm were much higher for LNT:$Eu^{3+}$ than for $LiNbO_3$:$Eu^{3+}$ [11,12]. The *RE*-doped $LiTaO_3$ phosphors have also been reported by other groups, where *RE* = $Pr^{3+}$ [13], $Er^{3+}$ [14], $Tb^{3+}$ [15] $Eu^{3+}$ [16] and $Tm^{3+}$ [17]. Recently, we have succeeded in synthesizing new red phosphors based on the quaternary $Li_{1+x}(Ta_{1-z}Nb_z)_{1-x}Ti_xO_3$ (LTNT, $0 \le x \le 0.25$, $0 \le z \le 1.0$) solid solutions as the host materials [18]. We have confirmed that the superstructures are actually formed in the higher Ti content regions of $0.06 \le x \le 0.2$ in the Ta-containing system ($0.05 \le z \le 0.175$). The PL intensities of the LTNT:$Eu^{3+}$ phosphors were not affected by the structural distortions induced by the superstructure formation, but dependent on the *x*- and *z*-values as well as the concentration of $Eu^{3+}$.

The *RE* (= $Sm^{3+}$, $Er^{3+}$, $Dy^{3+}$ and/or $Tm^{3+}$) doped $Li_{1+x}Ta_{1-x}Ti_xO_3$ (LTT) phosphors, showing various emission colors, have been synthesized by the conventional electric furnace in air to compared their PL properties to those of the LNT phosphors [19]. We have concluded that the small differences in environment of the dopant sites between the host materials of LNT and LTT eventually affect the emission energy of the $RE^{3+}$ ions. In the LTT host materials, the most effective activator was $Eu^{3+}$. The internal quantum efficiency attained the value of over 84% for the host composition of $Li_{1.11}Ta_{0.89}Ti_{0.11}O_3$ ($x = 0.11$) [19]. The $Li_{1.11}Ta_{0.89}Ti_{0.11}O_3$:$Eu^{3+}$ phosphor, when excited by the near ultraviolet (UV) light, emits strong red light, hence it could be suitable for the backlight of projectors; the backlight contains an array of red, green, and blue LEDs whose combined light forms white light [20]. To apply the LTT-host phosphors to the backlight, much higher PL intensities are required. Because the $Sm^{3+}$ ions have been reported to act as sensitizers for various types of Eu-doped phosphors [21–24], we have tried to enhance the emission intensities of the LTT phosphors by co-doping of $Eu^{3+}$ and $Sm^{3+}$. We have successfully prepared the red-light emitting $Li_{1.11}Ta_{0.89}Ti_{0.11}O_3$:$Eu^{3+}$, $Sm^{3+}$ phosphors with the improved PL properties.

* Corresponding author. Tel.: +81 532446606; fax: +81 532446610.
*E-mail address:* hiromi@crfc.tut.ac.jp (H. Nakano).

http://dx.doi.org/10.1016/j.materresbull.2014.09.059
0025-5408/

## 2. Experimental procedure

The starting materials used were $Li_2CO_3$, $Ta_2O_5$, and $TiO_2$ (>99.9% grade) powders to prepare the solid solutions of $Li_{1+x-y}Ta_{1-x-3y}Ti_{x+4y}O_3$. As activators, $Eu_2O_3$ and/or $Sm_2O_3$ were doped in the host materials. The mixed and pressed powders were pre-annealed at 1273 K for 3 h to drive off $CO_2$, and continuously sintered at 1423 K for 15 h using a conventional electric furnace.

Structural analysis was carried out by X-ray powder diffraction (XRD) using a RINT 2500 (Rigaku Co., Ltd. Tokyo, Japan) operating at 40 kV and 200 mA. Microstructure images were observed by a scanning electron microscope (SEM) (model SU8000, Hitachi Co., Ltd. Tokyo, Japan) operating at 3 kV. The crystal-structure models, the structural parameters of which were taken from those determined in a previous study [25], were visualized with the computer program VESTA [26]. Excitation and emission spectra were obtained by a PL spectrometer (model FP-6500, JASCO International Co., Ltd. Tokyo, Japan). Quantum efficiency was measured by a spectral radiometer (model MCPD-7000, Otsuka Electronics Co., Ltd. Osaka, Japan).

## 3. Results and discussion

### 3.1. Photoluminescence property

Phosphors based on the $Li_{1+x-y}M_{1-x-3y}Ti_{x+4y}O_3$ (M: Ta, Nb, $0 \le x \le 0.25$, $y = 0$) solid solutions as host materials were investigated. The optimal composition of the host material for a red phosphor was found to be $Li_{1.11}Ta_{0.89}Ti_{0.11}O_3$ (M = Ta, $x = 0.11$ and $y = 0$) by $Eu^{3+}$-ion doping, as previously reported [18]. The PL spectrum of the $Li_{1.11}Ta_{0.89}Ti_{0.11}O_3$:$Eu^{3+}$ phosphor is characterized by the charge transfer band in the range of 220–340 nm and sharp excitation peaks in the near-UV to green light (Fig. 1). Red-light emission at an excitation wavelength of 399 nm would be caused by the intraconfigurational $^7F_0$–$^5L_6$ transition. The maximum emission peak at around 624 nm would be associated with the hypersensitive electric dipole $^5D_0$–$^7F_2$ transition in the $Eu^{3+}$ ion.

Fig. 2 shows the changes in emission intensity as well as internal- and external-quantum efficiencies against the $Eu_2O_3$ content. We confirmed that the phosphor doped with $Eu_2O_3$ at 2.5 wt% had the highest emission intensity and internal quantum efficiency (84%). Over the value of 2.5 wt%, the PL intensity of the phosphor decreased at the point where concentration quenching occurred [22]. The external quantum efficiency remained low at even high concentrations of $Eu_2O_3$ content, which must be caused by the low absorptivity due to the forbidden 4f–4f transition of the

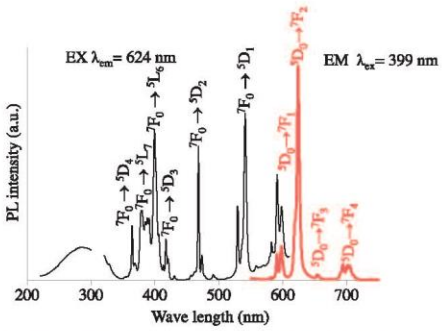


Fig. 1. Excitation and emission spectra of $Li_{1.11}Ta_{0.89}Ti_{0.11}O_3$:$Eu^{3+}$ phosphor.

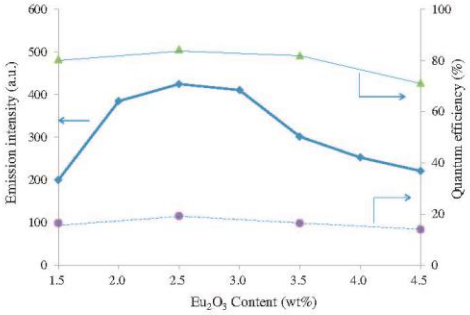


Fig. 2. Changes in emission intensity and internal- and external-quantum efficiencies against $Eu_2O_3$ content in $Li_{1.11}Ta_{0.89}Ti_{0.11}O_3$:$Eu^{3+}$.

$Eu^{3+}$ ion. The peak of the wavelength and its half-value width showed steady values of 624 nm and 5 nm, respectively, regardless of the $Eu_2O_3$ content.

Next, in order to clarify the effect of $Sm^{3+}$-ion doping on the photoluminescence properties, the $Sm_2O_3$ content was varied from 0 to 0.25 wt%, with a fixed $Eu_2O_3$ concentration of 2.5 wt%. We determined the internal and external quantum efficiencies (Fig. 3). The results show that the co-doped phosphor with $Sm_2O_3$ at 0.1 wt % showed the highest PL intensity, with the internal quantum efficiency being 98%. The PL intensity of this phosphor, doped with $Eu_2O_3$ at 2.5 wt% and $Sm_2O_3$ at 0.1 wt%, was *ca.* 1.4 times higher than that of the 2.5 wt% $Eu^{3+}$-doped $Li_{1.11}Ta_{0.89}Ti_{0.11}O_3$ phosphor, indicating that the small amount of $Sm^{3+}$ acted as an effective sensitizer. The external quantum efficiency was slightly improved up to *ca.* 20%, although the improvement degree was still unsatisfactorily low.

The excitation and emission spectra of the $Li_{1.11}Ta_{0.89}Ti_{0.11}O_3$-host phosphors with various $Sm_2O_3$ concentrations are shown in Fig. 4. The emission peak at 624 nm was obviously enhanced by the $Sm^{3+}$-ion doping at 0.1 wt%. The shift of wavelength of the peak corresponding to the $^7F_0$–$^5L_6$ transition of $Eu^{3+}$ was not detectable. The intensity of the excitation peak at 399 nm was enhanced by the $Sm^{3+}$-ion doping. The peak at 410 nm would be also induced by the $Sm^{3+}$-ion doping, which corresponds to the $^6H_{5/2}$–$^4K_{11/2}$ transition of $Sm^{3+}$. We compared the emission spectra of the three-types of phosphors $Li_{1.11}Ta_{0.89}Ti_{0.11}O_3$:$Eu^{3+}$, $Li_{1.11}Ta_{0.89}Ti_{0.11}O_3$:$Eu^{3+}$, $Sm^{3+}$,

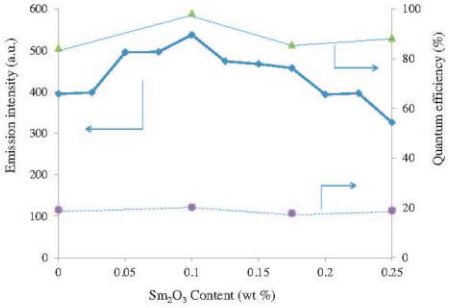


Fig. 3. Changes in emission intensity and internal- and external-quantum efficiencies against $Sm_2O_3$ content.

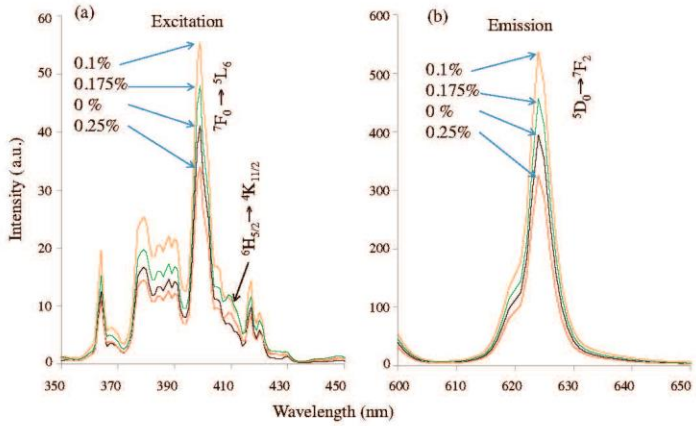


**Fig. 4.** (a) Excitation and (b) emission spectra of $Li_{1.11}Ta_{0.89}Ti_{0.11}O_3:Eu^{3+},Sm^{3+}$ phosphor with various amounts of $Sm_2O_3$ content.

and $Li_{1.11}Ta_{0.89}Ti_{0.11}O_3:Sm^{3+}$ (Fig. 5) in order to confirm the effect of $Sm^{3+}$-ion doping on these spectra. The $Li_{1.11}Ta_{0.89}Ti_{0.11}O_3:Sm^{3+}$ phosphor was synthesized with $Sm_2O_3$ doping at 2.5 wt%, as previously reported [19]. No emission peak of the co-doped phosphor was observed at around 607 and 650 nm by the transition of the $Sm^{3+}$ ion. These results indicate that the $Sm^{3+}$ ion must act as a sensitizer, which induces the energy transfer from $Sm^{3+}$ to $Eu^{3+}$ in the $Eu^{3+}$-doped phosphor. The mechanism of the energy-transfer process from $Sm^{3+}$ to $Eu^{3+}$ has been reported [21–24], which should be also applicable to the present $Li_{1.11}Ta_{0.89}Ti_{0.11}O_3:Eu^{3+}$, $Sm^{3+}$ phosphor. When the $Sm^{3+}$ is excited with 399 nm, the initial population relaxes finally to the $^4G_{5/2}$ level. Part of the energy in the $^4G_{5/2}$ level of $Sm^{3+}$ is transferred to the $^5D_0$ level of $Eu^{3+}$. The energy transfer from $Sm^{3+}$ to $Eu^{3+}$ is almost irreversible because of difference in the two energy height. The energy resonance transfer enhances the population of $^5D_0$ level. Hence, the highly efficient red-light emission due to $Eu^{3+}$ would occur through the $^5D_0$–$^7F_J$ transition, without the emission due to $Sm^{3+}$. Because of the highly efficient red-light emission for the present $Li_{1.11}Ta_{0.89}Ti_{0.11}O_3:Eu^{3+}$, $Sm^{3+}$phosphor, it could be potentially available for a part of the combined phosphors of backlight.

### 3.2. Grain morphology and phase identification

Fig. 6 shows SEM images of the as-sintered specimens for $Li_{1.11}Ta_{0.89}Ti_{0.11}O_3$-host phosphors with various amounts of $Sm_2O_3$ content. The grain sizes were almost the same, and no abnormal grain growth occurred by $Sm^{3+}$-ion doping. This result indicates that a small amount of $Sm^{3+}$ ions was homogeneously distributed after the powder-mixing process. Indeed, in our pre-experimental stage, abnormal grain growth occurred when unwell-mixed powders were used for the starting materials.

Fig. 7 shows the XRD patterns of $Li_{1.11}Ta_{0.89}Ti_{0.11}O_3:Eu^{3+}$, $Sm^{3+}$ phosphors with various $Sm_2O_3$ concentrations. The secondary phases were not detectable even in the phosphor doped with $Sm_2O_3$ at 0.25 wt%. Each of the diffraction patterns, which was successfully indexed with a rhombohedral unit cell, is in accord with the $LiTaO_3$-type structure with the space group $R3c$. These

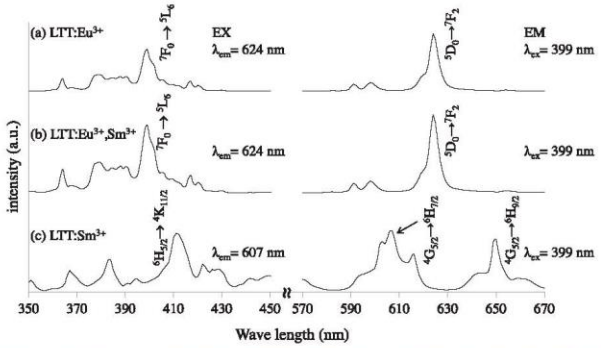


**Fig. 5.** Excitation and emission spectra of (a) Eu-doped, (b) Eu- and Sm-doped, and (c) Sm-doped $Li_{1.11}Ta_{0.89}Ti_{0.11}O_3$ phosphors.

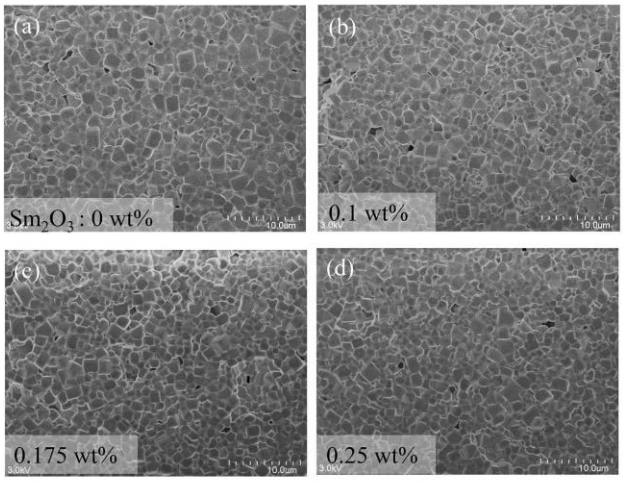


**Fig. 6.** SEM images of $Li_{1.11}Ta_{0.89}Ti_{0.11}O_3:Eu^{3+},Sm^{3+}$ phosphor with various $Sm_2O_3$ concentrations (a) 0 wt%, (b) 0.1 wt%, (c) 0.175 wt%, and (d) 0.25 wt%.

results show that the *RE* ions were diffused into the host materials so as to be homogeneously distributed. In our previous report, we actually confirmed that the sintering time of 15 h was sufficient for the homogeneous distribution of the *RE* ions in the host materials [19].

Here, we discuss the relationship between the crystal structures and PL intensities of the phosphors. The emission from $Eu^{3+}$ ions is primarily subject to the interaction with the adjacent anions due to overlapping of orbitals. Thus, the PL intensity of the phosphor must be closely related to the local environment of the $Eu^{3+}$ site in the crystal. The crystal structures of $Li_{1.11}Ta_{0.89}Ti_{0.11}O_3$ and $Li_{1.11}Ta_{0.89}Ti_{0.11}O_3:Eu^{3+}$ were determined using the Rietveld method [25]. The validity of the structural models were confirmed by the maximum-entropy-method based pattern fitting method, which clearly indicated that the $Ti^{4+}$ ion and $Eu^{3+}$ ion were displaced in the $Ta^{5+}$ site and $Li^+$ site, respectively. The $Eu^{3+}$ ions may occupy not only the $Li^+$ site but also the $Ta^{5+}$ site for the crystals with the relatively high concentration of $Eu^{3+}$ [27]. Fig. 8 shows parts of the refined crystal structures, together with the bond lengths of Li(Eu)—O, for $Li_{1.11}Ta_{0.89}Ti_{0.11}O_3$ and $Li_{1.11}Ta_{0.89}Ti_{0.11}O_3:Eu^{3+}$. The polyhedral distortions of $[Li(Eu)O_{12}]$ were determined from the ratios of circumscribed sphere volumes ($V_s$) and the coordination polyhedron volumes ($V_p$) [25]. The distortion-parameter values ($= V_s/V_p$) of $Li_{1.11}Ta_{0.89}Ti_{0.11}O_3$ and $Li_{1.11}Ta_{0.89}Ti_{0.11}O_3:Eu^{3+}$ were, respectively, 2.263 and 2.287, which were close to each other. On the other hand, the centroid-to-Li(Eu) distances ($\Delta$-value) widely varied from 0.024 for the former compound to 0.047 for the latter [25]. These results indicate that the replacement of $Li^+$ by $Eu^{3+}$ was mainly accompanied by the displacement of the Li(Eu) site along the *c*-axis, keeping the $[Li(Eu)O_{12}]$ polyhedra almost undistorted. As a result, the prominent difference in the environment of Li(Eu) ion between the two compounds is the $\Delta$-value for $[Li(Eu)O_{12}]$; the displacement magnitude is larger for $Li_{1.11}Ta_{0.89}Ti_{0.11}O_3:Eu^{3+}$ than for $Eu^{3+}$-free $Li_{1.11}Ta_{0.89}Ti_{0.11}O_3$. The displacement of $Eu^{3+}$ position from the centroid of $[EuO_{12}]$ polyhedra must contribute to the highly enhanced intraconfigurational $^7F_0$–$^5D_1$ transition when excited

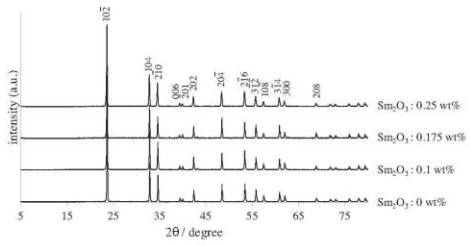


**Fig. 7.** XRD patterns of $Li_{1.11}Ta_{0.89}Ti_{0.11}O_3:Eu^{3+},Sm^{3+}$ phosphor with various $Sm_2O_3$ concentrations.

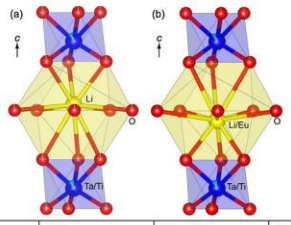


| bond length | LTT | LTT:$Eu^{3+}$ | direction |
|---|---|---|---|
| Li(Eu)-O × 3 (nm) | 0.1994(4) | 0.2022(3) | |
| Li(Eu)-O × 3 (nm) | 0.2999(12) | 0.3190(8) | |
| Li(Eu)-O × 3 (nm) | 0.2611(12) | 0.2432(7) | *c*-axis |
| Li(Eu)-O × 3 (nm) | 0.3182(6) | 0.3234(5) | *c*-axis |

**Fig. 8.** Parts of the crystal structures of (a) $Li(Ta_{0.89}Ti_{0.11})O_{2.945}$ and (b) $(Li_{0.977}Eu_{0.023})(Ta_{0.89}Ti_{0.11})O_{2.968}$, viewed along [110], together with the bond lengths of Li(Eu)—O. Note that chemical compositions are determined by Rietvelt method.

by the near-UV light. With the present $Li_{1.11}Ta_{0.89}Ti_{0.11}O_3:Eu^{3+}, Sm^{3+}$ phosphor, the $Sm^{3+}$ ion would be also located at the Li site because of its similar ionic radius. The displacements of $Eu^{3+}$ and $Sm^{3+}$ positions along the c-axis from the centroid of $[(Eu,Sm)O_{12}]$ polyhedra could be closely related to the enhancement mechanism of the red-light emission through the energy transfer from $Sm^{3+}$ to $Eu^{3+}$. The detail of this mechanism from view point of the structural distortion is still unclear, and should be investigated further.

## 4. Conclusion

The $Eu^{3+}$- and $Sm^{3+}$-doped $Li_{1.11}Ta_{0.89}Ti_{0.11}O_3$ phosphors have been successfully synthesized by the solid-state reaction. The highest PL intensity was attained for the phosphor doped with $Eu_2O_3$ at 2.5 wt% and $Sm_2O_3$ at 0.1 wt%. The red light was efficiently emitted at 624 nm when excited by the near-UV light, with the internal quantum efficiency of 98%. The PL intensity was *ca.* 1.4 times higher for $Li_{1.11}Ta_{0.89}Ti_{0.11}O_3:Eu^{3+}$, $Sm^{3+}$ than for $Li_{1.11}Ta_{0.89}Ti_{0.11}O_3:Eu^{3+}$, indicating that the small amount of $Sm^{3+}$ acted as an effective sensitizer. The high efficiency of red-light emission was ascribed to the energy transfer from $Sm^{3+}$ to $Eu^{3+}$, and the subsequent $^5D_0$–$^7F_J$ transition in $Eu^{3+}$.

## Acknowledgement

This work (H.N.) was partially supported by a Grant-in-Aid for Scientific Research (c) No. 25420709 by the Japan Society for the Promotion of Science.

## References

[1] M.E.V. -Castrejon, J.A. Gracia, E. Cisneros, R. Valenzuela, A.R. West, J. Br. Ceram. Soc. 83 (1984) 143–145.
[2] M.E.V. -Castrejon, A.A. -Pina, R. Valenzuela, A.R. West, J. Solid State Chem. 71 (1987) 103–108.
[3] R.I. Smith, A.R. West, Mater. Res. Bull. 27 (1992) 277–285.
[4] H. Hayashi, H. Nakano, K. Suzumura, K. Urabe, A.R. West, Forth Euro. Ceram. Soc. 2 (1995) 391–398.
[5] H. Hayashi, K. Urabe, K. Niihara, Key Eng. Mater. 501 (1999) 161–163.
[6] L. Farber, I. Levin, A. Borisevichi, I.E. Grey, R.S. Roth, P.K. Davies, J. Solid State Chem. 166 (2002) 81–90.
[7] A.Y. Borisevich, P.K. Davies, J. Am. Ceram. Soc. 85 (10) (2002) 573–578.
[8] Y. Yamamoto, H. Hayashi, T. Sekino, T. Nakayama, T. Kondo, M. Wada, T. Adachi, K. Niihara, Mater. Res. Innovations 7 (2003) 74–79.
[9] H. Hayashi, H. Nakano, J. Alloys. Compd. 502 (2010) 360–364.
[10] H. Hayashi, H. Nakano, M.I. Jones, J. Ceram. Soc. Jpn. 118 (3) (2010) 226–230.
[11] H. Naknao, K. Ozono, T. Saji, S. Miyake, H. Hiroyuki, Opt. Mater. 35 (2013) 2045–2048.
[12] H. Nakano, S. Suehrio, T. Saji, S. Miyake, J. Alloys. Compd. 552 (2013) 475–479.
[13] W. Gryk, D. Dyl, W.R. -Romanowski, M. Grinberg, J. Phys.: Condens. Matter 17 (2005) 5381–5395.
[14] S.M. Kostritskii, D.B. Maring, R.F. Tavlykasev, R.V. Ramaswamy, Appl. Phys. Lett. 76 (16) (2000) 2161–2163.
[15] W.R. -Romanowski, S. Golab, G.D. -Dzik, M.N. Paltnikov, N.V. Sidorov, J. Appl. Lett. 78 (23) (2001) 3610–3611.
[16] G. Gasparotto, M.A. Cebin, M.S. Goes, S.A.M. Lima, M.R. Davolos, J.A. Varela, C.O.P. -Santos, M.A. Zaghete, J. Appl. Phys. 106 (2009) 3506–3509.
[17] I. Sokolska, W.R. -Romanowski, S. Golab, M. Baba, M. Swirkowicz, T. Lukasiewicz, J. Phys. Chem. Solids 61 (2000) 1573–1581.
[18] H. Nakano, K. Ozono, H. Hayashi, S. Fujihara, J. Am. Ceram. Soc. 95 (9) (2012) 2795–2797.
[19] H. Nakano, S. Suehiro, S. Furuya, H. Hayashi, S. Fujihara, Materials 6 (2013) 2768–2776.
[20] T. Ishiwatari, Jpn. Energy Technol. Intell. (JETI) 55 (7) (2007) 8 (in Japanese).
[21] G.-H. Lee, T.-H. Kim, C. Yoon, S. Kang, J. Lumin. 128 (2008) 1922–1926.
[22] Y.-H. Won, H.S. Jang, W.B. Im, D.Y. Jeon, J. Electrochem. Soc. 155 (9) (2008) J226–J229.
[23] P. Li, Z. Xu, S. Zhao, F. Zhang, Y. Wang, Mater. Res. Bull. 47 (2012) 3825–3829.
[24] P.R. Biju, G. Jose, V. Thomas, V.P.N. Nampoori, N.V. Unnikrishnan, Opt. Mater. 24 (2004) 671–677.
[25] T. Uchida, S. Suehiro, T. Asaka, H. Nakano, K. Fukuda, Powder Diffr. 28 (3) (2013) 178–183.
[26] K. Momma, F. Izumi, J. Appl. Crystallogr. 44 (2011) 1272–1276.
[27] G. Gasparotto, M.A. Cebin, M.S. Goes, S.A.M. Lima, M.R. Davolos, J.A. Varela, C.O. Paiva-Santos, M.A. Zaghete, J. Appl. Phys. 106 (2009) 63509.

# 白色 LED 用近紫外励起赤色蛍光体の創成と母体構造の特徴

中 野 裕 美[*1]・福 田 功一郎[*2]

*Hiromi Nakano・Koichiro Fukuda*

■ [*1] 豊橋技術科学大学研究基盤センター　教授　博士(工学)　[*2] 名古屋工業大学大学院　つくり領域　教授　博士(理学) ■

## 1．はじめに

電気による照明は，1879 年のエジソンの炭素電球に始まり，1996 年に白色 LED (Light Emitting Diode)が発表されて以来，われわれの生活から白熱球や蛍光灯が徐々に姿を消している．代表的な白色 LED 方式には，青色または近紫外(紫色)LED チップに蛍光体材料を組み合わせるタイプと，赤，緑，青色すべて LED チップを使用するタイプ等がある．青色LEDの開発では，日本人の研究者3名がノーベル賞を受賞したのはつい最近のことで，いかに産業界に大きな貢献をしたかを改めて実感した．白色 LED 方式のそれぞれに一長一短があり，課題解決に向け研究者が取り組んでいるが，本研究では，前者の蛍光体材料を使用するタイプへの応用を期待し，材料創成の研究を進めてきた．

白色 LED の市場規模は，今後も国内外においてますます拡大すると予想され，中でも蛍光体材料の市場を牽引しているのは，LED 照明用，液晶 TV やモニター向けバックライト，車載用の分野である．市場拡大とともに，多様な特性の蛍光体材料が要求されており，本材料の応用分野の広がりを期待している．

今回，Li-Ta-Ti-O 系固溶体を蛍光体母体とする新規赤色蛍光体材料の発光特性と，母体構造の特徴について詳しく議論する．一般に，近紫外線とは，波長が 200～380 nm 程度の電磁波の場合に定義されるが，本稿では 400 nm 付近の波長を LED 関連分野の慣例に従い，「近紫外」と記述する．

## 2．赤色蛍光体材料の合成

本稿が対象とする材料は，Li-Ta-Ti-O 系の固溶体を母体とし，これに希土類元素を賦活剤として添加した赤色蛍光体である．この母体は，ある組成域で M-相と呼ばれる特異な周期構造(super structure，超構造)が発現し(**図 1**)，Ti 添加量によりインターグロース層の挿入数を操作することで，周期構造を自在に制御できる，ユニークな自己組織的材料である[1,2]．この蛍光体は，通常の固相反応法(セラミックス法)を用いて比較的簡便に合

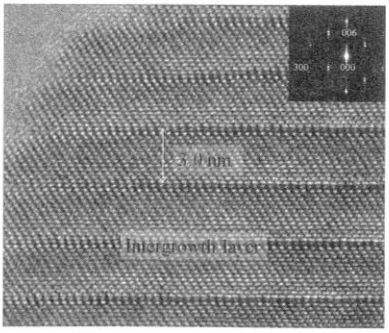


**図 1**　$Li_{1.035}Ta_{0.89}Ti_{0.41}O_3$ の周期構造

成できる．合成が容易な蛍光体は少なく，例えば，現在 LED 用蛍光体として実用化されている窒化物系化合物では高温・高圧環境が不可欠であり，シリケート系蛍光体では液相法や水系ゲル-凍結乾燥法等を用いた合成法が報告されている[3]．

本材料は $Li_2CO_3$，$Ta_2O_5$，$TiO_2$ 試薬を出発原料として用い，$Li_{1+x-y}Ta_{1-x-3y}Ti_{x+4y}O_3$ の組成式でモル比を計算し秤量する．これに賦活剤として $RE_2O_3$（$RE$：Eu，Sm，Tm，Er，Dy）を最適量添加し，ボールミルで十分に混合後プレス成型する．これを 1273 K で 3 時間加熱後，引き続き 1423 K で 15 時間電気炉で焼成し，蛍光体材料を合成する[4]．この複雑な組成式は電荷保障をするためであり，最初に M-相を見出した West[1] らのグループが提唱した式に従っている．ちなみに“M-相”の名前の由来は，最初に構造を見つけた女性研究者の名前から命名したのだと，昨年の国際会議で本人から告げられ，驚きとともに出会いに感激をした．

## 3．赤色蛍光体の発光特性と組織構造

図 2 に，$Eu^{3+}$ イオンを賦活した赤色蛍光体の励起・発光スペクトルを示す．測定には，F-7000 形分光蛍光光度計（日立）を使用した．波長 400 nm の近紫外線で励起すると，赤色領域の 625 nm 付近で，$Eu^{3+}$ イオンによるシャープな発光スペクトルが観測される．本材料は，青色（468 nm 付近）励起でも赤色発光を示すが，400 nm 励起による発光強度には及ばない．賦活剤としての Eu イオンは，$Eu^{2+}$ イオンと $Eu^{3+}$ イオンでは全く異なる発光特性を示す．その理由は，希土類イオンの電子配置の特徴にある．希土類イオンは，La（57）から Lu（71）までのイオンで，先に P 殻の 6s 軌道に電子を配置した後，Ce（58）以降は，N 殻の 4f 軌道を順に電子が配置し，それによりランタノイド収縮といわれるように，原子番号が大きくなるに従いイオン半径が小さくなる傾向を示す．4f-4f 遷移に起因する $Eu^{3+}$ イオンの発光は，外殻の O 殻電子の存在により母体構造の影響を受けにくく，シャープな赤色の線スペクトルを示す．それに対し，$Eu^{2+}$ イオンは 4f-5d 遷移のため母体構造の影響を受けやすく，ブロードな発光スペクトルを示し，配位環境に応じて色調をチューニングできるという特長がある．

本材料は，酸化物固溶体を蛍光体母体としている．固溶体を使用するメリットの一つは，結晶構造を大きく変えることなく化学組成を変化できるので，最適な発光特性を容易に見出すことができる点にある．今回，発光強度に最も大きな影響を与えたのは，母体中の Ti 添加量である．図 3 に，赤色蛍光体の Ti 添加量と発光強度の関係を示す．$Eu_2O_3$ 添加量

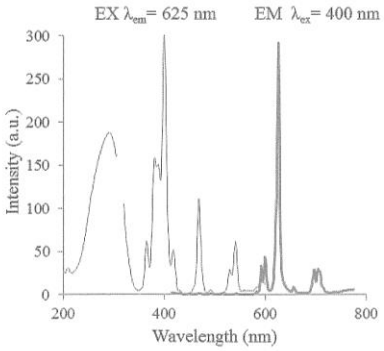

図 2　赤色蛍光体の励起・発光スペクトル

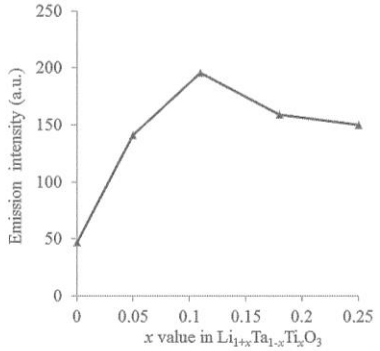

図 3　発光強度と母体中の Ti 濃度の関係

成できる．合成が容易な蛍光体は少なく，例えば，現在 LED 用蛍光体として実用化されている窒化物系化合物では高温・高圧環境が不可欠であり，シリケート系蛍光体では液相法や水系ゲル-凍結乾燥法等を用いた合成法が報告されている[3]．

本材料は $Li_2CO_3$，$Ta_2O_5$，$TiO_2$ 試薬を出発原料として用い，$Li_{1+x-y}Ta_{1-x-3y}Ti_{x+4y}O_3$ の組成式でモル比を計算し秤量する．これに賦活剤として $RE_2O_3$（$RE$：Eu，Sm，Tm，Er，Dy）を最適量添加し，ボールミルで十分に混合後プレス成型する．これを 1273 K で 3 時間加熱後，引き続き 1423 K で 15 時間電気炉で焼成し，蛍光体材料を合成する[4]．この複雑な組成式は電荷保障をするためであり，最初に M-相を見出した West[1]らのグループが提唱した式に従っている．ちなみに“M-相”の名前の由来は，最初に構造を見つけた女性研究者の名前から命名したのだと，昨年の国際会議で本人から告げられ，驚きとともに出会いに感激をした．

## 3．赤色蛍光体の発光特性と組織構造

**図 2** に，$Eu^{3+}$ イオンを賦活した赤色蛍光体の励起・発光スペクトルを示す．測定には，F-7000 形分光蛍光光度計（日立）を使用した．波長 400 nm の近紫外線で励起すると，赤色領域の 625 nm 付近で，$Eu^{3+}$ イオンによるシャープな発光スペクトルが観測される．本材料は，青色（468 nm 付近）励起でも赤色発光を示すが，400 nm 励起による発光強度には及ばない．賦活剤としての Eu イオンは，$Eu^{2+}$ イオンと $Eu^{3+}$ イオンでは全く異なる発光特性を示す．その理由は，希土類イオンの電子配置の特徴にある．希土類イオンは，La（57）から Lu（71）までのイオンで，先に P 殻の 6s 軌道に電子を配置した後，Ce（58）以降は，N 殻の 4f 軌道を順に電子が配置し，それによりランタノイド収縮といわれるように，原子番号が大きくなるに従いイオン半径が小さくなる傾向を示す．4f-4f 遷移に起因する $Eu^{3+}$ イオンの発光は，外殻の O 殻電子の存在により母体構造の影響を受けにくく，シャープな赤色の線スペクトルを示す．それに対し，$Eu^{2+}$ イオンは 4f-5d 遷移のため母体構造の影響を受けやすく，ブロードな発光スペクトルを示し，配位環境に応じて色調をチューニングできるという特長がある．

本材料は，酸化物固溶体を蛍光体母体としている．固溶体を使用するメリットの一つは，結晶構造を大きく変えることなく化学組成を変化できるので，最適な発光特性を容易に見出すことができる点にある．今回，発光強度に最も大きな影響を与えたのは，母体中の Ti 添加量である．**図 3** に，赤色蛍光体の Ti 添加量と発光強度の関係を示す．$Eu_2O_3$ 添加量

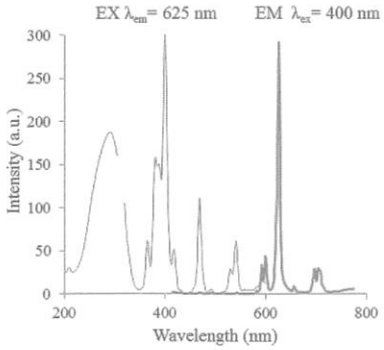


**図 2**　赤色蛍光体の励起・発光スペクトル

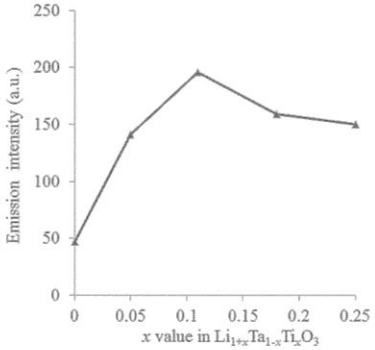


**図 3**　発光強度と母体中の Ti 濃度の関係

は，最適量の 2.5 wt%に固定した．その結果，発光強度に対する最適組成は $Li_{1.11}Ta_{0.89}Ti_{0.11}O_3$ であり，以後赤色蛍光体の母体組成とした．繰り返し赤色蛍光体を合成し，最大内部量子効率は 89%に達することを確認した(表 2)[4]．白色 LED 用蛍光体として使用するためには，温度や湿度に対する材料の安定性が求められる．本材料の温度特性を**表 1** に，高温・高湿試験(358 K/85%湿度中)結果を**表 2** に示す．その結果，温度特性および高温耐湿性が良好であるという評価が得られた．シリケート系蛍光体や一部の硫化物系蛍光体のように，耐湿性の弱点をカバーする工夫が必要となる材料もあるが，本材料は，酸化物蛍光体として高い安定性を示した．

赤色蛍光体の発光特性をさらに向上させるために，$Eu^{3+}$ イオンと $Sm^{3+}$ イオンの共添加を検討した．$Sm^{3+}$ イオンが $Eu^{3+}$ 添加蛍光体の増感剤として効果的に機能することは，エネルギー遷移メカニズムを基に解明されている[5]．**図 4** に，$Eu_2O_3$ の 2.5 wt%に対して添加した $Sm_2O_3$ 量と発光強度，内部/外部量子効率の関係を示す．その結果，$Sm_2O_3$ 量が

**表 1**　赤色蛍光体の温度特性

| Temp/K | PL 強度 | 積分強度 |
|---|---|---|
| 303 | 100 | 100 |
| 323 | 96.5 | 98.3 |
| 348 | 92.1 | 95.9 |
| 373 | 88.0 | 93.6 |
| 398 | 83.5 | 90.8 |
| 423 | 78.7 | 87.5 |

**表 2**　赤色蛍光体の高温・高湿度試験特性

| 経過時間 | 0 時間 | 500 時間 | 1000 時間 |
|---|---|---|---|
| 重量変化率(%) | 0.000 | 0.085 | 0.085 |
| 吸収率(%) | 20.3 | 21.1 | 19.1 |
| 内部量子効率(%) | 89.3 | 77.0 | 88.2 |
| 外部量子効率(%) | 18.1 | 16.2 | 16.9 |
| 色度 $x$ | 0.628 | 0.630 | 0.620 |
| 色度 $y$ | 0.310 | 0.310 | 0.307 |
| ピーク波長(nm) | 624.5 | 624.3 | 624.3 |
| 半値幅(nm) | 6.8 | 5.3 | 5.0 |

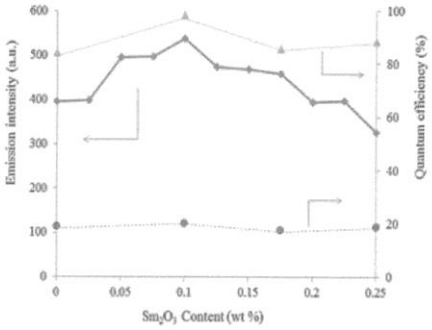


**図 4**　$Li_{1.11}Ta_{0.89}Ti_{0.11}O_3 : Eu^{3+},Sm^{3+}$ 蛍光体の $Sm_2O_3$ 添加量と発光強度および内部/外部量子効率の関係

0.1 wt%の時に最大を示し，$Eu^{3+}$ イオンのみの場合に比べ，約 1.4 倍高い発光強度を示した．内部量子効率が 90%を超える一方で，外部量子効率は 20%前後に留まっている．これは，$Eu^{3+}$ イオンの 4f-4f 遷移が禁制反射であり，吸収率が低いことに由来する．吸収率を高くするためには，応用の際にデバイス等での工夫が求められる．例えば，冷間等方圧加工法(CIP)後に焼結を行い，成型密度を上げる工夫をした結果，吸収率が改善されて外部量子効率は 40%まで向上した．**図 5** に，赤色蛍光体表面を走査型電子顕微鏡(SU-8000，日立)で撮影した二次電子像を示す．粒子サイズは，Sm 添加の有無に関わらず，1 ～ 2 μm の範囲で均質であった．焼成前の

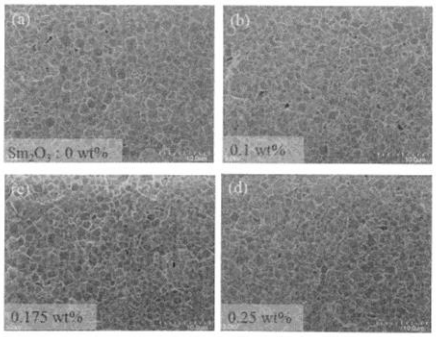


**図 5**　$Li_{1.11}Ta_{0.89}Ti_{0.11}O_3 : Eu^{3+},Sm^{3+}$ 蛍光体の粒子形状

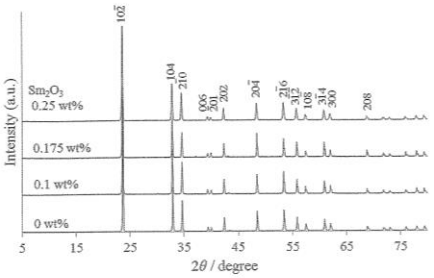


図６　$Li_{1.11}Ta_{0.89}Ti_{0.11}O_3$：$Eu^{3+}$,$Sm^{3+}$蛍光体のＸ線粉末回折図形

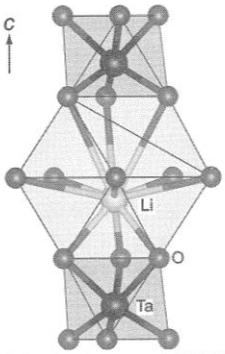


図７　[110]方向からみた$LiTaO_3$の部分構造（プログラムVESTA3[11]による描画）

混合が不十分な場合には，Sm添加試料において異常粒成長が観察され，混合プロセスが重要であることを認識した．**図６**に，$Li_{1.11}Ta_{0.89}Ti_{0.11}O_3$：$Eu^{3+}$,$Sm^{3+}$蛍光体のＸ線回折装置（XRD，RINT 2500，リガク）による構造解析結果を示す．２節で記述したとおり，Li-Ta-Ti-O系の固溶体は，ある特定の組成領域においてのみ超構造が形成される．当初は，複雑な超構造（図１）が強い赤色発光に影響していると予想した．しかし，組成を変えて合成を行い，XRDにより測定を行った結果，発光特性における最適組成では超構造は形成されず，$LiTaO_3$タイプの基本構造を維持することが分かった．図６では，$Eu^{3+}$や$Sm^{3+}$イオンを添加しても不純物相は検出されず，これらの希土類イオンが母体に存在していることを示した．

では，なぜこのように90％を超える高い内部量子効率を発現する蛍光体材料が作製できたのか？次節では，さらに詳しく母体構造の特徴について解説する．

## ４．母体構造の特徴

$LiTaO_3$の結晶構造（空間群 *R3c*）の詳細は，Hsuら[6]によって報告され，**図７**にそのモデル図を示す．Li席とTa席は共に三回回転軸上に存在し，$Li^+$イオンは12配位であり，$Ta^{5+}$イオンは６配位である．すなわち，この結晶構造は，面共有した$[LiO_{12}]$多面体と$[TaO_6]$八面体により構成される．Li-Ta-Ti-O系固溶体の場合は，$LiTaO_3$のTa席を$Ti^{4+}$イオンが置換することで，$Li(Ta,Ti)O_3$：$Eu^{3+}$蛍光体の母体構造がわずかに変化し，その変化が発光特性に強く影響すると考えられる．この仮説を確認するためには，母体構造の変化を定量的に検出することが必要である．そのために，配位多面体計算プログラムIVTON[7]を用いて各多面体のパラメータを算出し，$Ti^{4+}$イオンの固溶による多面体の変形度合いを定量的に議論した．注目すべきパラメータは，「偏心距離（Δ）」と「球形度（*S*）」である[8]．前者は，「多面体の重心と陽イオン間の距離」として定義され，Δ＝0であれば多面体の重心に陽イオンが存在することになる．後者は，多面体の重心から配位子までの平均距離（$r_s$）とその標準偏差（σ）を用いて$S=1-\sigma/r_s$で定義される値であり，「多面体のいびつさ」を表す指標になる．

構造比較のため，Ti置換量の異なる３種類の蛍光体（A）$LiTaO_3$：$Eu^{3+}$と（B）$Li(Ta_{0.89}Ti_{0.11})O_{2.945}$：$Eu^{3+}$，（C）$Li(Ta_{0.75}Ti_{0.25})O_{2.875}$：$Eu^{3+}$を作製した．この中で，（B）が最も高い発光強度を示した蛍光体である．これらのＸＲＤパターンを収集し，プログラムRIETAN-FP[9]を用いて結晶構造をリートベルト法[10]で精密化した．求めた格子定数と構成原子の分率座標の値から，$[(Li,Eu)O_{12}]$と

[(Ta,Ti)$O_6$] の多面体パラメータを計算した．[(Ta,Ti)$O_6$] 八面体では，Δ の値は 0.010 nm≦Δ≦0.012 nm の偏心距離が短い範囲に存在し，従って Ta 席原子は 3 試料いずれの場合にも多面体の重心付近に存在し，試料間で差がないことが示された．さらに $S$ の値は全て 1 に等しいことから，[(Ta,Ti)$O_6$] 八面体は $Ti^{4+}$ イオンの置換に対しても，球形度はほとんど影響されないことが分かった．一方，[(Li,Eu)$O_{12}$] 多面体では，$S$ の値は 0.821≦$S$≦0.830 の範囲内にあることから，多面体の外形はほぼ同一である．顕著に差が出たのは [(Li,Eu)$O_{12}$] 多面体の偏心距離であり，蛍光体(B)では Δ(B) = 0.047 の値を示し，他の蛍光体の Δ(A) = 0.017 や Δ(C) = 0.004 と比較して大きな値を示した．XRD 測定結果は平均構造であり，$Eu^{3+}$ イオンの局所的配位環境ではより大きな偏心が予想される[12]．蛍光体(B)の発光強度は，蛍光体(A)の 2 倍以上に相当し，発光強度の増大は，$Eu^{3+}$ イオン位置の多面体重心からの偏心と密接に関係していることが示唆される．

## 5．さいごに

本稿では，紙面の制約上触れていないが，同じ母体材料を使い，賦活剤としての希土類種を変えることにより，発光色の異なる黄色，緑色，青色蛍光体の合成にも成功している．ただ，赤色蛍光体の内部量子効率には到底及ばないため，現在も最適な合成条件を模索中である．本材料の母体構造の解析結果は，蛍光体母体の結晶構造と発光特性が密接に関連することを明示しており，新規蛍光体材料設計に活用したい．今後の市場拡大による多様な蛍光体材料の特性が要求される中で，これまでにない蛍光体材料の用途開拓が進むことを期待する．

**謝　辞**

材料の発光特性評価は，電気化学工業㈱の山田鈴弥博士に，合成は豊橋技術科学大学の古谷彰平氏に協力を頂いた．本研究の一部は，科学研究費助成事業(基盤c) No.25420709 により遂行した．ここに記して謝意を表す．

**参考文献**

1） M. E. Villafuerte-Castrejon, A. Aragon-Pina, R. Valenzuela, A. R. West, "Phase Equilibria in the systems $Li_2TiO_3$-$LiNbO_3$, $Li_2TiO_3$-$LiTaO_3$ and $Li_2TiO_3$-$LiNbO_3$-$LiTaO_3$", *J. Solid State Ceram.*, **71**, 103-108 (1987).

2） H. Nakano, S. Suehiro, S. Furuya, K. Fukuda, "Microstructural comparison between Nb- and Ta- systems in $Li_{1+x-y}M_{1-x-3y}Ti_{x+4y}O_3$ ($M = Nb^{5+}$, $Ta^{5+}$) solid solution with superstructure", *J. Alloys and Compds.*, **618**, 504 - 507 (2015).

3） S. Tezuka, Y. Sato, T. Komukai, Y. Takatsuka, H. Kato, M. Kakihana, "$Eu^{2+}$-Activated $CaSrSiO_4$: a New Red-Emitting Oxide Phosphor for White-Light-Emitting Diodes", *Appl. Phys. Express*, **6**, 072101 (2013).

4） H. Nakano, S. Suehiro, S. Furuya, H. Hayashi, S. Fujihara, "Synthesis of new $RE^{3+}$ doped $Li_{1+x}Ta_{1-x}Ti_xO_3$ (RE: Eu, Sm, Er, Tm, and Dy) phosphors with Various Emission Colors", *Materials*, **6**, 2768-2776 (2013).

5） H. Nakano, S. Furuya, K. Fukuda, S. Yamada, "Synthesis and luminescent of $Eu^{3+}$, $Sm^{3+}$ co-doped $Li_{1.11}Ta_{0.89}Ti_{0.11}O_3$ phosphor", *Mate. Res. Bull.*, **60**, 766-770 (2014).

6） R. Hsu, E. N. Maslen, D. Du Boulay, N. Ishizawa "Synchrotron X-ray studies of $LiNbO_3$ and $LiTaO_3$", *Acta Crystallogr. Sect. B: Struct. Sci.*, **53**, 420-428 (1997).

7） T. Balic-Zunic, I. Vickovic, "IVTON-a program for the calculation of geometrical aspects of crystal structures and some crystal chemical applications", *J. Appl. Crystallogr.*, **29**, 305-306 (1996).

8） E. Makovickv, T. Balic-Zunic, "New measure of distortion for coordination polyhedra", *Acta Crystallogr. Sect. B: Struct. Sci.*, **B54**, 766-773 (1998).

9） F. Izumi, K. Momma, "Three-dimensional visualization in powder diffraction", *Solid State Phenom.*, **130**, 15-20 (2007).

10） H. M. Rietveld, "Line profiles of neutron powder-diffraction peaks for structure refinement", *Acta Crystallogr.*, **22**, 151-152 (1967).

11） K. Momma, F. Izumi, "VESTA 3 for three-dimensional visualization of crystal, volumetric and morphology data", *Appl. Crystallogr.*, **44**, 1272-1276 (2011).

12） T. Uchida, S. Suehiro, T. Asaka, H. Nakano, K. Fukuda, "Syntheses and crystal structures of $Li(Ta_{0.89}Ti_{0.11})O_{2.945}$ and $(Li_{0.977}Eu_{0.023})(Ta_{0.89}Ti_{0.11})O_{2.968}$", *Powder Diffr.*, **28**, 178-183 (2013).

論　　文
Original Paper

*J. Soc. Powder Technol, Japan,* **51,** 136-141(2014)

# 構造制御されたLi-M-Ti-O系（M: Ta, Nb）固溶体の合成と構造解析

## Synthesis and Structural Analysis of $Li_{1+x-y}M_{1-x-3y}Ti_{x+4y}O_3$ (M: Ta, Nb) Solid Solutions with Superstructure

末廣 志穂[a]，中野 裕美[a, b*]

Shiho Suehiro, Hiromi Nakano

Received 25 July 2013; Accepted 15 October 2013

In the ternary $Li_2O$-$M_2O_5$-$TiO_2$ (M = Ta, Nb) system, a superstructure is formed in the chemical formula of $Li_{1+x-y}M_{1-x-3y}Ti_{x+4y}O_3$ ($0.06 \leq x \leq 0.33$, $0 \leq y \leq 0.175$), which is the so-called M-phase. In the Ta-system, the superstructure was found to form with higher Ti content ($0.06 \leq x \leq 0.2$, $0.05 \leq y \leq 0.175$). In this paper, we focus on the difference between Ta and Nb ions in the formation of a superstructure in the quaternary system $Li_{1+x}(Ta_{1-z}Nb_z)_{1-x}Ti_xO_3$ ($0.11 \leq x \leq 0.33$, $0 \leq z \leq 1.0$). The structural change is observed through the grain morphology, X-ray diffraction pattern, and transmission electron microscope image. The results show that the period of the intergrowth layer in the superstructure could be controlled with the Ti content and Ta/Nb ratio.

***Keywords***: Superstructure, Synthesis, Solid solution, TEM, XRD

### 1．緒　　言

Li-M-Ti-O系（M: Ta, Nb）固溶体は，固相反応によって，ある組成域でユニークな周期構造（超構造）を発現し，超構造を形成する領域の相はM相と呼ばれている。Castrejonらにより M相が見いだされて以来[1,2]，超構造の合成や構造解析に関する研究が報告されてきた[3~6]。また，M相周期構造と誘電特性との関係[7,8]についても報告されているが，構造と誘電特性の関係については不明瞭な点が残されている。

超構造は，三方晶の$LiNbO_3$タイプ構造が母相となり，この母相を分けるように，コランダムタイプの$[Ti_2O_3]^{2+}$相がインターグロース層として周期的に挿入して形成される。均質な超構造を有する試料を合成するには，電気炉で1373～1423 Kにおいて，最低でも24時間～72時間程度の焼成時間が必要になる[4]。Nb系固溶体では，M相の組成域でも，Ti添加量の多い組成では，余剰の$TiO_2$が第2相として検出され，固溶量には限界があることが報告されている[9]。しかしながら，Ta系固溶体については，詳細な超構造形成の組成域についてのデータや透過型電子顕微鏡を用いた詳細な構造に関する報告は少ない。また，四元系（Li-(Ta, Nb)-Ti-O系）に関する研究報告は皆無である。

著者らは，この構造制御された粉体を，低温・短時間合成するために，24 GHzのマイクロ波照射による

a 豊橋技術科学大学大学院 工学研究科 環境・生命工学系
（〒441-8580 愛知県豊橋市天伯町雲雀ヶ丘1-1）
Department of Environmental and Life Science, Toyohashi University of Technology
(1-1 Hibarigaoka, Tempaku, Toyohashi, Aichi, 441-8580, Japan)
b 豊橋技術科学大学 研究基盤センター
（〒441-8580 愛知県豊橋市天伯町雲雀ヶ丘1-1）
Cooperative Research Facility Center, Toyohashi University of Technology
(1-1 Hibarigaoka, Tempaku, Toyohashi, Aichi, 441-8580, Japan)
* 責任著者連絡先　hiromi@crfc.tut.ac.jp

グリーンプロセッシングを試みた[9]。その結果，24 GHzのマイクロ波照射により，Nb系固溶体での低温・短時間合成に成功し，1273 Kで1時間で均質な超構造を有する固溶体を合成した。近年では，新材料創出のため，この固溶体が有する超構造を蛍光体の母体材料として活用するための研究に取り組んできた。Nb系固溶体を母材として，種々の賦活剤を添加することにより，近紫外励起により赤，緑，青，黄色に発色する新規蛍光体を作製した[10, 11]。さらに，赤色蛍光体については，$Nb^{5+}$ イオンを $Ta^{5+}$ イオンに置き換えることで，発光強度が大きく向上し，高い内部量子効率を示す蛍光体の作製に成功した[12, 13]。しかしながら，発光強度と超構造の関係を明確にするにあたり，Nb系とTa系の超構造形成領域が同じであるのか，四元系でも超構造の周期は均質に形成されるのか，などの課題が生じた。

そこで，今回Ta系について，三元系から四元系での超構造形成領域を明確にするため，走査型電子顕微鏡，X線回折，透過型電子顕微鏡を用いて，詳細な構造解析を行った。特に，本稿では，四元系 $Li_{1+x}(Ta_{1-z}Nb_z)_{1-x}TixO_3$（以後LTNTと略す）（$0.11 \leq x \leq 0.33$, $0 \leq z \leq 1.0$）において，超構造の形成における $Ta^{5+}$ イオンおよび $Nb^{5+}$ イオンの違いに着目し，超構造の周期とTi添加量およびTa/Nb比の関係について詳細を報告する。

## 2．実験方法

LTNT固溶体合成のため，出発物質として，$Li_2CO_3$（99.0%，和光純薬），$Nb_2O_5$（99.9%，和光純薬），$Ta_2O_5$（99.9%，和光純薬），$TiO_2$（99.0%，和光純薬）を用いた。LTNT固溶体は，$Li_{1+x}(Ta_{1-z}Nb_z)_{1-x}Ti_xO_3$（$0.11 \leq x \leq 0.33$, $0 \leq z \leq 1.0$）の組成範囲で，**Fig. 1** の四元系状態図に示すように，$TiO_2$ の添加量を10～25 mol%まで変化させて合成した。出発物質の粉末を秤量し十分に混合した後，ペレット状（13 mm$\phi$）に加圧成型（プレス圧255 MPa）した。このペレットを，炭酸ガスを除去して固相反応を促進させるため，電気炉で1173 Kで5時間仮焼後，1393 K～1423 Kさらに24時間焼成を行った（Ta添加量が少ない試料では低温を使用）。得られた試料は，取り出して粉末X線回折（XRD）測定により相を確認しながら，不純物ピークがなくなるまで，1373 Kで繰り返し24時間～72時間程度再焼成を行った。組成により，均質になるまでの熱処理時間は異なった。

構造解析は，XRD（RINT2500，株式会社リガク）

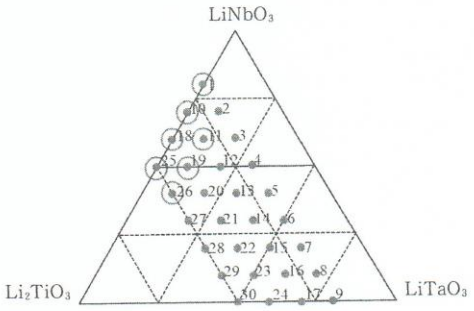


**Fig. 1** Compositions of $Li_{1+x}(Ta_{1-z}Nb_z)_{1-x}Ti_xO_3$ ($0.11 \leq x \leq 0.33$, $0 \leq z \leq 1.0$)

を用いて40 kV，200 mAでXRD測定を行った。試料の組織は，走査型電子顕微鏡（SEM）（SU-8000，日立株式会社）により，加速電圧3 kVでコーティングなしで観察した。高分解能像および制限視野電子回折（SAED）図は，透過型電子顕微鏡（TEM）（JEM-2100F，日本電子株式会社）を用いて200 kVで観察した。

## 3．結果と考察

**Fig. 2** に，三元系 $Li_{1+x-y}M_{1-x-3y}Ti_{x+4y}O_3$（M＝Nb, Ta）固溶体の超構造形成領域と，代表的な2組成でのXRDパターンを示す。Nb系では実線で囲んだ全領域で超構造が出現する[9]。一方，Ta系ではFig. 2のXRDパターンの結果が示すように，斜線部の領域（$0.06 \leq x \leq 0.2$, $0.04 \leq y \leq 0.175$）で超構造が形成された。Nb系では，Ti添加量の多い組成で固溶できない余剰の $TiO_2$ が検出され[9]，このことからもTa系のほうがNb系に比べてTi固溶量が大きいことを示した。

次に，四元系 $Li_{1+x}(Ta_{1-z}Nb_z)_{1-x}Ti_xO_3$（LTNT）の超構造形成における，$Ta^{5+}$ イオンおよび $Nb^{5+}$ イオンの違いに着目し，超構造の形成領域を調査した。組織・構造解析の結果，超構造形成領域は，Fig. 1の○印を付けた組成で形成することが確認できた。**Fig. 3** に，Ti添加量が同量でTa/Nb比率を変化させたFig. 1のNo. 10～17のラインで得られた試料のSEM像を示す。Nb系固溶体の場合，試料が超構造を形成すると，粒子形状は球状粒子から板状粒子に形状変化した[9]。今回の結果でも，Ta/Nb比率が大きくなると球状化し，板状粒子は，No. 10およびNo. 11の組成で観察された。超構造を形成した場合，XRDパターンにおいては，(012)，(202)，(122)ピークの周りに特徴的なサテライト反射が観察される[3]。Fig. 1の組成の中で，

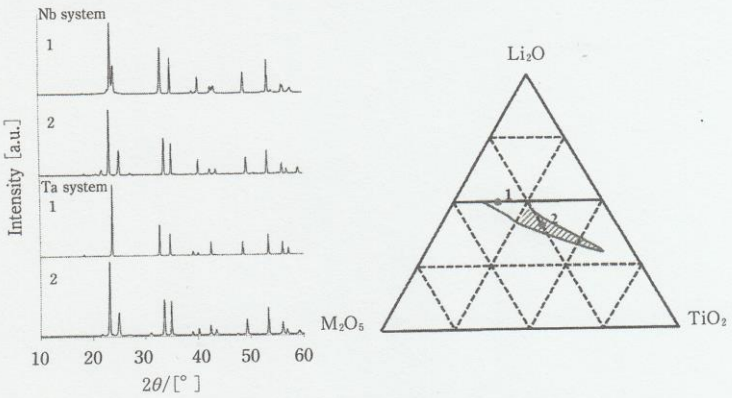


**Fig. 2** XRD patterns of the compositions marked by circle in Li-M-Ti-O system (M : Nb, Ta)

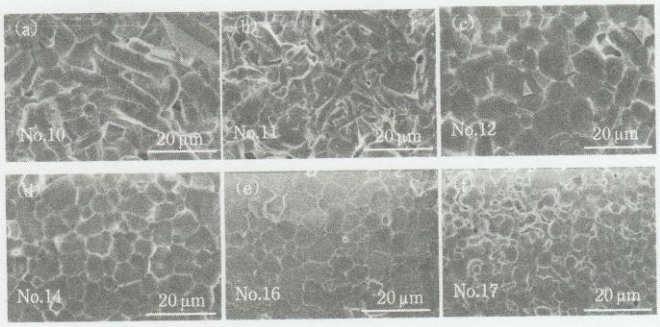


**Fig. 3** SEM images of $Li_{1.18}(Ta_{1-z}Nb_z)_{0.82}Ti_{0.18}O_3$ ($0 \leq z \leq 1.0$)
(a) $z=1.0$ (b) $z=0.857$ (c) $z=0.714$
(d) $z=0.429$ (e) $z=0.143$ (f) $z=0$

超構造を形成した組成のXRDパターンを**Fig. 4**に示す。試料番号は，Fig. 1に対応している。$LiTaO_3$の基本構造（三方晶）を比較のために示した。18度付近で検出されるピークは$Li_2TiO_3$あるいは，NbやTiを含む固溶体で，Ti添加量が多くなると形成されやすい傾向がある[8]。XRDの結果から，四元系の場合には，超構造はTi添加量が多く，Taの添加量が少ない組成域で形成されることが分かった。**Fig. 5**は，超構造を形成した組成の(012)反射周りのサテライトピークを示す。Ti添加量$x$が0.18～0.33（$z=1.0$, Ta添加量なし）の場合，Ti添加量を増加すると，サテライト間隔の$2\theta$が1.41°から1.99°に変化しており，明らかにサテライト反射の間隔が広くなっている。このことから，サテライト反射の間隔，いい換えると，超構造の周期間隔は，Ti添加量およびTa/Nbの比によって制御されていることが分かる。Ti添加量が同量では，サテライト反射の間隔は，$Ta^{5+}$イオンを添加することにより明らかに狭くなっている。これは，$LiTaO_3$の場合には，超構造を形成せずにTiを固溶できる組成範囲がNb系に比べて広いため（Fig. 2），同量の$Ti^{4+}$イオンを添加しても，$Ta^{5+}$イオンが増加すると，$[Ti_2O_3]^{2+}$のインターグロース層の間隔が拡大したものと思われる。近年，著者らは，XRDデータを用いて，リートベルト法による精密構造解析により，$LiTaO_3$と超構造を形成しない組成$Li_{1.11}Ta_{0.89}Ti_{0.11}O_3$の構造比較を行った[14]。リートベルト解析に際し，$Ti^{4+}$イオンがTaサイトに置換されている構造モデルが最適と判断し，組成を$Li(Ta_{0.89}Ti_{0.11})O_{2.945}$と決定した。$LiTaO_3$に$Ti^{4+}$イオンを固溶することにより，$LiTaO_3$構造（$R3c$）の$[LiO_{12}]$多面体の<Li-O>距離は，

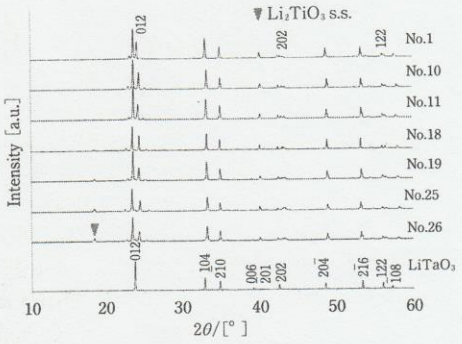


**Fig. 4** XRD patterns of $Li_{1+x}(Ta_{1-z}Nb_z)_{1-x}Ti_xO_3$ ($0.11 \leq x \leq 0.33$, $0 \leq z \leq 1.0$)
Number is corresponding to the composition in Fig. 1.

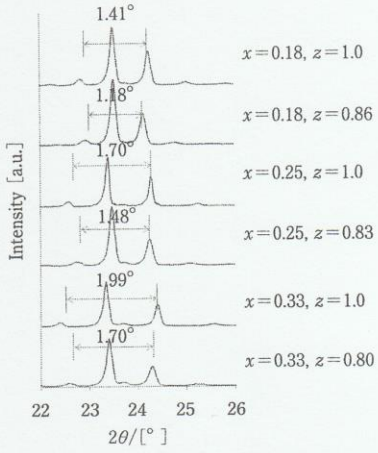


**Fig. 5** Satellite peaks of superstructutes with various compositions of $Li_{1+x}(Ta_{1-z}Nb_z)_{1-x}Ti_xO_3$

0.274 nm から 0.270 nm へ変化したが，[(Ta,Ti)$O_6$] 八面体については顕著な差はなかった。結果として，Li サイトの配位環境を変え，超構造を形成せずに基本の $LiTaO_3$ 構造を保持していることが明らかになった[14]。

LTNT の超構造の周期間隔および均質性について，TEM により観察した。**Fig. 6** に，$Li_{1.18}Nb_{0.82}Ti_{0.18}O_3$ および $Li_{1.18}(Ta_{0.14}Nb_{0.86})_{0.82}Ti_{0.18}O_3$ の [100] 方位からの TEM 像と制限視野電子回折（SAED）図を示す。SAED 図で，基本反射間にサテライト反射が c- 軸方向に観察される。これは，インターグロース層が規則的に挿入されたことにより出現したものであり，不均質な場合には，ストリークスとなって現れる。Fig. 6 (a) のインターグロース層の間隔 6.2 nm＝(006)×27 で，この周期に相当するサテライト反射が約27倍周期として規則的に SAED 図に出現している。Fig. 6 (c) では，(a) に比べてインターグロース層の間隔が広がり，したがってサテライト反射は35倍周期で出現している。この結果から，Ta と Nb が混在する四元系においても，超構造の周期は均質に形成されることが分かった。また，$Li_{1.18}(Ta, Nb)_{0.82}Ti_{0.18}O_3$ に 0.14 at% の $Ta^{5+}$ イオンを固溶することにより，インターグロース層の周期間隔は，$Li_{1.18}Nb_{0.82}Ti_{0.18}O_3$ の周期よりも 1.7 nm 広くなり，この結果もまた，Ta 系のほうが Nb 系に比べて Ti 固溶量が大きいことに起因し，XRD 解析の結果と一致している。

均質な超構造の形成には，電気炉で長時間の焼成を要した。焼成時間については，Ti の添加量が少ない試料では，インターグロース層の周期が均質化するまでの時間が長くなる傾向を示した。このため，XRD で構造を確認しながら，繰り返し焼成を行い，超構造形成過程を調査した。$Li_{1.18}(Ta_{0.14}Nb_{0.86})_{0.82}Ti_{0.18}O_3$ について，焼成時間による構造変化を **Fig. 7** に示す。24 時間の焼成では，23度と33度付近に $LiNbO_3$ の基本構造の (012) と (104) ピークが検出され，$LiNbO_3$ 基本構造と超構造の 2 相が共存していることが分かる。さらに長時間の熱処理をすると，一部の球状粒子はすべて

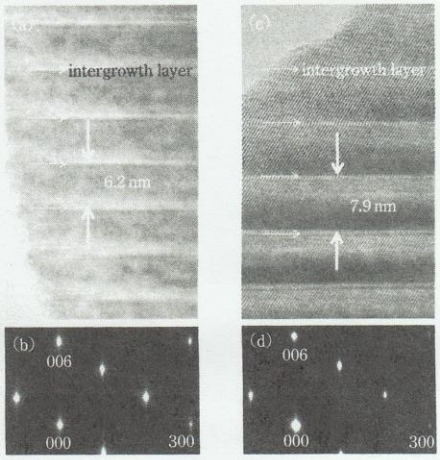


**Fig. 6** TEM images and SAED patterns of (a, b) $Li_{1.18}Nb_{0.82}Ti_{0.18}O_3$ and (c, d) $Li_{1.18}(Ta_{0.14}Nb_{0.86})_{0.82}Ti_{0.18}O_3$

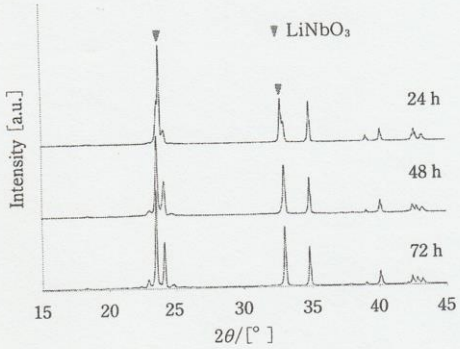


**Fig. 7** XRD patterns of $Li_{1.18}(Ta_{0.14}Nb_{0.86})_{0.82}Ti_{0.18}O_3$ with various sintering time

板状粒子に変化した。72時間後には，TEM 像（Fig. 6 (c)）に示すように，周期間隔は 7.9 nm と均質に形成され，サテライト反射は(012)ピークの周りに明瞭に出現した。超構造形成の理由として，価数の異なる $Ti^{4+}$ イオンの固溶により生じた静電的な斥力を緩和するために，一定の周期でインターグロース層を形成すると west らは推察している[3]。超構造の形成過程を詳しく知るために，Fig. 7 の24時間焼成で得られた試料について，TEM 像を観察し，①～④の箇所で点分析を行った結果を **Fig. 8** に示す。TEM 像から，24時間焼成ではインターグロース層が不均質に形成されていることが観察される。点分析の結果から，Ti 量はインターグロース層の形成箇所付近で多く分布しているのに対し，Nb/Ta 比は試料全体で同等であり，均質に分布していることがわかった。この結果から，超構造形成には，$Ti^{4+}$ イオンの拡散が律速となり，斥力を緩和するための $[Ti_2O_3]^{2+}$ のインターグロース層の形成は，粒成長とともに徐々に進行することが考えられる[9]。

## 4．結　論

今回，$Li_2O$-$Ta_2O_5$-$TiO_2$ 固溶体の超構造形成領域について，特に，四元系 $Li_{1+x}(Ta_{1-z}Nb_z)_{1-x}Ti_xO_3$ ($0.11 \leq x \leq 0.33$, $0 \leq z \leq 1.0$) について，超構造の形成における $Ta^{5+}$ イオンおよび $Nb^{5+}$ イオンの違いに着目した。

その結果，四元系においても，均質な超構造が形成され，Ti 添加量および Ta/Nb 比により，周期間隔が

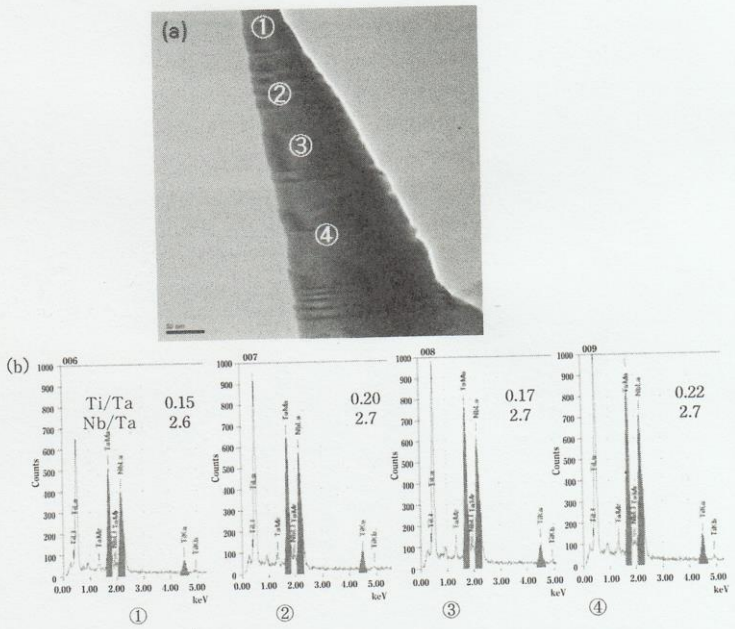


**Fig. 8** TEM image of inhomogeneous specimen and spot analysis by EDS
(a) TEM image of $Li_{1.18}(Ta_{0.14}Nb_{0.86})_{0.82}Ti_{0.18}O_3$ sintered for 24 h
(b) EDS spectra at points marked by number in (a)

制御できることが分かった。Ti添加量が同量の場合には，$Ta^{5+}$ イオンを添加するほうが，インターグロース層の間隔が広くなり，Ta添加量が多くなると，超構造を形成しなく領域も存在した。この理由は，Ta系のほうがNb系に比べて，Ti固溶量が大きく，Ta系の場合には，Liサイトの配位環境を変えることにより，超構造を形成せずに $LiTaO_3$ の基本構造を維持することができることに起因すると結論づけた。

［謝辞］ 本研究の一部は，科学研究費（基盤（c)No. 25420709）により遂行したので記して謝意を表す。

## References


1）Villafuerte-Castrejon, M. E., J. A. Gracia, E. Cisneros, R. Valenzuela and A. R. West : "New rutile solid solutions $Ti_{1-4x}Li_xM_{3x}O_2$ : M＝Nb, Ta, Sb", *J. Brit. Ceram. Soc.*, **83**, 143-145 (1984)

2）Villafuerte-Castrejon, M. E., A. Aragon-Pina, R. Valenzuela and A. R. West : "Compound and solid-solution formation in the system $Li_2O$-$Nb_2O_5$-$TiO_2$", *J. Solid State Ceram.*, **71**, 103 -108 (1987)

3）Smith, R. I. and A. R. West : "Characterization of an incommensurate LiTiNb oxide", *Mat. Res. Bull.*, **27**, 277-285 (1992)

4）Hayashi, H., H. Nakano, K. Suzumura, K. Urabe and A. R. West : "Superstructure in LiTiNb Oxides", *Forth Ceram. Soc.*, **2**, 391-398 (1995)

5）Hayashi, H., K. Urabe and K. Niihara : "Preparation of stoichiometric crystalline $Li(Nb,Ti)O_3$ solid solutions by sol-gel processing with metal alkoxides", *Key Engineering materials.*, **501**, 161-163 (1999)

6）Farber, L., I. Levin, A. Borisevichi, I. E. Grey, R. S. Roth and P. K. Davies : "Structural Study of $Li_{1+x-y}Nb_{1-x-3y}Ti_{x+4y}O_3$ Solid Solutions", *J. Solid State Chem.*, **166**, 81-90 (2002)

7）Borisevich, A. Y. and P. K. Davies : "Crystalline structure and dielectric properties of $Li_{1+x-y}Nb_{1-x-3y}Ti_{x+4y}O_3$ M-phase solid solutions", *J. Am. Ceram. Soc.*, **85**, 573-578 (2002)

8）Yamamoto, Y., H. Hayashi, T. Sekino, T. Nakayama, T. Kondo, M. Wada, T. Adachi and K. Niihara : "Microstructure and dielectric properties of sintered Li-Nb-Ti-O solid solution ceramics having superstructure", *Materials Research Innovations*, **7**, 74-79 (2003)

9）Nakano, H., T. Saji, M. Yuasa, M. Shoji and M. Mamoru : "Rapid synthesis and structural analysis of Li-Nb-Ti-O solid solutions with superstructure by millimeter-wave heating", *J. Ceram. Soc. Japan*, **119**, 808-812 (2011)

10）Hayashi, H. and H. Nakano : "Evaluation and preparation of $Li_{1+x-y}Nb_{1-x-3y}Ti_{x+4y}O_3$ solid solution with superstructure as new phosphor", *J. Alloys and Compds.*, **502**, 360-364 (2010)

11）Nakano, H., S. Suehiro, T. Saji and S. Miyake : "Synthesis of a rare-earth doped LNT (Li-Nb-Ti-O) phosphor by millimeter-wave heating", *J. Alloys and Compds.*, **552**, 475-479 (2013)

12）Nakano, H., K. Ozono, H. Hayashi and S. Fujihara : "Synthesis and luminescent properties of a new $Eu^{3+}$-doped $Li_{1+x}(Ta_{1-z}Nb_z)_{1-x}Ti_xO_3$ red phosphor", *J. Ame. Ceram. Soc.*, **95**(**9**), 2795-2797 (2012)

13）Nakano, H., S. Suehiro, H. Hayashi and S. Fujihara : "Synthesis of new $RE^{3+}$ doped $Li_{1+x}Ta_{1-x}Ti_xO_3$ (RE : Eu, Sm, Er, Tm, and Dy) phosphors with various emission colors", *Materials*, **6**, 2768-2776 (2013)

14）Uchida, T., S. Suehiro, T. Asaka, H. Nakano and K. Fukuda : "Syntheses and crystal structures of $Li(Ta_{0.89}Ti_{0.11})O_{2.945}$ and $(Li_{0.977}Eu_{0.023})(Ta_{0.89}\ Ti_{0.11})O_{2.968}$", *Powder Diff. J.*, **28**(**3**), 178-183 (2013)

Journal of Alloys and Compounds 618 (2015) 504–507

Contents lists available at ScienceDirect

Journal of Alloys and Compounds

journal homepage: www.elsevier.com/locate/jalcom

# Microstructural comparison between Nb- and Ta-systems in $Li_{1+x-y}M_{1-x-3y}Ti_{x+4y}O_3$ (M = $Nb^{5+}$, $Ta^{5+}$) solid solution with superstructure

Hiromi Nakano [a,b,*], Shiho Suehiro [b], Syohei Furuya [b], Koichiro Fukuda [c]

[a] Cooperative Research Facility Center, Toyohashi University of Technology, Toyohashi 441-8580, Japan
[b] Department of Environmental and Life Sciences, Toyohashi University of Technology, Toyohashi 441-8580, Japan
[c] Department of Materials Science and Engineering, Nagoya Institute of Technology, Nagoya 466-8555, Japan

ARTICLE INFO

*Article history:*
Received 25 June 2014
Received in revised form 19 August 2014
Accepted 19 August 2014
Available online 27 August 2014

*Keywords:*
Oxide materials
Sintering
Atomic scale structure
SEM
TEM
X-ray diffraction

ABSTRACT

We successfully synthesized $Li_{1+x-y}M_{1-x-3y}Ti_{x+4y}O_3$ solid solutions (M = Nb or Ta, LMT, $0.07 \leqslant x \leqslant 0.33$, $0 \leqslant y \leqslant 0.175$) that have a superstructure, using a conventional electric furnace. The synthesizing time depended on the Ti content, and annealing was repeated for 24–264 h until a homogeneous structure was formed by the insertion of periodical intergrowth layers. We characterized the LMT solid solutions, from micro-scale to nano-scale, using X-ray diffraction, a scanning electron microscope, and a transmission electron microscope. The period of the intergrowth layer was controlled by the Ti content. LNT's period of the intergrowth layer was narrower than that of LTT in the real lattice when the Ti content was the same. The narrowest interplanar distance (1.82 nm) of the intergrowth layer was formed in $Li_{0.935}Ta_{0.365}Ti_{0.810}O_3$. The widest distance (14.3 nm) appeared in $Li_{1.11}Nb_{0.89}Ti_{0.11}O_3$, but no such wide period formed in the Ta-system.



## 1. Introduction

In the $Li_2O$–$Nb_2O_5$–$TiO_2$ system, $Li_{1+x-y}Nb_{1-x-3y}Ti_{x+4y}O_3$ ($0.05 \leqslant x \leqslant 0.3$, $0 \leqslant y \leqslant 0.182$) (LNT) forms with a superstructure known as the M-phase, which is formed by the periodical insertion of an intergrowth layer in a matrix having a trigonal structure. Since the discovery of the M-phase by Villafuerte-Castrejon et al. [1,2], related structures have been investigated [3–7]. The relationship between the M-phase's dielectric property and the period of its intergrowth layer has also been studied [8,9]. To better tailor the material's properties, the anisotropy structure of an LNT solid solution was synthesized, in which rod-precipitates were arranged regularly by a crystal growth method [10]. In a high magnetic field, oriented bulk LNT ceramic with a superstructure was prepared [11]. On the other hand, for the $Li_2O$–$Ta_2O_5$–$TiO_2$ (LTT) system, few papers have reported the relationship between the dielectric property and the composition [12], and no paper has addressed its detailed structure.

To apply this unique structure as a host material of phosphor, new phosphors have been investigated based on LNT or related structures made by a conventional electric furnace [13,14]. Recently, we successfully synthesized a red phosphor with high PL intensity using as host material an $Li_{1+x}(Ta_{1-2}Nb_2)_{1-x}Ti_xO_3$ solid solution [15]. To clarify the relationship between the structure and PL intensity, the host material's microstructure must be determined.

This time, we synthesized Nb- and Ta-bearing solid solutions with a homogeneous superstructure based on two viewpoints. One is to clarify the self-organized formation area of the superstructure. The second viewpoint is to compare the detailed microstructure between the Nb- and Ta-solid solutions. Structural analysis of the $Li_{1+x-y}M_{1-x-3y}Ti_{x+4y}O_3$ (LMT, M = Nb or Ta) solid solution was carefully performed, from micro-scale to nano-scale, using X-ray diffraction (XRD), a scanning electron microscope (SEM), and a transmission electron microscope (TEM). In this paper we report our new observations.

## 2. Experimental procedure

The starting materials used were $Li_2CO_3$, $Nb_2O_5$, $Ta_2O_5$ and $TiO_2$ (>99.9% grade) to prepare the solid solution of LNT and LTT. The compositions of the LMT solid solutions prepared in this work followed the general formula $Li_{1+x-y}M_{1-x-3y}Ti_{x+4y}O_3$ (M = Nb or Ta), with $0.07 \leqslant x \leqslant 0.33$, $0 \leqslant y \leqslant 0.175$. The mixed and pressed powders were calcined at 1273 K for 3 h and continuously at 1393 K for LNT and at 1423 K

* Corresponding author at: Cooperative Research Facility Center, Toyohashi University of Technology, Toyohashi 441-8580, Japan.
*E-mail address:* hiromi@crfc.tut.ac.jp (H. Nakano).

http://dx.doi.org/10.1016/j.jallcom.2014.08.172
0925-8388/

for LTT using an electric furnace in air. The annealing was repeated several times until the X-ray diffraction (XRD) patterns of resultant powders were free of impurity peaks.

Structural analysis was carried out by X-ray diffraction (XRD) using a RINT 2500 (Rigaku Co., Ltd., Japan) operating at 40 kV and 200 mA. The angles were corrected by an external standard method for calculation of the lattice parameters. Microstructure images were observed with a scanning electron microscope (SEM) (SU 8000, Hitachi Co., Ltd., Japan) operating at 3 kV. High-resolution TEM (HRTEM) images and selected area electron diffraction (SAED) patterns were also observed by a device (2100 F, JEOL Co., Ltd., Japan) operating at 200 kV and equipped with energy dispersive X-ray spectroscopy (EDS). The crystal-structure models, the structural parameters of which were taken from those determined in a previous study [16], were visualized with the computer program VESTA [17].

## 3. Results and discussion

First, we synthesized an LTT solid solution with a composition of $Li_{1+x-y}Ta_{1-x-3y}Ti_{x+4y}O_3$ ($0.07 \leqslant x \leqslant 0.33$, $0 \leqslant y \leqslant 0.175$) at the formation area of the M-phase in the LNT solid solution, as previously reported [1]. The synthesizing compositions are listed at 16 points in Fig. 1. We confirmed the superstructure by detecting the appearance of satellite reflections near the reflection with indices 012 in the XRD pattern. The results show that the period is controlled by the Ti content and that the composition range of the LTT's superstructure formation is narrower than that of LNT, as indicated by the dotted area in Fig. 1. These results almost completely agreed with the data reported by Borisevich and Davies [8]. We also compared the structure between the LNT and LTT solid solutions. Fig. 2 shows the structural change in two compositions with $Li_{1.18}M_{0.82}Ti_{0.18}O_3$ (No. 2 in Fig. 1) and $Li_{1.02}M_{0.62}Ti_{0.47}O_3$ (No. 11 in Fig. 1) formulas. With low Ti content, $LiTaO_3$'s basic structure appeared and no superstructure was formed (Fig. 2(b)). When the Ti content was the same for the LNT- and LTT-solid solutions, LNT's period was larger than that of LTT in the reciprocal lattice of the XRD pattern. In other words, LNT's period of the intergrowth layer was narrower than that of LTT in the real lattice.

Next, we synthesized the LTT solid solution on the composition line with a range of $x = 0.11$ and $y$ values that were finely varied from 0 to 0.175 (Fig. 3). The detailed structures were carefully analyzed by XRD, SEM, and TEM. Fig. 4 shows the XRD patterns of the LTT solid solutions. The superstructure started to form a composition when $y = 0.039$, but the $LiTaO_3$ phase remained, even for over 11 days of sintering, as indicated by the triangles. Homogeneous structure was formed from the composition of $y = 0.048$–$0.175$. The spacing of the satellite reflections at (0 1 2) became wider with increasing Ti content, as indicated by the arrows, and the limited period of the intergrowth layer was $y = 0.150$ (No. 11, $TiO_2$ content

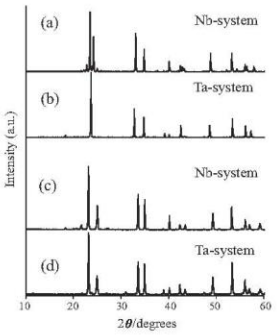


**Fig. 2.** XRD patterns of $Li_{1.18}M_{0.82}Ti_{0.18}O_3$ (No. 2 in Fig. 1) in (a)/(b) and $Li_{1.02}M_{0.62}Ti_{0.47}O_3$ (No. 11 in Fig. 1) in (c)/(d).

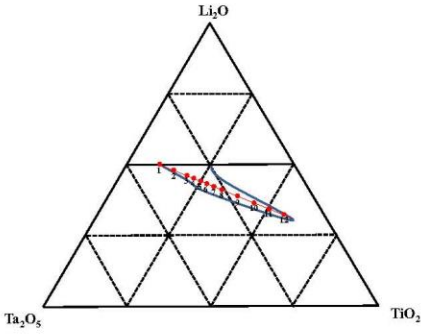


**Fig. 3.** Synthesizing compositions in $Li_{1+x-y}Ta_{1-x-3y}Ti_{x+4y}O_3$ solid solution on the line indicating $x = 0.11$ and $y$ value ranging from 0 to 0.175.

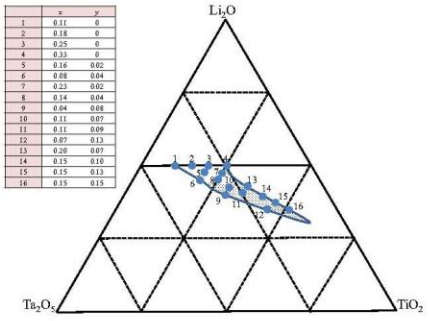


| | x | y |
|---|---|---|
| 1 | 0.11 | 0 |
| 2 | 0.18 | 0 |
| 3 | 0.25 | 0 |
| 4 | 0.33 | 0 |
| 5 | 0.16 | 0.02 |
| 6 | 0.08 | 0.04 |
| 7 | 0.23 | 0.02 |
| 8 | 0.14 | 0.04 |
| 9 | 0.04 | 0.08 |
| 10 | 0.11 | 0.07 |
| 11 | 0.11 | 0.09 |
| 12 | 0.07 | 0.13 |
| 13 | 0.20 | 0.07 |
| 14 | 0.15 | 0.10 |
| 15 | 0.15 | 0.13 |
| 16 | 0.15 | 0.15 |

**Fig. 1.** Synthesizing compositions of $Li_{1+x-y}Ta_{1-x-3y}Ti_{x+4y}O_3$ solid solution. Dotted area is superstructure formation area.

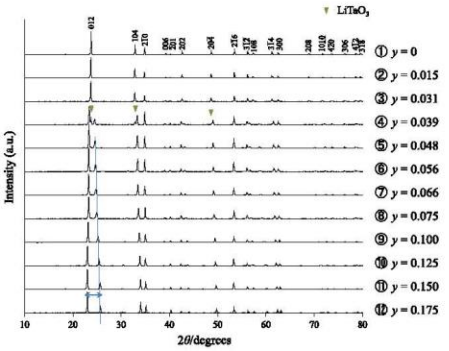


**Fig. 4.** XRD patterns of LTT solid solutions.

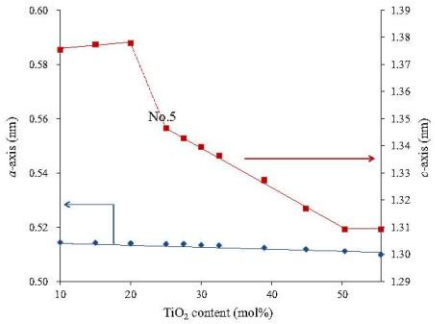


**Fig. 5.** Relationship between cell parameters and $TiO_2$ content for LTT.

of 50 mol% in Fig. 3). Fig. 5 shows the relationship between the cell parameters and the Ti content. The lattice constant of the *c*-axis obviously changed after the superstructure was formed. With increasing Ti content, the cell size of the *c*-axis gradually decreased until a limited period was formed. On the other hand, the cell size of the *a*-axis was almost the same, even with increasing Ti content. The grain shapes also clearly changed from spherical to plate-like when a superstructure was formed over the composition with $y = 0.048$ (Fig. 6). The crystal's *c*-axis was perpendicular to the basal plane of the plate-like grain.

Next, we analyzed and compared the widest and narrowest periods in the M-phase area (Fig. 1). Fig. 7 shows both TEM images and selected area diffraction patterns of the LNT and LTT solid solutions. The widest interplanar distance of the intergrowth (14.3 nm) was formed in $Li_{1.11}Nb_{0.89}Ti_{0.11}O_3$. No such wide distance formed in the Ta-system, where the widest distance (3.87 nm) appeared in $Li_{1.062}Ta_{0.746}Ti_{0.302}O_3$. On the other hand, narrow distances of the intergrowth layer were formed in $Li_{0.935}Ta_{0.365}Ti_{0.810}O_3$ and $Li_{0.935}Nb_{0.365}Ti_{0.810}O_3$: 1.82 nm and 2.17 nm, respectively. In the case of $Li_{0.935}Nb_{0.365}Ti_{0.810}O_3$, a small amount of excess Ti ions was detected in XRD as an impurity phase and actual Ti content was not the same. This was caused by the difference in the substitution capacity of the Ti ion between $LiNbO_3$ and $LiTaO_3$. In other

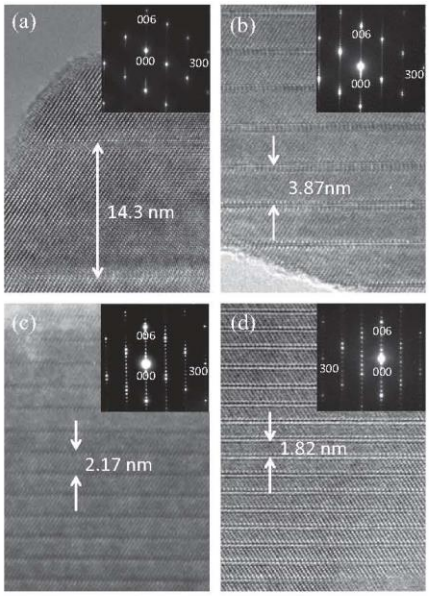


**Fig. 7.** TEM images taken from the [0 1 0] or [0 1 0] zone axis of widest periods of LNT (a) and LTT (b) in the M-phase area (shown in Fig. 1). Narrowest periods of LNT (c) and LTT (d).

words, a larger amount of Ti ion was occluded in the $LiTaO_3$ crystal than in the $LiNbO_3$ crystal. The narrowest period of 1.82 nm equaled only eight times the (0 0 6) spacing in $Li_{0.935}Ta_{0.365}Ti_{0.810}O_3$, where the structure has some strain due to the matrix and the intergrowth layers having different structures. Actually, we observed strain contrast in the TEM images. Here, the crystal structures determined by the Rietveld method were compared between

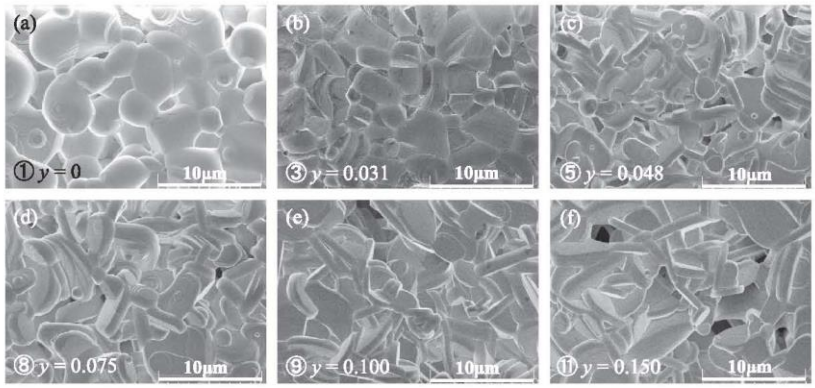


**Fig. 6.** SEM images of LTT solid solutions. Inset numbers correspond to the numbers in Fig. 3.

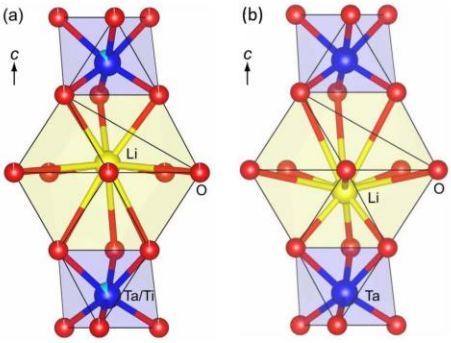


**Fig. 8.** Structures determined for $Li(Ta,Ti)O_3$ (a) and $LiTaO_3$ (b) viewed along [1 1 0], showing coordination polyhedra for Li and Ta.

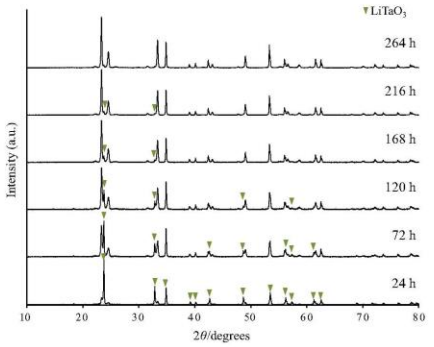


**Fig. 9.** Structural changes in $Li_{1.062}Ta_{0.746}Ti_{0.302}O_3$ (No. 5 in Fig. 3) during annealing.

$LiTaO_3$ and LTT with no superstructure. The chemical composition was determined to be $Li(Ta_{0.89}Ti_{0.11})O_{2.945}$ from the Rietveld refinement process, and detailed crystallographic data have been reported [16]. Fig. 8 shows the determined structures viewed along [1 1 0] as well as the coordination polyhedra for Li and Ta. The structure of the $LiTaO_3$ crystal was stable, and the Li ion shifted from the center of the Li site along the *c*-axis by doping of the Ti ion. As a result, the composition range of LTT's superstructure formation was narrower than that of the LNT solid solution.

The structural stability of the superstructure has been estimated by a first-principles calculation [7]. The structure was stable due to the formation of the superstructure, which was composed through an anisotropic arrangement of the Ti ions. The superstructure was formed by the diffusion and precipitation of Ti ions where extra cations in the phases were accommodated by the formation of $Li_2TiO_3$ in the middle of the $LiMO_3$ (M = Nb or Ta) slabs. Therefore, annealing needed to be repeated until a homogeneous superstructure was formed (i.e. the system reaches equilibrium), as shown in Fig. 9. With low Ti content (No. 5 in Fig. 3), a longer annealing time was needed to homogeneously insert the intergrowth layer. Consequently, the superstructure's formation speed and area were also controlled by the Ti content, the strain, and the stability of the crystal structure.

## 4. Conclusion

We clarified the formation area of the superstructure in the $Li_{1+x-y}M_{1-x-3y}Ti_{x+4y}O_3$ solid solution (M = Nb or Ta). It was formed through self-organizing by the periodical insertion of an intergrowth layer in a matrix having a trigonal structure. With increasing Ti content, the period gradually became narrower. Structural comparison between the Nb- and Ta-systems was carried out using XRD, SEM, and TEM, from micro-scale to nano-scale. As a result, the composition range of the superstructure formation and the period of the intergrowth layer were not the same. The widest interplanar distance of the intergrowth (14.3 nm) was formed in $Li_{1.11}Nb_{0.89}Ti_{0.11}O_3$, and no such wide period was formed in the Ta-system. In the area with a large amount of Ti content, the narrowest interplanar distance of 1.82 nm was formed, which was only eight times the (0 0 6) spacing found in $Li_{0.935}Ta_{0.365}Ti_{0.81}O_3$. In the Nb-system, no such narrow period was formed. This was caused by the difference in the substitution capacity of the Ti ion between $LiNbO_3$ and $LiTaO_3$. The structure of the $LiTaO_3$-type by doping of the Ti ion was stable and shifted the Li ion from the center of the Li site. Consequently, a larger amount of the Ti ion was occluded in the Ta-system than in the Nb-system in the solid solution.

## Acknowledgement

This work was partially supported by a Grant-in-Aid for Scientific Research (c) No. 25420709 (H.N.) by the Japan Society for the Promotion of Science.

## References

[1] M.E. Villafuerte-Castrejon, J.A. Gracia, E. Cisneros, R. Valenzuela, A.R. West, J. Brit. Ceram. Soc. 83 (1984) 143–145.
[2] M.E. Villafuerte-Castrejon, A. Aragon-Pina, R. Valenzuela, A.R. West, J. Solid State Chem. 71 (1987) 103–108.
[3] R.I. Smith, A.R. West, Mat. Res. Bull. 27 (1992) 277–285.
[4] H. Hayashi, H. Nakano, K. Suzumura, K. Urabe, A.R. West, Forth Euro-Ceram. Soc. 2 (1995) 391–398.
[5] H. Hayashi, K. Urabe, K. Niihara, Key Eng. Mater. 161–163 (1999) 501–504.
[6] L. Farber, I. Levin, A. Borisevichi, I.E. Grey, R.S. Roth, P.K. Davies, J. Solid State Chem. 166 (2002) 81–90.
[7] H. Nakano, T. Saji, M. Yuasa, S. Miyake, M. Mabuchi, J. Ceram. Soc. Jpn. 119 (2011) 808–812.
[8] A.Y. Borisevich, P.K. Davies, J. Am. Ceram. Soc. 85 (2002) 573–578.
[9] Y. Yamamoto, H. Hayashi, T. Sekino, T. Nakayama, T. Kondo, M. Wada, T. Adachi, K. Niihara, Mater. Res. Innovations 7 (2003) 74–79.
[10] Y. Yamamoto, T. Sekino, T. Kusunose, T. Nakayama, Y. Morimoto, S. Miyazawa, K. Niihara, J. Cry, Growth 264 (2004) 445–451.
[11] H. Nakano, S. Suehiro, T.S. Suzuki, Mater. Sci. Forum 783–786 (2014) 2480–2484.
[12] H. Nakano, K. Ozono, H. Hayashi, S. Fujihara, J. Am. Ceram. Soc. 95 (9) (2012) 2795–2797.
[13] H. Hayashi, H. Nakano, J. Alloys Comp. 502 (2010) 360–364.
[14] H. Hayashi, H. Nakano, M.I. Jones, J. Ceram. Soc. Jpn. 118 (2010) 226–230.
[15] A. Borisevich, P.K. Davies, J. Europ. Ceram. Soc. 21 (2001) 1719–1722.
[16] T. Uchida, S. Suehiro, T. Asaka, H. Nakano, K. Fukuda, Powder Diffr. 28 (3) (2013) 178–183.
[17] K. Momma, F. Izumi, J. Appl. Crystallogr. 44 (2011) 1272–1276.

TECHNICAL ARTICLE

# Crystal structures and enhancement of photoluminescence intensities by effective doping for lithium tantalate phosphors

Hiroaki Ichioka,[1] Shohei Furuya,[2] Toru Asaka,[1] Hiromi Nakano,[2] and Koichiro Fukuda[1,a)]
[1]*Department of Materials Science and Engineering, Nagoya Institute of Technology, Nagoya 466-8555, Japan*
[2]*Department of Environmental and Life Sciences, Toyohashi University of Technology, Toyohashi 441-8580, Japan*

(Received 14 April 2015; accepted 10 July 2015)

Crystal structures of $(Li_{0.925}Eu^{3+}_{0.025})TaO_3$, $(Li_{0.968}Eu^{3+}_{0.032})(Ta_{0.81}Ti_{0.19})O_{2.937}$, $(Li_{0.967}Sm^{3+}_{0.033})(Ta_{0.89}Ti_{0.11})O_{2.978}$, and $(Li_{0.950}Sm^{3+}_{0.033}Mg_{0.017})(Ta_{0.89}Ti_{0.11})O_{2.987}$ were investigated by X-ray powder diffraction. The initial structural parameters, taken from those of the isomorphous compound $(Li_{0.977}Eu^{3+}_{0.023})(Ta_{0.89}Ti_{0.11})O_{2.968}$ (space group $R3c$ and $Z = 6$), were refined by the Rietveld method. A pattern-fitting method based on the maximum-entropy method was subsequently used to determine the three-dimensional electron-density distributions (EDDs) that are free from the structural bias. We confirmed that the EDDs are in accord with the resulting structural models, each of which was composed of the [(Ta, Ti)$O_6$] octahedron and [(Li, Eu, Sm, Mg)$O_{12}$] polyhedron. We compared these polyhedra and found that the prominent difference among these compounds was the centroid-to-(Li, Eu, Sm, Mg) distance (eccentricity) of [(Li, Eu, Sm, Mg)$O_{12}$]. The high correlation was demonstrated between the magnitude of eccentricity and photoluminescence intensity under near ultraviolet excitation. © *2015 International Centre for Diffraction Data.*
[doi:10.1017/S0885715615000688]

Key words: doped lithium tantalate, X-ray powder diffraction, Rietveld method, electron-density distributions, phosphors

## I. INTRODUCTION

Recently, $Li(Ta_{1-x}Ti_x)O_{3-x/2}$ crystals ($0 \le x \le 0.25$), when they are activated with rare-earth ions ( = $Sm^{3+}$, $Eu^{3+}$, $Er^{3+}$, $Dy^{3+}$, and/or $Tm^{3+}$), have been found to demonstrate the highly efficient emission with various colors upon near ultraviolet (UV) excitation (Nakano *et al.*, 2012, 2013). Nakano *et al.* (2012) have investigated the photoluminescence (PL) properties of the $Eu^{3+}$-doped $Li(Ta_{1-x}Ti_x)O_{3-x/2}$ phosphors and found that their PL intensities have been dependent on the $x$-value. The intensity was the highest for phosphor with $x = 0.11$. The phosphors with $x$-values lower or higher than this value thus showed the inferior intensities. Uchida *et al.* (2013) used the X-ray powder diffraction (XRPD) method to determine the crystal structure of $Li(Ta_{1-x}Ti_x)O_{3-x/2}:Eu^{3+}$ phosphor with $x = 0.11$ (space group $R3c$), the chemical formula of which is $(Li_{0.977}Eu^{3+}_{0.023})(Ta_{0.89}Ti_{0.11})O_{2.968}$. They found that it is isostructural with $LiTaO_3$ (Hsu, *et al.*, 1997), in which both (Li, Eu) and (Ta, Ti) sites are located on the triad axis (Figure 1). The (Li, Eu) atom is 12-fold coordinated by oxygen and (Ta, Ti) site is coordinated with six oxygen atoms. The (Li, Eu) site is relatively largely displaced from the centroid of [(Li, Eu)$O_{12}$] polyhedra in the [00$\bar{1}$] direction by 0.047 nm, in contrast to the (Ta, Ti) site located nearly at the centroid of the [(Ta, Ti)$O_6$] octahedra (Uchida *et al.*, 2013). To clarify the mechanism of high efficiency and further improve the PL performance of doped lithium tantalate phosphors, it is necessary to obtain the structural

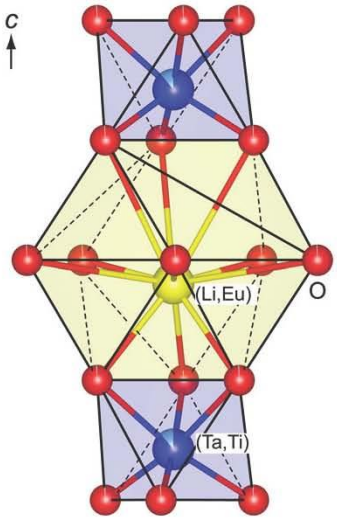


Figure 1. (Color online) Part of the crystal structure of $(Li_{0.977}Eu^{3+}_{0.023})(Ta_{0.89}Ti_{0.11})O_{2.968}$ viewed along [110], showing coordination polyhedra for (Li, Eu) and (Ta, Ti). Because the occupancy of the oxygen site is less than unity, the O atoms are depicted as red circle graphs for occupancies. Blue and cyan bicolor balls are for Ta (blue) and Ti (cyan) sites. Yellow and magenta bicolor balls are for Li (yellow) and Eu (magenta) sites. Structural parameters are determined by Uchida *et al.* (2013).

a)Author to whom correspondence should be addressed. Electronic mail: fukuda.koichiro@nitech.ac.jp

TABLE I. Phase composition (mol%).

| Sample | Doped lithium tantalate | $EuTaO_4$ | $Li_4Ti_5O_{12}$ | $Li_3TaO_4$ | Total |
|---|---|---|---|---|---|
| LETO | 99.90 | 0.10 | – | – | 100 |
| LETTO | 94.61 | – | 1.65 | 3.74 | 100 |
| LSTTO | 96.73 | – | – | 3.27 | 100 |
| LSMTTO | 96.74 | – | – | 3.26 | 100 |

TABLE II. Crystal data for $(Li_{0.925}Eu^{3+}{}_{0.025})TaO_3$.

| Chemical formula | $(Li_{0.925}Eu^{3+}{}_{0.025})TaO_3$ |
|---|---|
| Space group | *R*3*c* (No. 161) |
| *a*/nm | 0.515 741(2) |
| *c*/nm | 1.377 230(4) |
| *V*/nm$^3$ | 0.317 249(1) |
| *Z* | 6 |
| $D_x$/Mg m$^{-3}$ | 7.511 |

information especially on the coordination environment of the rare-earth ions.

We reported in our previous study the crystal structure of $(Li_{0.977}Eu^{3+}{}_{0.023})(Ta_{0.89}Ti_{0.11})O_{2.968}$ (Uchida *et al.*, 2013), the (Li, Eu) site position which was displayed clearly from three-dimensional (3D) electron-density distributions (EDDs). We used the recent analytical techniques for crystal-structure analysis from XRPD data, which includes combined use of the Rietveld method (Rietveld, 1967), the maximum-entropy method (MEM) (Takata *et al.*, 2001) and the MEM-based pattern fitting (MPF) method (Momma *et al.*, 2013). As the result of the alternately repeated MEM and MPF analyses (REMEDY cycle), we are able to visualize the EDDs that are free from the bias toward the structural models (Izumi *et al.*, 2001). Thus, the structural details can be seen clearly from the EDDs.

In the present study, we prepared four types of doped lithium tantalate phosphors; they are $Li(Ta_{1-x}Ti_x)O_{3-x/2}:Eu^{3+}$ with $x = 0$ and $x = 0.19$ and $(Li_{1-y}Mg_y)(Ta_{0.89}Ti_{0.11})O_{2.945+y/2}:Sm^{3+}$ with $y = 0$ and $y = 0.017$. We determined these crystal structures and compared their structural details together with those of $(Li_{0.977}Eu^{3+}{}_{0.023})(Ta_{0.89}Ti_{0.11})O_{2.968}$ ($x = 0.11$). The *z* coordinates of the (Li, Eu) and (Li, Sm, Mg) sites were markedly different among the isomorphous structures. Hence, we discuss the close relationship between the PL intensity and the coordination environment of these sites.

## II. EXPERIMENTAL

### A. Syntheses

We prepared four types of powder specimens with different starting compositions of [Li:Eu:Ta] = [0.965:0.035:1] (sample LETO), [Li:Eu:Ta:Ti] = [0.974:0.026:0.75:0.25] (sample LETTO), [Li:Sm:Ta:Ti] = [0.969:0.031:0.89:0.11] (sample LSTTO), and [Li:Sm:Mg:Ta:Ti] = [0.954:0.030:0.016:0.89:0.11] (sample LSMTTO) in atomic ratio from the chemicals of $Li_2CO_3$, $Eu_2O_3$, $Sm_2O_3$, MgO, $Ta_2O_5$, and $TiO_2$. Each of the well-mixed chemicals was heated at 1273 K for 3 h, and then successively at 1423 K for 24 h (samples LETO and LETTO) and for 15 h (samples LSTTO and LSMTTO), and finally cooled to ambient temperature. We finely ground the densely sintered pellets and obtained the fine powder specimens suitable for XRPD. The former two samples (LETO and LSTTO) were prepared under exactly the same experimental conditions as those of $Li(Ta_{1-x}Ti_x)O_{3-x/2}:Eu^{3+}$ phosphors examined for PL properties in a previous study (Nakano *et al.*, 2012).

### B. Characterization

The XRPD intensities in the $2\theta$ range of 10.0°–149.0° ($CuK\alpha_1$) with 15 559 total data points were collected on a diffractometer in the Bragg–Brentano geometry (X'Pert PRO Alpha-1, PANalytical B.V., Almelo, The Netherlands). The X-ray generator was operated at 45 kV and 40 mA. We used a computer program VESTA (Momma and Izumi, 2011) to visualize the structural models, equidensity isosurfaces of EDDs and 2D EDD maps. Distortion parameters for the coordination polyhedra were determined using a computer program IVTON (Balic-Zunic and Vickovic, 1996). Excitation and emission spectra were obtained for the $(Li_{1-y}Mg_y)(Ta_{0.89}Ti_{0.11})O_{2.945+y/2}:Sm^{3+}$ phosphors by a PL spectrometer (model FP-6500, JASCO International Co., Ltd., Tokyo, Japan). We measured the PL intensities on the sintered sample surface to eliminate the effects of powder particle size and degree of crystallinity.

## III. RESULTS AND DISCUSSION

### A. Crystal structure refinements and electron-density distributions

The sample LETO was composed of both $Eu^{3+}$-doped lithium tantalate and a small amount of $EuTaO_4$ (Krylov and Strelina, 1963). We successfully indexed the XRPD peaks, corresponding to the doped lithium tantalate, with a hexagonal unit cell. Initial structural parameters were taken from those of $(Li_{0.977}Eu^{3+}{}_{0.023})(Ta_{0.89}Ti_{0.11})O_{2.968}$ (space group *R*3*c*) determined by Uchida *et al.* (2013). There is one (Li, Eu) site and one Ta site, both of which are located at the Wyckoff position 6*a*, and one O site at 18*b* in the hexagonal unit cell ($Z = 6$). We refined the structural parameters of all atoms using the Rietveld method on a computer program RIETAN-FP (Izumi and Momma, 2007). We quantitatively determined the phase composition of the sample using the phase-analysis method based on Brindley's procedure

TABLE III. Structural parameters and isotropic atomic displacement parameters ($100 \times B$/nm$^2$) for $(Li_{0.925}Eu^{3+}{}_{0.025})TaO_3$.

| Site position | Wyckoff | *g* | *x* | *y* | *z* | $100 \times B$/nm$^2$ |
|---|---|---|---|---|---|---|
| (Li,Eu) | 6*a* | 0.925/0.025 | 0 | 0 | 0.2795(5) | 1.3 |
| Ta | 6*a* | 1.0 | 0 | 0 | 0 | 0.40(5) |
| O | 18*b* | 1.0 | 0.0450(10) | 0.3243(14) | 0.0969(3) | 0.52(8) |

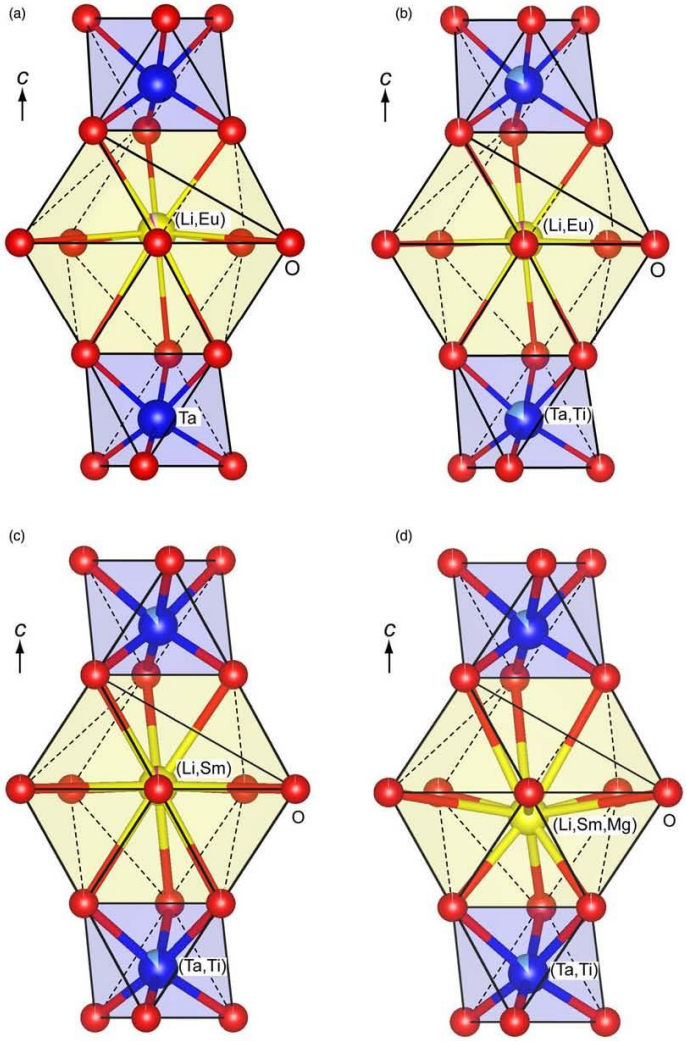


Figure 2. (Color online) (a) Part of the crystal structure viewed along [110] of $(Li_{0.925}Eu^{3+}_{0.025})TaO_3$ in sample LETO. Yellow and magenta bicolor balls are for Li (yellow) and Eu (magenta) sites. Blue balls are for Ta sites. (b) Part of the crystal structure viewed along [110] of $(Li_{0.968}Eu^{3+}_{0.032})(Ta_{0.81}Ti_{0.19})O_{2.937}$ in sample LETTO. Yellow and magenta bicolor balls are for Li (yellow) and Eu (magenta) sites. Because the occupancy of the oxygen site is less than unity, the O atoms are depicted as red circle graphs for occupancies. Blue and cyan bicolor balls are for Ta (blue) and Ti (cyan) sites. (c) Part of the crystal structure viewed along [110] of $(Li_{0.967}Sm^{3+}_{0.033})(Ta_{0.89}Ti_{0.11})O_{2.978}$ in sample LSTTO. Yellow and magenta bicolor balls are for Li (yellow) and Sm (magenta) sites. Because the occupancy of the oxygen site is less than unity, the O atoms are depicted as red circle graphs for occupancies. Blue and cyan bicolor balls are for Ta (blue) and Ti (cyan) sites. (d) Part of the crystal structure viewed along [110] of $(Li_{0.950}Sm^{3+}_{0.033}Mg_{0.017})(Ta_{0.89}Ti_{0.11})O_{2.987}$ in sample LSMTTO. Yellow and magenta bicolor balls are for Li (yellow) and (Sm, Mg) (magenta) sites. Because the occupancy of the oxygen site is less than unity, the O atoms are depicted as red circle graphs for occupancies. Blue and cyan bicolor balls are for Ta (blue) and Ti (cyan) sites.

TABLE IV. Crystal data for $(Li_{0.968}Eu^{3+}_{0.032})(Ta_{0.81}Ti_{0.19})O_{2.937}$.

| Chemical formula | $(Li_{0.968}Eu^{3+}_{0.032})(Ta_{0.81}Ti_{0.19})O_{2.937}$ |
|---|---|
| Space group | $R3c$ (No. 161) |
| $a$/nm | 0.518 222(3) |
| $c$/nm | 1.372 199(7) |
| $V$/nm$^3$ | 0.319 139(3) |
| $Z$ | 6 |
| $D_x$/Mg m$^{-3}$ | 6.688 |

TABLE V. Crystal data for $(Li_{0.967}Sm^{3+}_{0.033})(Ta_{0.89}Ti_{0.11})O_{2.978}$.

| Chemical formula | $(Li_{0.967}Sm^{3+}_{0.033})(Ta_{0.89}Ti_{0.11})O_{2.978}$ |
|---|---|
| Space group | $R3c$ (No. 161) |
| $a$/nm | 0.517 857(3) |
| $c$/nm | 1.373 060(6) |
| $V$/nm$^3$ | 0.318 889(3) |
| $Z$ | 6 |
| $D_x$/Mg m$^{-3}$ | 7.050 |

TABLE VI. Crystal data for $(Li_{0.950}Sm^{3+}_{0.033}Mg_{0.017})(Ta_{0.89}Ti_{0.11})O_{2.987}$.

| Chemical formula | $(Li_{0.950}Sm^{3+}_{0.033}Mg_{0.017})(Ta_{0.89}Ti_{0.11})O_{2.987}$ |
|---|---|
| Space group | $R3c$ (No. 161) |
| $a$/nm | 0.517 517(3) |
| $c$/nm | 1.373 688(7) |
| $V$/nm$^3$ | 0.318 616(3) |
| $Z$ | 6 |
| $D_x$/Mg m$^{-3}$ | 7.070 |

(Brindley, 1945), the subroutine of which was implemented in the program RIETAN-FP. The phase composition was, under the condition of effective particle radii being 5.00 $\mu$m, found to be 99.90 mol% $Eu^{3+}$-doped lithium tantalate and 0.10 mol% $EuTaO_4$ (Table I). We determined the chemical formula of the former by subtracting the $EuTaO_4$ component from the bulk chemical composition. Because the bulk atomic ratio of sample LETO was [Li:Eu:Ta] = [0.965:0.035:1], the chemical formula should be $(Li_{0.925}Eu^{3+}_{0.025})TaO_3$ ($x = 0$). The Rietveld refinement result was satisfactory due to the relatively low reliability ($R$) indices (Young, 1993) of $R_{wp}$ = 10.14%, $S(=R_{wp}/R_e) = 1.29$%, $R_p = 7.24$%, $R_B = 2.84$%, and $R_F = 1.40$%. We summarized the crystal data in Table II, and the final atomic positional parameters and isotropic atomic displacement parameters (ADPs) in Table III, where the figures in parentheses of these tables indicate estimated standard uncertainties.

We visualized the 3D EDDs with 108 × 108 × 276 voxels in the unit cell, the spatial resolution of which is ~0.005 nm, using the MPF method on the computer programs Dysnomia (Momma *et al.*, 2013) and RIETAN-FP to confirm the validity of the structural model (Figure S1(a) in Supplemental Data). The one REMEDY cycle further decreased the $R_B$- and $R_F$-indices to 1.63 and 0.80%, respectively ($R_{wp} = 10.00$%, $S = 1.27$, and $R_p = 6.89$%). The reduction of these $R$-indices, which must be induced by slight improvements of EDDs, implies that the EDDs more clearly demonstrate the structural details as compared with the ball-and-stick model in Figure 2(a). The XRPD patterns that are obtained by observation and calculation for the final MPF, together with their difference, are plotted in Figure S2(a) (see Supplemental Data).

The other samples of LETTO, LSTTO, and LSMTTO were composed of doped lithium titanotantalate and small amounts of impurities of $Li_3TaO_4$ (Agulyanskii *et al.*, 1986) and/or $Li_4Ti_5O_{12}$ (Leonidov *et al.*, 2003). The analytical processes for these samples were very similar to that of LETO aforementioned. We determined the phase compositions (Table I) and subsequently determined the chemical formulae of doped lithium titanotantalate compounds from calculation by subtracting the impurity components from the bulk chemical compositions. We obtained the satisfactory $R$ indices for

TABLE VII. Structural parameters and isotropic atomic displacement parameters ($100 \times B$/nm$^2$) for $(Li_{0.968}Eu^{3+}_{0.032})(Ta_{0.81}Ti_{0.19})O_{2.937}$.

| Site position | Wyckoff | $g$ | $x$ | $y$ | $z$ | $100 \times B$/nm$^2$ |
|---|---|---|---|---|---|---|
| (Li,Eu) | 6$a$ | 0.968/0.032 | 0 | 0 | 0.2684(5) | 0.8(1) |
| (Ta,Ti) | 6$a$ | 0.81/0.19 | 0 | 0 | 0 | 0.19(3) |
| O | 18$b$ | 0.979 | 0.0439(11) | 0.3201(17) | 0.0960(4) | 0.48(6) |

TABLE VIII. Structural parameters and isotropic atomic displacement parameters ($100 \times B$/nm$^2$) for $(Li_{0.967}Sm^{3+}_{0.033})(Ta_{0.89}Ti_{0.11})O_{2.978}$.

| Site position | Wyckoff | $g$ | $x$ | $y$ | $z$ | $100 \times B$/nm$^2$ |
|---|---|---|---|---|---|---|
| (Li,Sm) | 6$a$ | 0.967/0.033 | 0 | 0 | 0.2671(4) | 0.9(1) |
| (Ta,Ti) | 6$a$ | 0.89/0.11 | 0 | 0 | 0 | 0.54(4) |
| O | 18$b$ | 0.993 | 0.0520(14) | 0.3216(22) | 0.0955(5) | 0.87(8) |

TABLE IX. Structural parameters and isotropic atomic displacement parameters ($100 \times B$/nm$^2$) for $(Li_{0.950}Sm^{3+}_{0.033}Mg_{0.017})(Ta_{0.89}Ti_{0.11})O_{2.987}$.

| Site position | Wyckoff | $g$ | $x$ | $y$ | $z$ | $100 \times B$/nm$^2$ |
|---|---|---|---|---|---|---|
| (Li,Sm,Mg) | 6$a$ | 0.950/0.033/0.017 | 0 | 0 | 0.2291(5) | 1.2(1) |
| (Ta,Ti) | 6$a$ | 0.89/0.11 | 0 | 0 | 0 | 0.54(8) |
| O | 18$b$ | 0.996 | 0.0604(15) | 0.323 52(23) | 0.0961(4) | 0.7(1) |

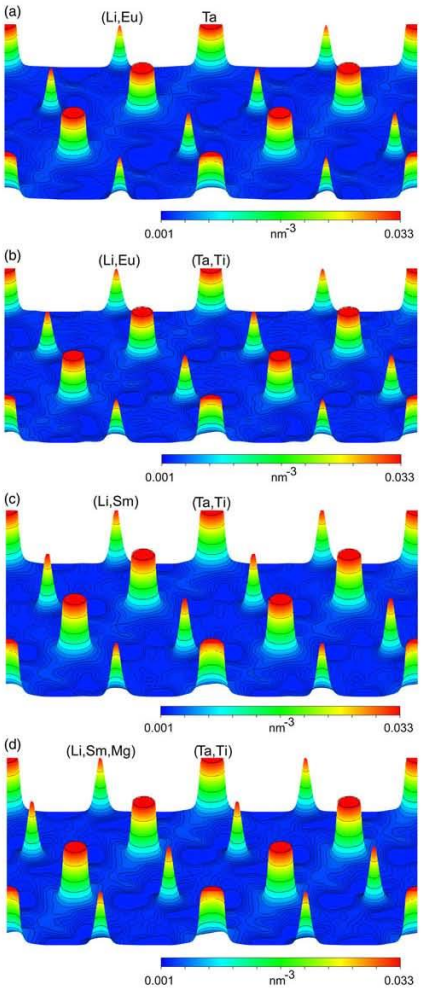


Figure 3. (Color online) (a) Bird's eye view of electron densities determined by MPF of the (Li, Eu) and Ta atoms on the (110) plane of $(Li_{0.925}Eu^{3+}_{0.025})TaO_3$ in sample LETO. (b) Bird's eye view of electron densities determined by MPF of the (Li, Eu) and (Ta, Ti) atoms on the (110) plane of $(Li_{0.968}Eu^{3+}_{0.032})(Ta_{0.81}Ti_{0.19})O_{2.937}$ in sample LETTO. (c) Bird's eye view of electron densities determined by MPF of the (Li, Sm) and (Ta, Ti) atoms on the (110) plane of $(Li_{0.967}Sm^{3+}_{0.033})(Ta_{0.89}Ti_{0.11})O_{2.978}$ in sample LSTTO. (d) Bird's eye view of electron densities determined by MPF of the (Li, Sm, Mg) and (Ta, Ti) atoms on the (110) plane of $(Li_{0.950}Sm^{3+}_{0.033}Mg_{0.017})(Ta_{0.89}Ti_{0.11})O_{2.987}$ in sample LSMTTO.

all of the Rietveld refinements (Table SI in Supplemental Data), the refined structural models of which are shown in Figures S1(b)–S1(d) (see Supplemental Data). The crystal data of doped lithium titanotantalate compounds are given in Tables IV, V and VI, and the final atomic positional parameters and isotropic ADPs are given in Tables VII, VIII and IX, where the figures in parentheses of these tables indicate estimated standard uncertainties. We applied the MPF method and further decreased the $R$ indices after two REMEDY cycles (Table SI in Supplemental Data). Observed, calculated, and difference XRPD patterns for the final MPF are plotted in Figures S2(b)–S2(d) (see Supplemental Data).

Figures 2(a)–2(d) show parts of the refined crystal structures of doped lithium tantalate phosphors, the chemical formulas of which are $(Li_{0.925}Eu^{3+}_{0.025})TaO_3$ ($x = 0$) in sample LETO, $(Li_{0.968}Eu^{3+}_{0.032})(Ta_{0.81}Ti_{0.19})O_{2.937}$ ($x = 0.19$) in sample LETTO, $(Li_{0.967}Sm^{3+}_{0.033})(Ta_{0.89}Ti_{0.11})O_{2.978}$ ($y = 0$) in sample LSTTO, and $(Li_{0.950}Sm^{3+}_{0.033}Mg_{0.017})(Ta_{0.89}Ti_{0.11})O_{2.987}$ ($y = 0.017$) in sample LSMTTO. We confirmed that all of them are isostructural with $(Li_{0.977}Eu^{3+}_{0.023})(Ta_{0.89}Ti_{0.11})O_{2.968}$ ($x = 0.11$) (Uchida *et al.*, 2013). The individual equidensity isosurfaces of 3D EDDs were in accord with the arrangements of atoms. The 2D EDD maps show that the positions of (Li, Eu, Sm, Mg) and (Ta, Ti) sites are successfully disclosed by the EDDs (Figure 3). The EDD voxel data have several local maximum, which correspond to the coordinates of atoms. We determined the amounts of deviations between the maxima positions and corresponding atomic coordinates to find that they were necessarily less than 0.003 nm, which is within the resolution limit of the 3D EDDs. Thus, we concluded that the refined structural models would satisfactorily represent the corresponding crystal structures.

### B. Structure comparison and photoluminescence property

The coordination elements of each structure are the [(Ta, Ti)$O_6$] octahedron and [(Li, Eu, Sm, Mg)$O_{12}$] polyhedron. Selected interatomic distances and their standard deviations are listed in Tables SII–SV (see Supplemental Data). In comparing the polyhedral distortion parameters of [(Ta, Ti)$O_6$] octahedra (Table X) among the four isomorphous structures, together with those of $(Li_{0.977}Eu^{3+}_{0.023})(Ta_{0.89}Ti_{0.11})O_{2.968}$ (Uchida *et al.*, 2013), we found that the $V_S/V_P$-values (i.e., the ratios of the volumes of the circumscribed sphere and the polyhedron) ranged between 3.129 and 3.157, and hence they were close to the relevant value of regular octahedron ( = 3.1416) (Makovicky and Balic-Zunic, 1998). Thus, the [(Ta, Ti)$O_6$] polyhedra were only slightly distorted from the regular octahedra. The values for distortion parameters ($\Delta$ $r_S$, $V_S$, $\sigma$, and $V_P$) were almost the same among the five phosphors, hence we concluded that the [(Ta, Ti)$O_6$] octahedra were all comparable with one another. With [(Li, Eu, Sm, Mg)$O_{12}$] polyhedra, the centroid-to-(Li, Eu, Sm, Mg) distances ($\Delta$-values) widely varied from 0.004 to 0.047 among the five compounds, although the other polyhedral parameter values ($r_S$, $V_S$, $\sigma$, and $V_P$) were almost unchanged (Table X).

Here, we compare the eccentricity vectors $\boldsymbol{\Delta}$, which are defined from the centroids to the (Li, Eu, Sm, Mg) sites of the [(Li, Eu, Sm, Mg)$O_{12}$] polyhedra, to indicate more clearly the features of the crystal structures of $Li(Ta_{1-x}Ti_x)O_{3-x/2}:Eu^{3+}$ and $(Li_{1-y}Mg_y)(Ta_{0.89}Ti_{0.11})O_{2.945+y/2}:Sm^{3+}$ by the directions of $\boldsymbol{\Delta}$ as well as their magnitudes $|\boldsymbol{\Delta}|$ (Uchida *et al.*, 2013). With $(Li_{0.977}Eu^{3+}_{0.023})(Ta_{0.89}Ti_{0.11})O_{2.968}$ ($x = 0.11$)

TABLE X. Polyhedral distortion parameters.

| Compound | Polyhedron | $\Delta$/nm | $r_S$/nm | $V_S$/nm$^3$ | $\sigma$ | $V_P$/nm$^3$ | $V_S/V_P$ |
|---|---|---|---|---|---|---|---|
| $(Li_{0.925}Eu^{3+}_{0.025})TaO_3$ | [(Li,Eu)$O_{12}$] | 0.019 | 0.269 | 0.0971 | 0.821 | 0.0428 | 2.269 |
| | [$TaO_6$] | 0.014 | 0.198 | 0.0323 | 1 | 0.0103 | 3.136 |
| $(Li_{0.968}Eu^{3+}_{0.032})(Ta_{0.81}Ti_{0.19})O_{2.937}$ | [(Li,Eu)$O_{12}$] | 0.004 | 0.270 | 0.0974 | 0.830 | 0.0431 | 2.260 |
| | [(Ta,Ti)$O_6$] | 0.010 | 0.198 | 0.0325 | 1 | 0.0103 | 3.155 |
| $(Li_{0.977}Eu^{3+}_{0.023})(Ta_{0.89}Ti_{0.11})O^*_{2.968}$ | [(Li,Eu)$O_{12}$] | 0.047 | 0.270 | 0.0981 | 0.826 | 0.0429 | 2.287 |
| | [(Ta,Ti)$O_6$] | 0.012 | 0.198 | 0.0326 | 1 | 0.0104 | 3.135 |
| $(Li_{0.967}Sm^{3+}_{0.033})(Ta_{0.89}Ti_{0.11})O_{2.978}$ | [(Li,Sm)$O_{12}$] | 0.006 | 0.269 | 0.0965 | 0.833 | 0.0429 | 2.249 |
| | [(Ta,Ti)$O_6$] | 0.016 | 0.197 | 0.0322 | 1 | 0.0102 | 3.157 |
| $(Li_{0.950}Sm^{3+}_{0.033}Mg_{0.017})(Ta_{0.89}Ti_{0.11})O_{2.987}$ | [(Li,Sm,Mg)$O_{12}$] | 0.046 | 0.269 | 0.0945 | 0.843 | 0.0431 | 2.193 |
| | [(Ta,Ti)$O_6$] | 0.019 | 0.196 | 0.0316 | 1 | 0.0101 | 3.129 |

$\Delta$, centroid-to-cation distance (eccentricity); $r_S$, radius of sphere fitted to ligands; $V_S$, sphere volume; $\sigma$, sphericity; $V_P$, volume of coordination polyhedron. For explanation, see Makovicky and Balic-Zunic (1998).
* Structural parameters by Uchida *et al.* (2013).

(Figure 1), the eccentricity vector $\Delta$ is in the [00$\bar{1}$] direction and $|\Delta|$ = 0.047 nm. On the other hand, the $\Delta$ vectors for $(Li_{0.925}Eu^{3+}_{0.025})TaO_3$ ($x$ = 0) (Figure 2(a)) and $(Li_{0.968}Eu^{3+}_{0.032})(Ta_{0.81}Ti_{0.19})O_{2.937}$ ($x$ = 0.19) (Figure 2(b)) are in the [001] direction with the smaller magnitudes of 0.019 and 0.004 nm, respectively. Thus, the marked difference among the three phosphors was clarified as the degree of eccentricity along the $c$-axis of the (Li, Eu) position in [(Li, Eu)$O_{12}$]. Because the concentrations of Eu in the (Li, Eu) sites are relatively low and nearly the same among the three compounds with $x$ = 0, 0.11, and 0.19, the replacement of Ti for Ta would mainly induce the displacement of the (Li, Eu) site along the $c$-axis, without changing the outer shapes of both [(Li, Eu)$O_{12}$] and [(Ta, Ti)$O_6$] polyhedra. The PL intensities determined by Nakano *et al.* (2012) were highest for the Li$(Ta_{1-x}Ti_x)O_{3-x/2}$:$Eu^{3+}$ phosphor with $x$ = 0.11, followed by those with $x$ = 0.19 and $x$ = 0 (Figure 4). This strongly suggests that the displacement of the $Eu^{3+}$ position from the centroid of [(Li, Eu)$O_{12}$] polyhedra contributes to the highly enhanced hypersensitive $^5D_0$–$^7F_2$ transition in $Eu^{3+}$ when excited by near-UV light (Nakano *et al.*, 2012). The slight change of coordination environment of $Eu^{3+}$ ion would markedly affect the *f*-*f* transition process, which would eventually cause an increase of emission intensity.

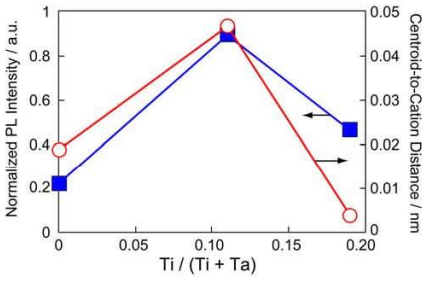


Figure 4. (Color online) Relationship between normalized photoluminescence (PL) intensity and centroid-to-cation distance ($\Delta$-value) of [(Li, Eu)$O_{12}$] polyhedra with Ti/(Ti + Ta) ratio (=$x$) for Li$(Ta_{1-x}Ti_x)O_{3-x/2}$:$Eu^{3+}$. The PL intensity data are from Nakano *et al.* (2012). The $\Delta$-value with $x$ = 0.11 is from Uchida *et al.* (2013).

With $(Li_{0.967}Sm^{3+}_{0.033})(Ta_{0.89}Ti_{0.11})O_{2.978}$ ($y$ = 0), the eccentricity vector $\Delta$ is in the [001] direction with $|\Delta|$ = 0.006 nm, whereas the $\Delta$ vector of $(Li_{0.950}Sm^{3+}_{0.033}Mg_{0.017})(Ta_{0.89}Ti_{0.11})O_{2.987}$ ($y$ = 0.017) is in the opposite direction with the larger $|\Delta|$-value of 0.046 nm (Figures 2(c) and 2(d)). Accordingly, the prominent difference between the two compounds was clarified as the degree of eccentricity along the $c$-axis of the (Li, Sm, Mg) position in [(Li, Sm, Mg)$O_{12}$]. The concentrations of $Sm^{3+}$ in the Li sites of $(Li_{1-y}Mg_y)(Ta_{0.89}Ti_{0.11})O_{2.945+y/2}$:$Sm^{3+}$ are exactly the same between the two compounds with $y$ = 0 and $y$ = 0.017, hence the replacement of Mg for Li would mainly induce the displacement of the (Li, Sm, Mg) site along the $c$-axis, keeping both [(Li, Sm, Mg)$O_{12}$] and [(Ta, Ti)$O_6$] polyhedra nearly undistorted. Each of the PL spectra in the range

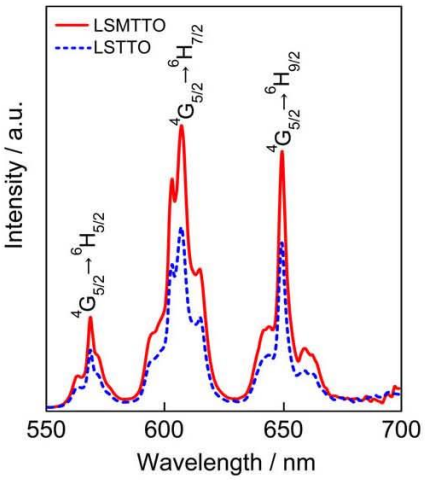


Figure 5. (Color online) Photoluminescence (PL) emission spectra of $(Li_{0.967}Sm^{3+}_{0.033})(Ta_{0.89}Ti_{0.11})O_{2.978}$ in sample LSTTO and $(Li_{0.950}Sm^{3+}_{0.033}Mg_{0.017})(Ta_{0.89}Ti_{0.11})O_{2.987}$ in sample LSMTTO, showing the higher PL intensity for the latter phosphor ($\lambda_{ex}$ = 410 nm).

550–680 nm, recorded at the excitation wavelength 410 nm, is caused by the $^4G_{5/2} \rightarrow {}^6H_J$ transitions of $Sm^{3+}$ ion (Sakirzanovas *et al.*, 2011; Dillip *et al.*, 2013) and consists of three groups of narrow band emission in the range of 550–585 ($J = 5/2$), 585–625 ($J = 7/2$), and 630–680 ($J = 9/2$) (Figure 5). Among them, the most intense band is located at ~607 nm because of the $^4G_{5/2} \rightarrow {}^6H_{7/2}$ transition. The relevant PL intensities were ~1.6 times higher for $(Li_{0.950}Sm^{3+}_{0.033}Mg_{0.017})(Ta_{0.89}Ti_{0.11})O_{2.987}$ ($y = 0.017$) than for $(Li_{0.967}Sm^{3+}_{0.033})(Ta_{0.89}Ti_{0.11})O_{2.978}$ ($y = 0$), which strongly suggests that the displacement of the $Sm^{3+}$ position from the centroid of [(Li, Sm, Mg)$O_{12}$] polyhedra contributes to the higher PL efficiency.

We have confirmed that the crystal structures of doped lithium tantalate phosphors are flexible with respect to the substitution of $Eu^{3+}$, $Sm^{3+}$, and Mg for Li and that of Ti for Ta. A more detailed discussion on the PL properties of $Li(Ta_{1-x}Ti_x)O_{3-x/2}:Eu^{3+}$ and $(Li_{1-y}Mg_y)(Ta_{0.89}Ti_{0.11})O_{2.945+y/2}:Sm^{3+}$ would be made based on the comparison among the electronic states of these compounds, which might be determined by, for example, density functional theory. The reliable atomic coordinates, which are essential for the theoretical calculations, are available at the moment for the doped lithium tantalate phosphors.

## IV. CONCLUSION

We clarified the slight differences among the crystal structures of $Li(Ta_{1-x}Ti_x)O_{3-x/2}:Eu^{3+}$ ($x = 0$ and 0.19) and $(Li_{1-y}Mg_y)(Ta_{0.89}Ti_{0.11})O_{2.945+y/2}:Sm^{3+}$ ($y = 0$ and 0.017), each of which is made up of two types of polyhedra [(Li, Eu, Sm, Mg)$O_{12}$] and [(Ta, Ti)$O_6$]. The 3D EDDs determined by MPF method well supported the validity of the structural models. The substitution of Ti for Ta and that of Mg for Li displaced, respectively, the (Li, Eu) site of $Li(Ta_{1-x}Ti_x)O_{3-x/2}:Eu^{3+}$ and (Li, Sm, Mg) site of $(Li_{1-y}Mg_y)(Ta_{0.89}Ti_{0.11})O_{2.945+y/2}:Sm^{3+}$ along their *c*-axes, without changing the outer shapes of both [(Li, Eu, Sm, Mg)$O_{12}$] and [(Ta, Ti)$O_6$] polyhedra. The eccentricity of the $Eu^{3+}$ and $Sm^{3+}$ positions in [(Li, Eu, Sm, Mg)$O_{12}$] thus seems to be closely related to the PL efficiency of the doped lithium tantalate phosphors. Based on the sufficient experimental evidence for the relevant phosphors, we could be able to formulate the relationship between the magnitude of eccentricity and photoluminescence intensity.

## SUPPLEMENTARY MATERIALS

For supplementary material for this article, please visit http://dx.doi.org/10.1017/S0885715615000688


## ACKNOWLEDGMENT

This work was partially supported by a Grant-in-Aid for Scientific Research (c) No. 25420709 by the Japan Society for the Promotion of Science (H. N.).



Agulyanskii, A. I., Bessonova, V. A., Kuznetsov, V. Ya., and Kalinnikov, V. T. (**1986**). "Double oxide fluorides with a sodium chloride structure," Russ. J. Inorg. Chem. **31**, 1548–1549.

Balic-Zunic, T. and Vickovic, I. (**1996**). "IVTON – a program for the calculation of geometrical aspects of crystal structures and some crystal chemical applications," J. Appl. Crystallogr. **29**, 305–306.

Brindley, G. W. (**1945**). "A theory of X-ray absorption in mixed powders," Philos. Mag. **36**, 347–369.

Dillip, G. R., Kumar, P. M., Raju, B. D. P., and Dhoble, S. J. (**2013**). "Synthesis and luminescence properties of a novel $Na_6CaP_2O_9:Sm^{3+}$ phosphor," J. Lumin. **134**, 333–338.

Hsu, R., Maslen, E. N., Du Boulay, D., and Ishizawa, N. (**1997**). "Synchrotron X-ray studies of $LiNbO_3$ and $LiTaO_3$," Acta Crystallogr., Sect. B: Struct. Sci. **53**, 420–428.

Izumi, F. and Momma, K. (**2007**). "Three-dimensional visualization in powder diffraction," Solid State Phenom. **130**, 15–20.

Izumi, F., Kumazawa, S., Ikeda, T., Hu, W.-Z., Yamamoto, A., and Oikawa, K. (**2001**). "MEM-based structure-refinement system REMEDY and its applications," Mater. Sci. Forum **378–381**, 59–64.

Krylov, E. I. and Strelina, M. M. (**1963**). "Orthotantalates of lanthanum, samarium, and europium," Russ. J. Inorg. Chem. **8**, 1180–1182.

Leonidov, I. A., Leonidova, O. N., Perelyaeva, L. A., Samigullina, R. F., Kovyazina, S. A., and Patrakeev, M. V. (**2003**). "Structure, ionic conduction, and phase transformations in lithium titanate $Li_4Ti_5O_{12}$," Phys. Solid State **45**, 2183–2188.

Makovicky, E. and Balic-Zunic, T. (**1998**). "New measure of distortion for coordination polyhedra," Acta Crystallogr. Sect. B: Struct. Sci. **B54**, 766–773.

Momma, K. and Izumi, F. (**2011**). "VESTA 3 for three-dimensional visualization of crystal, volumetric and morphology data," J. Appl. Crystallogr. **44**, 1272–1276.

Momma, K., Ikeda, T., Belik, A. A., and Izumi, F. (**2013**). "Dysnomia, a computer program for maximum-entropy method (MEM) analysis and its performance in the MEM-based pattern fitting," Powder Diffr. **28**, 184–193.

Nakano, H., Ozono, K., Hayashi, H., and Fujihara, S. (**2012**). "Synthesis and luminescent properties of a new $Eu^{3+}$-Doped $Li_{1+x}(Ta_{1-z}Nb_z)_{1-x}Ti_xO_3$ red phosphor," J. Am. Ceram. Soc. **95**, 2795–2797.

Nakano, H., Suehiro, S., Furuya, S., Hayashi, H., and Fujihara, S. (**2013**). "Synthesis of new $RE^{3+}$ doped $Li_{1+x}Ta_{1-x}Ti_xO_3$ (RE: Eu, Sm, Er, Tm, and Dy) phosphors with various emission colors," Materials **6**, 2768–2776.

Rietveld, H. M. (**1967**). "Line profiles of neutron powder-diffraction peaks for structure refinement," Acta Crystallogr. **22**, 151–152.

Sakirzanovas, S., Katelnikovas, A., Bettentrup, H., Kareiva, A., and Jüstel, T. (**2011**). "Synthesis and photoluminescence properties of $Sm^{3+}$-doped $LaMgB_5O_{10}$ and $GdMgB_5O_{10}$," J. Lumin. **131**, 1525–1529.

Takata, M., Nishibori, E., and Sakata, M. (**2001**). "Charge density studies utilizing powder diffraction and MEM. Exploring of high Tc superconductors, C60 superconductors and manganites," Z. Kristallogr. **216**, 71–86.

Uchida, T., Suehiro, S., Asaka, T., Nakano, H., and Fukuda, K. (**2013**). "Syntheses and crystal structures of $Li(Ta_{0.89}Ti_{0.11})O_{2.945}$ and $(Li_{0.977}Eu_{0.023})(Ta_{0.89}Ti_{0.11})O_{2.968}$," Powder Diffr. **28**, 178–183.

Young, R. A. (**1993**). "Introduction to the Rietveld method," in *The Rietveld Method*, edited by R. A. Young (Oxford University Press, Oxford, U.K.), pp. 1–38.

# その他の構造・組成制御した無機材料の合成と解析

THE JOURNAL OF PHYSICAL CHEMISTRY C

Article

pubs.acs.org/JPCC

# Crystal Structure, Optical Properties, and Electronic Structure of Calcium Strontium Tungsten Oxynitrides $Ca_xSr_{1-x}WO_2N$

Masatomo Yashima,*[,†] Uhi Fumi,[‡] Hiromi Nakano,[§] Kazuki Omoto,[‡] and James R. Hester[∥]

[†]Department of Chemistry and Materials Science, Tokyo Institute of Technology, 2-12-1-W4-17, O-okayama, Meguro-ku, Tokyo, 152-8551, Japan

[‡]Department of Materials Science and Engineering, Tokyo Institute of Technology, 2-12-1-W4-17, O-okayama, Meguro-ku, Tokyo, 152-8551, Japan

[§]Cooperative Research Facility Center, Toyohashi University of Technology, Hibarigaoka 1-1, Tempaku, Toyohashi-shi, 441-8580, Japan

[∥]The Bragg Institute, Australian Nuclear Science and Technology Organisation, Lucas Heights, NSW 2234, Australia

Supporting Information

**ABSTRACT:** Novel calcium strontium tungsten oxynitrides $Ca_xSr_{1-x}WO_2N$ ($x$ = 0.25 and 0.5) have been synthesized. The crystal and electronic structures, electron-density distribution, and optical properties of $Ca_xSr_{1-x}WO_2N$ and $Ca_xSr_{1-x}WO_4$ ($x$ = 0, 0.25, and 0.5) have been investigated by neutron, synchrotron, and X-ray powder diffraction; transmission electron microscopy energy-dispersive spectroscopy (TEM-EDS); scanning electron microscopy; UV−visible reflectance measurements; and ab initio density functional theory (DFT)-based calculations. Precursor materials $Ca_xSr_{1-x}WO_4$ ($x$ = 0, 0.25, 0.5, and 1) with a scheelite-type structure were prepared by solid-state reactions, and heated at 900 °C for 5 h under an ammonia flow. The main phase in the product for the composition $x$ = 1 was metallic tungsten W, whereas cubic $Pm\bar{3}m$ perovskite-type oxynitrides $Ca_xSr_{1-x}WO_2N$ were obtained for the compositions $x$ = 0, 0.25, and 0.5. The unit-cell parameter $a$ of the cubic perovskite-type $Ca_xSr_{1-x}WO_2N$ obtained from the Rietveld analysis of synchrotron X-ray and neutron powder diffraction data decreases with an increase of Ca concentration $x$ ($0 \le x \le 0.5$), which indicates the substitution of Ca for Sr. The existence of nitrogen in $Ca_xSr_{1-x}WO_2N$ was confirmed by (1) the refined occupancy factor in the Rietveld analysis of neutron data and (2) EDS. The maximum-entropy-method electron-density analysis combined with the DFT calculations indicates W−N and W−O covalent bonds in $Ca_xSr_{1-x}WO_2N$, which are formed by the overlapping of W 5d and anion 2p orbitals. The minimum electron density at the W−N bond is higher than that at the W−O one, which indicates that the W−N bond is more covalent due to the smaller difference in the electronegativity between W and N atoms compared to the W and O ones. The oxidation number of W in $Ca_xSr_{1-x}WO_2N$ was estimated to be 5.2 by bond valence sum, which indicates the $W^{5+}$ ion with the $5d^1$ electron configuration. Precursor oxides $Ca_xSr_{1-x}WO_4$ with $W^{6+}$ having the $5d^0$ electron configuration are white and insulating, whereas the $Ca_xSr_{1-x}WO_2N$ oxynitrides with the $W^{5+}$ ion having the $5d^1$ configuration are black and exhibit metallic character. These results indicate the insulator−metal transition from the $d^0$ oxide $Ca_xSr_{1-x}WO_4$ to the $d^1$ oxynitride $Ca_xSr_{1-x}WO_2N$.

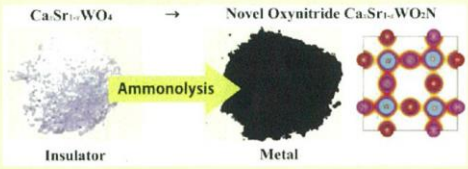


## INTRODUCTION

Many perovskite-type $ABO_3$ oxides are promising materials for energy, environments, and electronics where the $A$ and $B$ are the larger and smaller cations, respectively.[1−9] Recently, mixed anion systems, such as metal oxynitrides, have received much attention. The 2p orbitals of nitrogen have a higher energy level than that of oxygen; therefore, the partial replacement of oxygen by nitrogen in perovskite-type oxides $ABO_{3-x}N_x$ leads to a band gap reduction, where the $x$ is the concentration of nitrogen in the anions.[10−25] Therefore, the perovskite-type oxynitrides often exhibit intense colors and have potential applications, such as visible-light-driven photocatalysts[15,25] and nontoxic pigments.[14]

Oxynitrides containing tungsten (W) are of interest because of a variety of oxidation states of W[26] and their high photocatalytic activity.[25] Fawcett et al.[12] synthesized the perovskite-type strontium tungsten oxynitride $SrWO_2N$ by the ammonolysis of the scheelite-type $SrWO_4$ at 900 °C. The reaction formula can be described approximately as follows.

$$ABO_4 + (1/2)N_2 + 2H_2 \rightarrow ABO_2N + 2H_2O$$

Here, $A$ and $B$ are larger $A^{2+}$ and smaller cations, respectively. The partial nitridation from $ABO_4$ to $ABO_2N$ is accompanied

Received: June 6, 2013
Revised: August 7, 2013
Published: August 8, 2013

by the change of valence of the $B$ cation from 6+ to 5+. In the case of $B$ = W, the $W^{6+}$ ion with the $5d^0$ electron configuration in $AWO_4$ changes to $W^{5+}$ with the $5d^1$ configuration in $AWO_2N$. The $d^0$-to-$d^1$ change would lead to the change of electronic structure and optical properties.

In the sheelite-type $AWO_4$, there exist not only $SrWO_4$ ($A$ = Sr)[27] but also $CaWO_4$[28] and $BaWO_4$[27] ($A$ = Ca and Ba). To our best knowledge, there have been no reports on the synthesis of $CaWO_2N$ and $BaWO_2N$. It is well-known that the $CaWO_4$ and $SrWO_4$ form $Ca_xSr_{1-x}WO_4$ solid solutions ($0 \le x \le 1$).[29,30] However, the $Ca_xSr_{1-x}WO_2N$ solid solutions ($0 < x \le 1$) have not been known yet. The purpose of this work is to investigate the existing phases in the samples obtained by the ammonolysis of $Ca_xSr_{1-x}WO_4$ ($x$ = 0, 0.25, 0.5 and 1). Here, we report novel calcium strontium tungsten oxynitrides $Ca_xSr_{1-x}WO_2N$ ($x$ = 0.25 and 0.5).

$SrWO_2N$ has a cubic $Pm\bar{3}m$ perovskite-type structure[12,13] and exhibits a nearly temperature-independent electrical resistivity (ca. 1 Ω·cm at room temperature).[12] The electron-density distribution and electronic structure of a solid are of vital importance in many fields of chemistry, physics, and materials science.[9,22,31−37] The electron-density distribution of a solid provides the information not only on the details of crystal structure but also on the chemical bonding. Despite their importance, the electron-density distribution and electronic structure of $SrWO_2N$ and $Ca_xSr_{1-x}WO_4$ have not been studied yet. The second purpose of this work is to investigate the electron-density distribution, electronic structure, and crystal structure of $Ca_xSr_{1-x}WO_2N$ ($x$ = 0, 0.25, and 0.5).

## EXPERIMENTAL PROCEDURE

**Synthesis of the Perovskite-Type Calcium Strontium Tungsten Oxynitrides $Ca_xSr_{1-x}WO_2N$.** Precursor materials $Ca_xSr_{1-x}WO_4$ ($x$ = 0, 0.25, 0.5, and 1) with a scheelite-type structure were prepared by solid-state reactions. High-purity powders of $CaCO_3$ (99.9% purity), $SrCO_3$ (99.9% purity), and $WO_3$ (99.9% purity) were mixed and ground for about 2 h in an agate mortar. The mixed powders were pressed into pellets and then heated in air at 900 °C for 12 h. The precursor materials $Ca_xSr_{1-x}WO_4$ ($x$ = 0, 0.25, 0.5, and 1) were confirmed to have a scheelite-type structure[27,38] by X-ray powder diffraction measurements (RINT-2550, Cu $K\alpha$, $2\theta$ range from 10° to 90°, step interval of 0.02°). Rietveld analyses of the X-ray data for $Ca_xSr_{1-x}WO_4$ ($x$ = 0, 0.25, 0.5, and 1.0) were performed using a computer program RIETAN-FP.[39] The refined unit-cell parameters of the scheelite-type $Ca_xSr_{1-x}WO_4$ decreased with Ca content $x$, which indicates the formation of the $Ca_xSr_{1-x}WO_4$ solid solution.

The precursor $Ca_xSr_{1-x}WO_4$ powders ($x$ = 0, 0.25, 0.5, and 1) were heated at 900 °C for 5 h under a continuous ammonia flow (flow rate = 500 cc/min). Figure 1 shows the schematic diagram and photo of the apparatus for the ammonolysis of precursors. The precursor $Ca_xSr_{1-x}WO_4$ powders were white (Figure 2a), whereas the color of the products obtained by heating the precursor $Ca_xSr_{1-x}WO_4$ powders under an ammonia flow was black (Figure 2b). Existing phases in the powders thus obtained were investigated by the RINT-2550 X-ray powder diffractometer. The microstructure and chemical composition of $Ca_xSr_{1-x}WO_2N$ ($x$ = 0, 0.25, and 0.5) were examined by a scanning transmission electron microscope equipped with an energy-dispersive X-ray spectrometer (JEOL JEM-2100F STEM-EDS, 200 kV) and a scanning electron

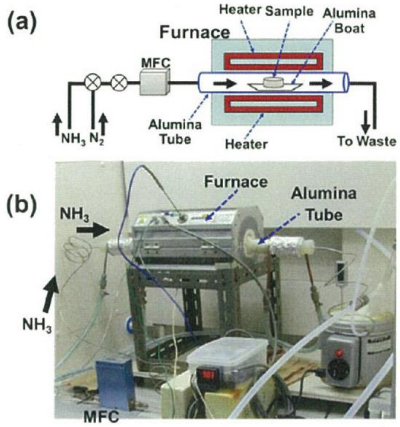


**Figure 1.** (a) Schematic diagram and (b) photo of the apparatus for ammonolysis. MFC: mass flow controller. Black arrows denote the directions of gas flow.

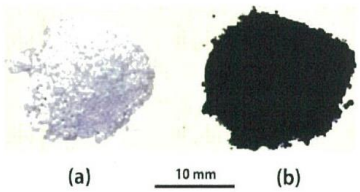


**Figure 2.** Optical images of the $Ca_{0.5}Sr_{0.5}WO_4$ precursor (a) and $Ca_{0.5}Sr_{0.5}WO_2N$ product (b).

microsope (Hitachi High Technologies SU-8000, SEM, 3 kV). For each composition $Ca_xSr_{1-x}WO_2N$, we investigated the electron-diffraction patterns and EDS spectra at eight positions. UV−visible diffuse reflectance data of $Ca_xSr_{1-x}WO_4$ and $Ca_xSr_{1-x}WO_2N$ ($x$ = 0, 0.25, and 0.5) were collected and converted to absorbance using a JASCO V-670 scanning double-beam spectrometer equipped with an integrating sphere (ISN-723) over the spectral range of 200−2500 nm (0.50−6.2 eV). The thermogravimetric (TG, TG-DTA-2020SA-TK18, Bruker AXS) measurements of $SrWO_2N$ were conducted in air at the heating/cooling rate of 10 K/min to investigate its thermal stability.

**Synchrotron X-ray Diffraction Measurements of $Ca_xSr_{1-x}WO_2N$ and Data Processing.** Synchrotron X-ray powder diffraction measurements of $Ca_xSr_{1-x}WO_2N$ ($x$ = 0, 0.25, and 0.5) were performed in air at 301 and 484 K by a high-angular-resolution diffractometer[40] and an electric furnace[41,42] installed at the BL-4B$_2$ beamline of the Photon Factory facility, KEK, Japan. The optical system consisted of a bending-magnet light source, a double-crystal Si(111) monochromator, a focusing cylindrical mirror, a flat specimen rotating at 60 rpm, and the multiple-detector system with a Ge(111) flat analyzer crystal and scintillation counters. The measurement condition was as follows: $2\theta$ range from 10° to 154°, step interval of 0.008°, measurement time of 4−14 s. An ionic chamber monitored the intensity of the incident beam. The asymmetric $2\theta$ scan technique was used for data collection:

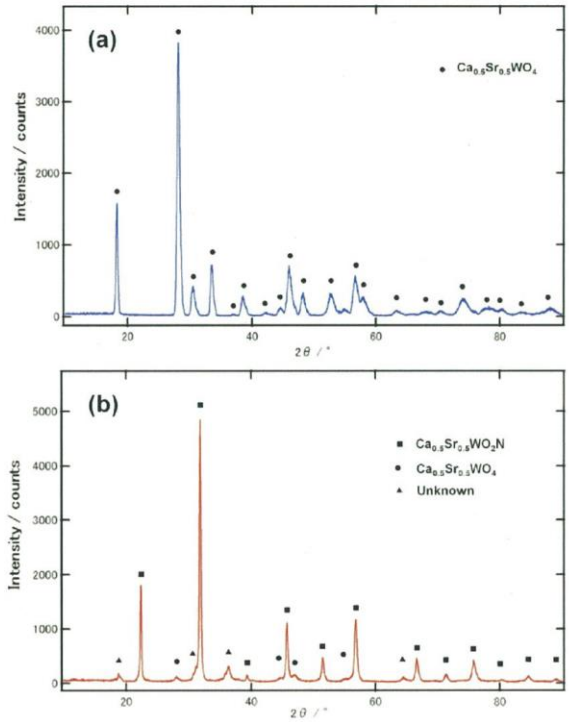


**Figure 3.** X-ray powder diffraction profiles (Cu $K\alpha$, room temperature) of the precursor $Ca_{0.5}Sr_{0.5}WO_4$ (a) and the sample obtained by heating the precursor at 900 °C under an ammonia flow (b). The sample for (b) is identified mainly by the perovskite-type $Ca_{0.5}Sr_{0.5}WO_2N$ (closed squares in panel b). Closed circle in (a, b): $Ca_{0.5}Sr_{0.5}WO_4$, which was identified using the powder diffraction files of $CaWO_4$ (JCPDS No. 41-1431) and $SrWO_4$ (JCPDS No. 08-0490). Closed square in (b): cubic $Pm\bar{3}m$ perovskite-type $Ca_{0.5}Sr_{0.5}WO_2N$, which was identified by the Rietveld analysis. Closed triangle in (b): unknown peak.

The $\theta$ angle was fixed to 7° during the measurement of the whole powder pattern. The wavelength of the synchrotron X-ray was 1.194158(5) Å, which was determined using the 19 peak positions of an NIST SRM640c silicon standard. Rietveld and maximum entropy method (MEM) analyses of the synchrotron data for $Ca_xSr_{1-x}WO_2N$ ($x$ = 0, 0.25, and 0.5) were performed using RIETAN-FP[39] and PRIMA,[43] respectively. The refined crystal structure and electron-density distributions were depicted using the computer program VESTA.[44] The synchrotron X-ray powder diffraction data of $Ca_{0.5}Sr_{0.5}WO_2N$ and $Ca_{0.25}Sr_{0.75}WO_2N$ were also measured by the Debye–Scherrer camera with an imaging plate as a detector,[45] installed at the BL02B2 experimental station of the SPring-8, Hyogo of Japan (see the experimental details in the Supporting Information, section A).

**Neutron Diffraction Data Collection of $Ca_xSr_{1-x}WO_2N$ and Data Processing.** Neutron diffractometry is a powerful tool to refine the occupancy factors of nitrogen and oxygen atoms located at a crystallographic site.[46,47] Neutron powder diffraction measurements of $Ca_xSr_{1-x}WO_2N$ ($x$ = 0, 0.25, and 0.5) were performed using the Echidna neutron powder diffractometer with 128 position sensitive tube detectors installed at the OPAL reactor facility of the Bragg Institute at the Australian Nuclear Science and Technology Organisation (ANSTO).[48] Neutrons with a wavelength of 1.6620(5) Å were obtained from the 335 reflection of a Ge monochromator. The wavelength was determined by the Rietveld analysis of neutron-diffraction data of an NIST alumina standard. Diffraction data were collected in the $2\theta$ range of 5.25–163.95° at intervals of 0.1°. The crystal structures of the $Ca_xSr_{1-x}WO_2N$ ($x$ = 0, 0.25, and 0.5) were refined by the Rietveld method using the computer program RIETAN-FP.[39] The peak shape was assumed to be a modified split-type pseudo-Voigt function with asymmetry and a cutoff value of 7.00. The background profile was approximated by a 12 parameter Legendre polynomial. The unit cell, background, profile shape, and crystal structural parameters were refined simultaneously.

**DFT Calculations of $Ca_xSr_{1-x}WO_2N$ and $Ca_xSr_{1-x}WO_4$.** The ab initio total energy program VASP (Vienna Ab initio Simulation Package)[49,50] was employed for calculation of the valence-electron-density distribution and electron density-of-states (DOS) of single cells or 2 × 2 × 1 supercells of

$Ca_xSr_{1-x}WO_4$ and of 2 × 2 × 2 supercells of cubic $Pm\bar{3}m$ perovskite-type $Ca_xSr_{1-x}WO_2N$ ($x$ = 0, 0.25, and 0.5). Projector augmented-wave (PAW) potentials were used for Ca, Sr, W, O, and N atoms.[51,52] A plane-wave basis set with a cutoff of 500 eV was used. The calculations were performed using the Perdew–Burke–Ernzerhof (PBE) generalized gradient approximation (GGA) for the exchange and correlation functional.[53] Sums over occupied electronic states were performed using the Monkhorst–Pack scheme[54] on a 3 × 3 × 3 or 5 × 5 × 3 set of the $k$-point mesh. The crystallographic parameters refined using synchrotron data of $Ca_xSr_{1-x}WO_2N$ were used as initial parameters in the structural optimization of VASP calculations where the unit-cell parameters were fixed and the positional parameters were relaxed in the structural optimizations. Six 2 × 2 × 2 supercells $(Ca_xSr_{1-x}WO_2N)_8$ with different atomic configurations were optimized. There were stable four models and a little unstable two models. The four structural models resulted in similar valence-electron-density distributions and partial and total density-of-states (DOS). The valence-electron-density distributions were depicted using VESTA.[44]

## ■ RESULTS AND DISCUSSION

**Synthesis and Stability of the Perovskite-Type Oxynitrides $Ca_xSr_{1-x}WO_2N$.** The precursor materials $Ca_xSr_{1-x}WO_4$ ($x$ = 0, 0.25, 0.5, and 1) were identified to be the tetragonal scheelite phase[27,38] (Figure 3a). Unit-cell parameters of the precursor $Ca_xSr_{1-x}WO_4$ materials ($x$ = 0, 0.25, 0.5, and 1) decrease with an increase of Ca content, which indicates that the $Ca_xSr_{1-x}WO_4$ solid solutions are formed. A similar decrease of unit-cell parameters of $Ca_xSr_{1-x}WO_4$ with $x$ was reported also in the literature.[29] The decrease in the cell parameters is attributed to the smaller ionic size of the $Ca^{2+}$ cation compared to $Sr^{2+}$ ($r(Ca^{2+}, 12)$ = 1.34 Å < $r(Sr^{2+}, 12)$ = 1.44 Å). Here, $r(Ca^{2+}, 12)$ stands for the ionic radius of $Ca^{2+}$ with the coordination number of 12 after Shannon.[55]

After heating $CaWO_4$ at 900 °C under an ammonia flow, a tungsten metal W is mainly formed (Figure 4), which suggests

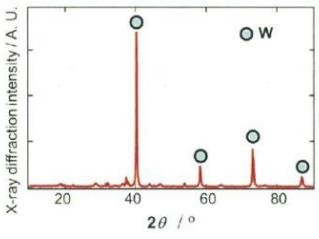


**Figure 4.** X-ray powder diffraction profile (Cu $K\alpha$, room temperature) of the sample obtained by heating the $CaWO_4$ precursor at 900 °C under an ammonia flow. The sample is mainly tungsten metal (circle: tungsten diffraction peak, JCPDS No. 01-1204).

that the mixture of metal tungsten and CaO is more stable than $CaWO_2N$. On the contrary to $CaWO_2N$, the cubic $Pm\bar{3}m$ perovskite-type oxynitrides $Ca_xSr_{1-x}WO_2N$ were successfully prepared for the compositions $x$ = 0, 0.25, and 0.5 as shown by the X-ray, synchrotron X-ray, and neutron powder diffraction patterns (Figures 3b, 5–8). The electron-diffraction patterns from a single domain of $Ca_xSr_{1-x}WO_2N$ ($x$ = 0, 0.25, and 0.5) also indicated the cubic $Pm\bar{3}m$ perovskite-type structure

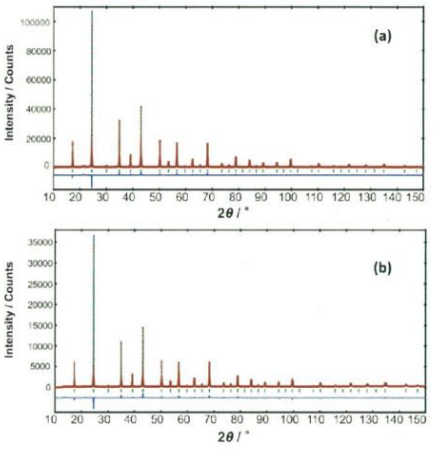


**Figure 5.** Rietveld patterns of the synchrotron X-ray powder diffraction data of the sample obtained by heating the $SrWO_4$ precursor at 900 °C under an ammonia flow, measured in situ at 301 K (a) and at 484 K (b). Green tick marks are Bragg peak positions of cubic $Pm\bar{3}m$ perovskite-type $SrWO_2N$. Blue line at the bottom denotes the difference intensities between the observed and calculated profiles.

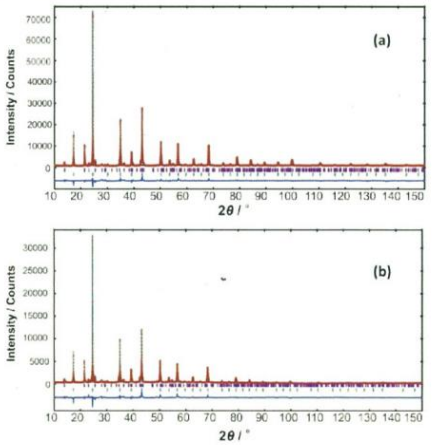


**Figure 6.** Rietveld patterns of the synchrotron X-ray powder diffraction data of the sample obtained by heating the $Ca_{0.25}Sr_{0.75}WO_4$ precursor at 900 °C under an ammonia flow, measured in situ at 301 K (a) and at 484 K (b). Lower green tick marks are Bragg peak positions of cubic $Pm\bar{3}m$ perovskite-type $Ca_{0.25}Sr_{0.75}WO_2N$. Bragg peak positions of minor $Ca_{0.25}Sr_{0.75}WO_4$ phase are shown by the upper violet tick marks. Blue line at the bottom denotes the difference intensities between the observed and the calculated profiles.

$Ca_xSr_{1-x}WO_4$ and of 2 × 2 × 2 supercells of cubic $Pm\bar{3}m$ perovskite-type $Ca_xSr_{1-x}WO_2N$ ($x$ = 0, 0.25, and 0.5). Projector augmented-wave (PAW) potentials were used for Ca, Sr, W, O, and N atoms.[51,52] A plane-wave basis set with a cutoff of 500 eV was used. The calculations were performed using the Perdew–Burke–Ernzerhof (PBE) generalized gradient approximation (GGA) for the exchange and correlation functional.[53] Sums over occupied electronic states were performed using the Monkhorst–Pack scheme[54] on a 3 × 3 × 3 or 5 × 5 × 3 set of the $k$-point mesh. The crystallographic parameters refined using synchrotron data of $Ca_xSr_{1-x}WO_2N$ were used as initial parameters in the structural optimization of VASP calculations where the unit-cell parameters were fixed and the positional parameters were relaxed in the structural optimizations. Six 2 × 2 × 2 supercells $(Ca_xSr_{1-x}WO_2N)_8$ with different atomic configurations were optimized. There were stable four models and a little unstable two models. The four structural models resulted in similar valence-electron-density distributions and partial and total density-of-states (DOS). The valence-electron-density distributions were depicted using VESTA.[44]

## ■ RESULTS AND DISCUSSION

**Synthesis and Stability of the Perovskite-Type Oxynitrides $Ca_xSr_{1-x}WO_2N$.** The precursor materials $Ca_xSr_{1-x}WO_4$ ($x$ = 0, 0.25, 0.5, and 1) were identified to be the tetragonal scheelite phase[27,38] (Figure 3a). Unit-cell parameters of the precursor $Ca_xSr_{1-x}WO_4$ materials ($x$ = 0, 0.25, 0.5, and 1) decrease with an increase of Ca content, which indicates that the $Ca_xSr_{1-x}WO_4$ solid solutions are formed. A similar decrease of unit-cell parameters of $Ca_xSr_{1-x}WO_4$ with $x$ was reported also in the literature.[29] The decrease in the cell parameters is attributed to the smaller ionic size of the $Ca^{2+}$ cation compared to $Sr^{2+}$ ($r(Ca^{2+}, 12)$ = 1.34 Å < $r(Sr^{2+}, 12)$ = 1.44 Å). Here, $r(Ca^{2+}, 12)$ stands for the ionic radius of $Ca^{2+}$ with the coordination number of 12 after Shannon.[55]

After heating $CaWO_4$ at 900 °C under an ammonia flow, a tungsten metal W is mainly formed (Figure 4), which suggests

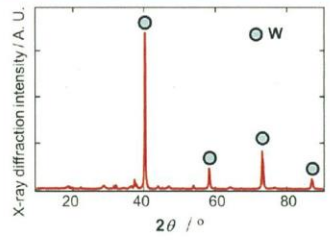


**Figure 4.** X-ray powder diffraction profile (Cu $K\alpha$, room temperature) of the sample obtained by heating the $CaWO_4$ precursor at 900 °C under an ammonia flow. The sample is mainly tungsten metal (circle: tungsten diffraction peak, JCPDS No. 01-1204).

that the mixture of metal tungsten and CaO is more stable than $CaWO_2N$. On the contrary to $CaWO_2N$, the cubic $Pm\bar{3}m$ perovskite-type oxynitrides $Ca_xSr_{1-x}WO_2N$ were successfully prepared for the compositions $x$ = 0, 0.25, and 0.5 as shown by the X-ray, synchrotron X-ray, and neutron powder diffraction patterns (Figures 3b, 5–8). The electron-diffraction patterns from a single domain of $Ca_xSr_{1-x}WO_2N$ ($x$ = 0, 0.25, and 0.5) also indicated the cubic $Pm\bar{3}m$ perovskite-type structure

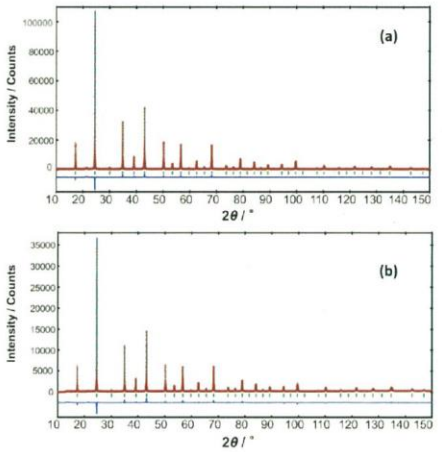


**Figure 5.** Rietveld patterns of the synchrotron X-ray powder diffraction data of the sample obtained by heating the $SrWO_4$ precursor at 900 °C under an ammonia flow, measured in situ at 301 K (a) and at 484 K (b). Green tick marks are Bragg peak positions of cubic $Pm\bar{3}m$ perovskite-type $SrWO_2N$. Blue line at the bottom denotes the difference intensities between the observed and calculated profiles.

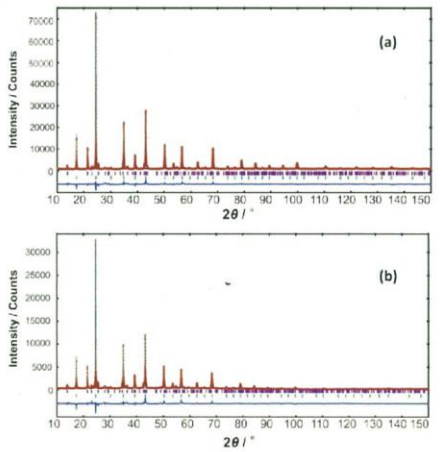


**Figure 6.** Rietveld patterns of the synchrotron X-ray powder diffraction data of the sample obtained by heating the $Ca_{0.25}Sr_{0.75}WO_4$ precursor at 900 °C under an ammonia flow, measured in situ at 301 K (a) and at 484 K (b). Lower green tick marks are Bragg peak positions of cubic $Pm\bar{3}m$ perovskite-type $Ca_{0.25}Sr_{0.75}WO_2N$. Bragg peak positions of minor $Ca_{0.25}Sr_{0.75}WO_4$ phase are shown by the upper violet tick marks. Blue line at the bottom denotes the difference intensities between the observed and the calculated profiles.

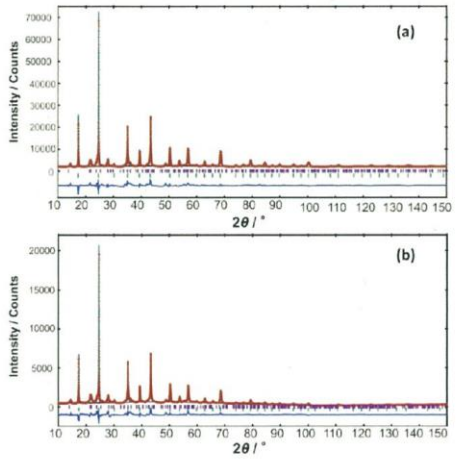


**Figure 7.** Rietveld patterns of the synchrotron X-ray powder diffraction data of the sample obtained by heating the $Ca_{0.5}Sr_{0.5}WO_4$ precursor at 900 °C under an ammonia flow, measured in situ at 301 K (a) and at 484 K (b). Lower green tick marks are Bragg peak positions of cubic $Pm\bar{3}m$ perovskite-type $Ca_{0.5}Sr_{0.5}WO_2N$. Bragg peak positions of minor $Ca_{0.5}Sr_{0.5}WO_4$ phase are shown by the upper violet tick marks. Blue line at the bottom denotes the difference intensities between the observed and the calculated profiles.

(Figure 9) where the nitrogen was detected in the EDS spectra from the domain (Figure S1 in the Supporting Information, section B). The SEM micrographs show that the $Ca_xSr_{1-x}WO_2N$ powders are poorly sintered and aggregated (Figure 10). The sizes of the aggregated particles range from 1 to 10 $\mu$m (Figure 10). The size of a single domain or crystallite is 100–300 nm (Figure 9d, h, l). Fawcett et al.[12] and Weller and Skinner[13] reported the preparation of cubic perovskite-type $SrWO_2N$. In the present work, we successfully synthesized novel oxynitrides $Ca_xSr_{1-x}WO_2N$ ($x$ = 0.25 and 0.5).

Synchrotron X-ray powder diffraction profiles show that $Ca_xSr_{1-x}WO_2N$ materials have the cubic perovskite-type structure and are stable in air at 484 K (Figures 5b, 6b, and 7b). Figure 11 shows that $SrWO_2N$ is stable in air up to about 570 K and oxidized during heating at the rate of 10 K/min in air between 600 and 1110 K.

**Crystal Structure Refinements of $Ca_xSr_{1-x}WO_2N$.** Synchrotron X-ray powder diffraction data of $Ca_xSr_{1-x}WO_2N$ ($x$ = 0, 0.25, and 0.5) measured at 301 and 484 K were analyzed by the Rietveld method on the basis of the cubic $Pm\bar{3}m$ perovskite-type structure (Figures 5–7 and 12a). Rietveld analysis of neutron-powder-diffraction data taken at room temperature was also performed for the cubic $Pm\bar{3}m$ perovskite-type structure (Figure 8). Ca and Sr cations are put at the 1*b* 1/2,1/2,1/2 position. The W atom exists at the 1*a* 0,0,0 position. The O and N anions are put at the 3*d* 1/2,0,0 position. The calculated intensities agree well with observed ones (Table 1, Figures 5–8). The refined unit-cell parameter $a$ decreases with an increase of Ca content $x$ in $Ca_xSr_{1-x}WO_2N$ ($x$ = 0, 0.25, and 0.5) (Figure 13), which indicates the formation of solid solutions $Ca_xSr_{1-x}WO_2N$. Therefore, the W–(O,N) and (Ca,Sr)–(O,N) bond lengths also decrease with Ca content $x$ (W–(O,N) bond length = $a/2$, (Ca,Sr)–(O,N) bond length = $a/\sqrt{2}$). Least-squares fit gives the equation, $a$ = 3.985 − 0.029$x$. The decrease in the $a$ parameter and minus value of the slope (−0.029) are attributed to the smaller size of the Ca cation ($r(Ca^{2+}, 12)$ = 1.34 Å < $r(Sr^{2+}, 12)$ = 1.44 Å). Here, $r(Ca^{2+}, 12)$ stands for the ionic radius of $Ca^{2+}$ with the coordination number of 12 after Shannon.[55] The refined occupancy factor of the nitrogen atom at the 3*d* site $g$(N) was 0.37(6) (Table 1), where the number in the parentheses is the estimated standard deviation in the last digit. EDS results also indicated the existence of the nitrogen atom in $Ca_{0.5}Sr_{0.5}WO_2N$ (see Figure S1 in the Supporting Information, section B). Therefore, the oxygen atom is partially substituted by the nitrogen atom. The bond valence sum (BVS) of the W atom in $Ca_{0.5}Sr_{0.5}WO_2N$ was estimated to be 5.2 using the equation

$$\mathrm{BVS} = \sum (R_0 - r)/0.28$$

where $R_0$ is the average bond valence parameter ($R_0$ = 1.941) and $r$ is the average bond length (1.9843 Å).[56,57] This oxidation number of W (BVS = 5.2) agrees well with that by the chemical composition and electrical neutrality (5.0). These results indicate the $W^{5+}$ ion with the $5d^1$ electron configuration in $Ca_{0.5}Sr_{0.5}WO_2N$, which is different from the $W^{6+}$ ion with the $5d^0$ configuration in $Ca_{0.5}Sr_{0.5}WO_4$.

**Electron-Density Distributions of $Ca_xSr_{1-x}WO_2N$.** To investigate the chemical bonding in $Ca_xSr_{1-x}WO_2N$, we have

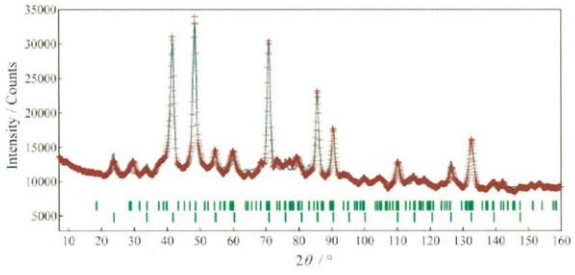


**Figure 8.** Rietveld patterns of the room-temperature neutron-powder-diffraction data of the sample obtained by heating the $Ca_{0.5}Sr_{0.5}WO_4$ precursor at 900 °C under an ammonia flow. Lower tick marks are Bragg peak positions of cubic $Pm\bar{3}m$ perovskite-type $Ca_{0.5}Sr_{0.5}WO_2N$. Bragg peak positions of minor $Ca_{0.5}Sr_{0.5}WO_4$ phase are shown by the upper tick marks.

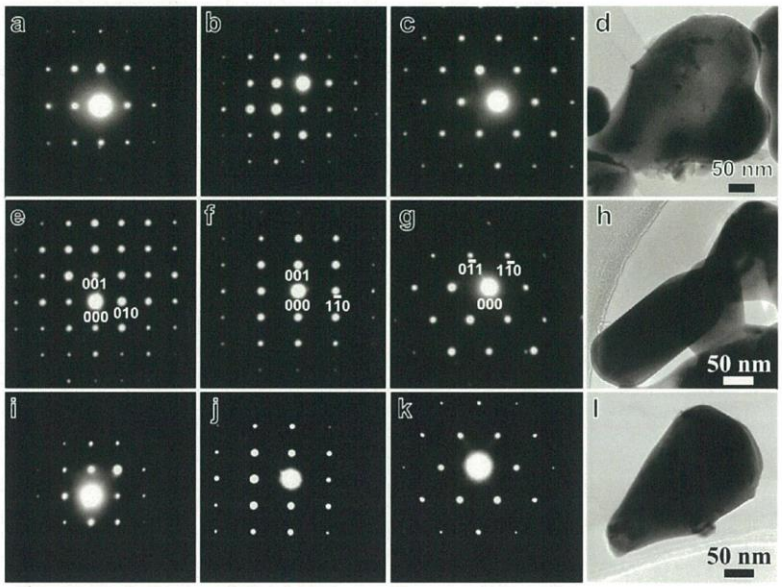


**Figure 9.** Electron-diffraction patterns and TEM micrographs of $SrWO_2N$ (a–d), $Ca_{0.25}Sr_{0.75}WO_2N$ (e–h), and $Ca_{0.5}Sr_{0.5}WO_2N$ (i–l). The patterns of (a–c) were taken from the (d) $SrWO_2N$ particle. The (e–g) were from the (h) $Ca_{0.25}Sr_{0.75}WO_2N$ particle. The (i–k) patterns were from the (l) $Ca_{0.5}Sr_{0.5}WO_2N$ particle. Patterns of (a, e, and i), (b, f, and j), and (c, g, and k) were taken along the ⟨100⟩, ⟨110⟩, and ⟨111⟩ cubic perovskite axes, respectively.

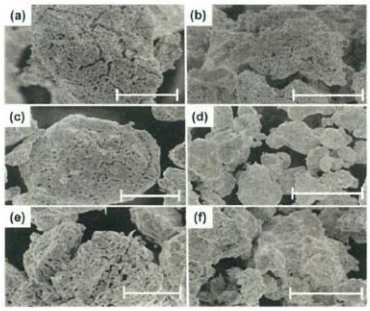


**Figure 10.** SEM micrographs of (a, b) $SrWO_2N$, (c, d) $Ca_{0.25}Sr_{0.75}WO_2N$, and (e, f) $Ca_{0.5}Sr_{0.5}WO_2N$. Scale bar in (a, c, e) = 2 $\mu$m. Scale bar in (b, d, f) = 5 $\mu$m.

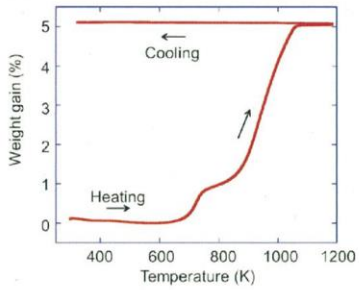


**Figure 11.** TG curve of $SrWO_2N$ in air. Heating and cooling rates are 10 K/min. The weight gain of 5.1 wt % is attributed to the oxidation of $SrWO_2N$ to $SrWO_4$ (calculated weight gain: 5.7 wt %).

performed maximum-entropy-method (MEM) electron-density analysis using the structure factors obtained in the Rietveld analysis of synchrotron powder diffraction data taken at 301 K. Figure 12b shows the continuous electron-density distributions along the W–(O,N) bonds and strongly suggests the partial covalency of W–O and W–N bonds. On the contrary, the electron-density distributions of (Ca,Sr) cations are isolated, which strongly suggests that the (Ca,Sr)–(O,N) bonds are more ionic compared with the W–(O,N) ones. This is the first experimental visualization of the electron-density distribution of $Ca_xSr_{1-x}WO_2N$. Similarly, the La–(O,N) bond is more ionic comparing with the Ti–(O,N) one in $LaTiO_2N$.[22]

These features in the experimental electron-density distribution of $Ca_xSr_{1-x}WO_2N$ (Figure 12b) are observed also in the theoretical valence-electron-density distributions obtained by the density functional theory (DFT)-based calculations (Figure 12c,d). The W–O and W–N bonds are more covalent, whereas the Ca and Sr atoms are more ionic. The average value of the theoretical DFT minimum electron densities at the W–anion

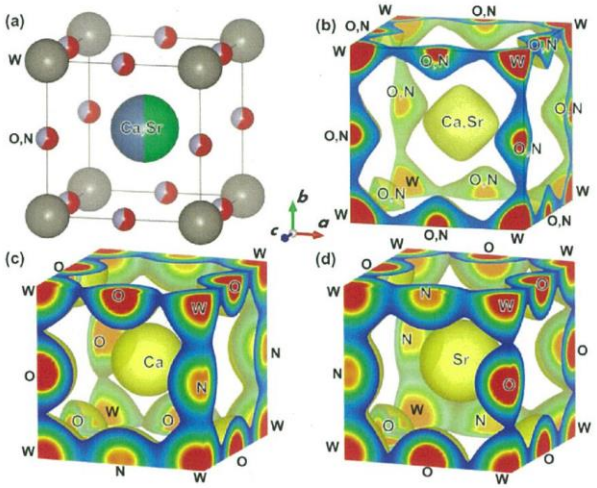


**Figure 12.** (a) Refined crystal structure of $Ca_{0.5}Sr_{0.5}WO_2N$ and (b) experimental MEM electron-density distribution of $Ca_{0.5}Sr_{0.5}WO_2N$. (c, d) Parts of DFT valence-electron-density distributions around a (c) Ca atom and (d) Sr atom.

**Table 1. Refined Crystallographic Parameters and Reliability Factors for Neutron Powder Diffraction Data of $Ca_{0.5}Sr_{0.5}WO_{1.89(18)}N_{1.11(18)}$ Measured at Room Temperature**[a]

| atom | site | $g$ | $x$ | $y$ | $z$ | $U$ Å$^2$ |
|---|---|---|---|---|---|---|
| Ca | 1*b* | 0.5 | 1/2 | 1/2 | 1/2 | 0.044(4) |
| Sr | 1*b* | 0.5 | 1/2 | 1/2 | 1/2 | = $U$(Ca) |
| W | 1*a* | 1.0 | 0 | 0 | 0 | 0.032(3) |
| O | 3*d* | 0.63(6)[b] | 1/2 | 0 | 0 | 0.0260(15) |
| N | 3*d* | 0.37(6)[b] | 1/2 | 0 | 0 | = $U$(O) |

[a]Crystal symmetry: cubic; space group: $Pm\bar{3}m$; unit-cell parameters: $a = b = c = 3.9636(11)$ Å, $\alpha = \beta = \gamma = 90°$, $V = 62.27(2)$ Å$^3$. $g$: occupancy factor. $x$, $y$, $z$: atomic coordinates. $U$: isotropic atomic displacement parameter. Reliability factors: $R_{wp} = 4.48\%$, GoF = 4.90, $R_B = 0.969\%$, $R_F = 0.557\%$. Wavelength = 1.6220 Å. [b]Linear constraint: $g(O) = 1 - g(N)$.

bonds in a supercell $(Ca_{0.5}Sr_{0.5}WO_2N)_8$ (0.87(5) Å$^{-3}$) agrees well with that from the experimental MEM electron-density distribution of $Ca_{0.5}Sr_{0.5}WO_2N$ (0.85 Å$^{-3}$). Here, the number in the parentheses is the standard deviation in the last digit. It is interesting to point out that the minimum electron density at the W–N bond (ex. 1.095(5) Å$^{-3}$ for $(Ca_{0.5}Sr_{0.5}WO_2N)_8$) is higher than that at the W–O one (0.76(7) Å$^{-3}$ for $(Ca_{0.5}Sr_{0.5}WO_2N)_8$), where the number in the parentheses is the standard deviation in all the W–O or W–N bonds of the supercell $(Ca_{0.5}Sr_{0.5}WO_2N)_8$ (Figures 12c,d and 14), which indicates the higher covalency of the W–N bond compared with the W–O one. The higher covalency of the W–N bond is attributable to the smaller electronegativity of the N atom (3.04 (Pauling's scale)) than that of the oxygen atom (3.44). The electronegativity difference between N and W atoms (3.04 − 2.36 = 0.68) is smaller than that between O and W ones (3.44 − 2.36 = 1.08), which leads to the higher covalency of the W–N bond. The different covalency was observed also in a

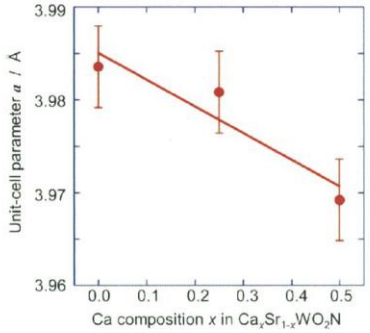


**Figure 13.** Variation of the unit-cell parameter $a$ of the cubic $Pm\bar{3}m$ perovskite-type $Ca_xSr_{1-x}WO_2N$ with Ca composition $x$. Least-squares fit gives the equation, $a = 3.985 - 0.029x$.

perovskite-type $LaTiO_2N$ oxynitride.[22] The Ti–N bond is more covalent than the Ti–O one in $LaTiO_2N$. As shown in the calculated partial density-of-states (DOS in Figures 15 and 16), the covalent W–N bond is formed by the overlap of W 5d and N 2p orbitals. The W–O covalent bond is formed due to the overlapping of W 5d and O 2p orbitals.

**Optical Properties and Electronic Structure of $Ca_xSr_{1-x}WO_2N$.** As described above, the precursor $Ca_xSr_{1-x}WO_4$ powders are white (Figure 2a), whereas the color of the products $Ca_xSr_{1-x}WO_2N$ is black (Figure 2b), which suggests that the insulating $Ca_xSr_{1-x}WO_4$ becomes metallic $Ca_xSr_{1-x}WO_2N$. The UV–visible reflectance spectra of $Ca_xSr_{1-x}WO_4$ and $Ca_xSr_{1-x}WO_2N$ in Figure 17 clearly indicate the insulator-to-metal change from the $Ca_xSr_{1-x}WO_4$ oxide to the $Ca_xSr_{1-x}WO_2N$ oxynitride. This change was confirmed also by the

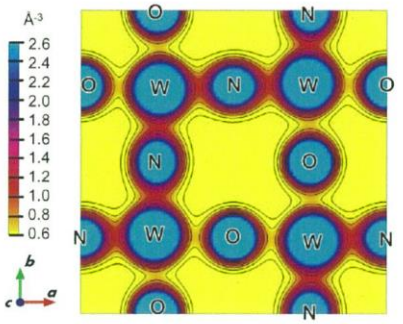


**Figure 14.** DFT valence-electron-density distribution on the *ab* plane at $z = 0.75$ of a $2 \times 2 \times 2$ supercell of cubic $Ca_{0.5}Sr_{0.5}WO_2N$. Contour lines from 0.4 to 2.0 $Å^{-3}$ by the step of 0.2 $Å^{-3}$.

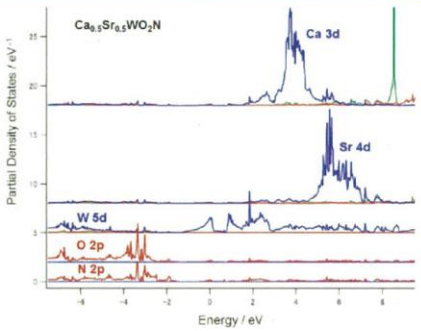


**Figure 15.** Partial density-of-states (DOS) of a $2 \times 2 \times 2$ supercell of cubic $Ca_{0.5}Sr_{0.5}WO_2N$. The blue, red, and green lines stand for the partial DOS of d, p, and s orbitals, respectively.

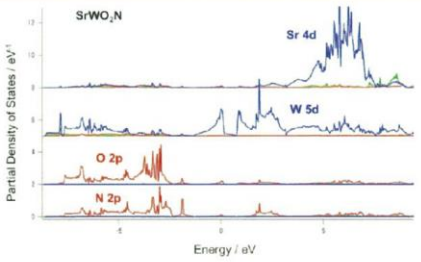


**Figure 16.** Partial density-of-states (DOS) of a $2 \times 2 \times 2$ supercell of cubic $SrWO_2N$. The blue, red, and green lines stand for the partial DOS of d, p, and s orbitals, respectively.

density-of-states (DOS) of $Ca_xSr_{1-x}WO_4$ and $Ca_xSr_{1-x}WO_2N$ (Figures 18 and 19). The DOS of $Ca_xSr_{1-x}WO_2N$ does not change largely with the Ca content $x$ (Figure S2 in the Supporting Information, section C). It should be noted that the electrons around the Fermi level of $Ca_xSr_{1-x}WO_2N$ mainly consist of W 5d ones (Figures 15 and 16), which indicates that

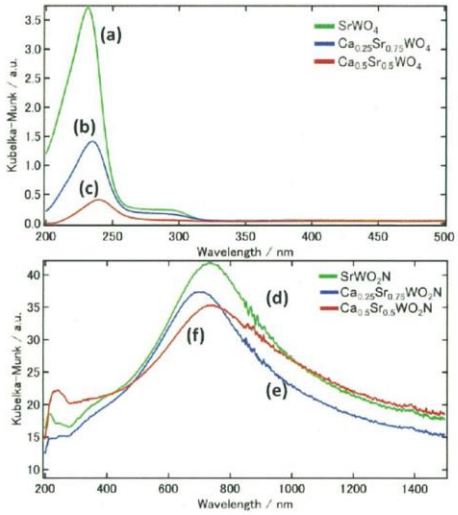


**Figure 17.** UV–vis diffuse reflectance spectra of (a) $SrWO_4$, (b) $Ca_{0.25}Sr_{0.75}WO_4$, (c) $Ca_{0.5}Sr_{0.5}WO_4$, (d) $SrWO_2N$, (e) $Ca_{0.25}Sr_{0.75}WO_2N$, and (f) $Ca_{0.5}Sr_{0.5}WO_2N$.

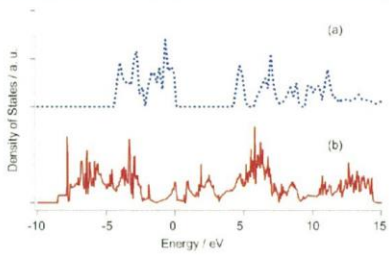


**Figure 18.** Total density-of-states (DOS) of (a) $SrWO_4$ and (b) $SrWO_2N$. Band gap of $SrWO_4$ was estimated to be 4.27 eV.

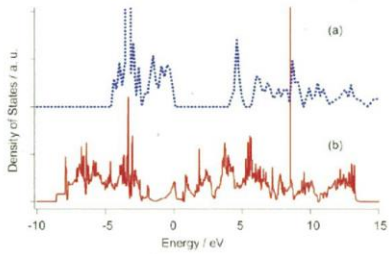


**Figure 19.** Total density-of-states (DOS) of (a) $Ca_{0.5}Sr_{0.5}WO_4$ and (b) $Ca_{0.5}Sr_{0.5}WO_2N$. The band gap of $Ca_{0.5}Sr_{0.5}WO_4$ was estimated to be 4.12 eV.

the metallic state of $Ca_xSr_{1-x}WO_2N$ is attributable to the $W^{5+}$ ion with the $5d^1$ electron configuration. On the contrary,


dx.doi.org/10.1021/jp405597x | J. Phys. Chem. C 2013, 117, 18529–18539

$Ca_xSr_{1-x}WO_4$ is insulating due to the $W^{6+}$ ion with the $5d^0$ electron configuration. Precursor oxides $Ca_xSr_{1-x}WO_4$ with $W^{6+}$ having the $5d^0$ electron configuration are white and insulating, whereas the $Ca_xSr_{1-x}WO_2N$ oxynitrides with the $W^{5+}$ ion having the $5d^1$ configuration are black and exhibit metallic character. These results indicate the insulator−metal transition from the $5d^0$ oxide $Ca_xSr_{1-x}WO_4$ to the $5d^1$ oxynitride $Ca_xSr_{1-x}WO_2N$.

## ■ CONCLUSIONS

We have successfully synthesized the novel $Pm\bar{3}m$ perovskite-type calcium strontium tungsten oxynitrides $Ca_xSr_{1-x}WO_2N$ ($x$ = 0.25 and 0.5) and strontium tungsten oxynitride $SrWO_2N$ by heating the precursor materials $Ca_xSr_{1-x}WO_4$ at 900 °C under an ammonia flow (Figures 1−3 and 5−10). We were not able to prepare the perovskite-type $CaWO_2N$, but metallic tungsten W appeared by heating $CaWO_4$ under the same condition (Figure 4). The crystal and electronic structures, electron-density distribution, and optical properties of $Ca_xSr_{1-x}WO_2N$ and $Ca_xSr_{1-x}WO_4$ ($x$ = 0, 0.25 and 0.5) have been investigated by neutron, synchrotron, and X-ray powder diffraction; TEM-EDS; SEM; UV−visible reflectance measurements; and DFT calculations. The unit-cell parameter $a$ of the cubic perovskite-type $Ca_xSr_{1-x}WO_2N$ decreases with an increase of Ca content $x$ due to the smaller ionic size of $Ca^{2+}$, which indicates the substitution of Ca for Sr (Figure 13). The existence of nitrogen in $Ca_xSr_{1-x}WO_2N$ was confirmed by (1) the refined occupancy factor in the Rietveld analysis of neutron-diffraction data (Table 1) and (2) EDS (Figure S1, Supporting Information). The MEM electron-density analysis combined with the DFT calculations has indicated the W−N and W−O covalent bonds in $Ca_xSr_{1-x}WO_2N$ (Figures 12 and 14), which are formed by the overlapping of W 5d and anion 2p orbitals (Figures 15 and 16). The minimum electron density at the W−N bond is higher than that at the W−O one (Figures 12 and 14), which indicates that the W−N bond is more covalent due to the smaller difference in the electronegativity between W and N atoms compared to the W and O ones. The oxidation number of W in $Ca_xSr_{1-x}WO_2N$ was estimated to be 5.2 by BVS, which indicates the $W^{5+}$ ion with the $5d^1$ electron configuration. Precursor oxides $Ca_xSr_{1-x}WO_4$ with $W^{6+}$ having the $5d^0$ electron configuration are white and insulating, whereas the $Ca_xSr_{1-x}WO_2N$ oxynitrides with the $W^{5+}$ ion having the $5d^1$ configuration are black and exhibit metallic character (Figures 2 and 17−19). Therefore, we have demonstrated the insulator−metal transition from the $5d^0$ oxide $Ca_xSr_{1-x}WO_4$ to the $5d^1$ oxynitride $Ca_xSr_{1-x}WO_2N$ through the partial nitridation. The metallic state of $Ca_xSr_{1-x}WO_2N$ is attributable to the $W^{5+}$ ion with the $5d^1$ electron configuration. On the contrary, $Ca_xSr_{1-x}WO_4$ is insulating due to the $W^{6+}$ ion with the $5d^0$ electron configuration. Therefore, this work has demonstrated that the electrical, optical, and photocatalytic properties of tungsten-containing oxides and oxynitrides can be tailored by changing the valence of the W ion by partial nitridation.

## ■ ASSOCIATED CONTENT

### Supporting Information

EDS spectra of $Ca_xSr_{1-x}WO_2N$ ($x$ = 0, 0.25, and 0.5), the comparison of the density-of-states among $Ca_xSr_{1-x}WO_2N$ ($x$ = 0, 0.25, and 0.5), and synchrotron experimental details. This material is available free of charge via the Internet at http://pubs.acs.org.

## ■ AUTHOR INFORMATION


### Corresponding Author

*E-mail: yashima@cms.titech.ac.jp.


### Notes

The authors declare no competing financial interest.

## ■ ACKNOWLEDGMENTS

The authors would like to thank Prof. T. Ida, Dr. J. Kim, and facility staff for their arrangements and support on the synchrotron- and neutron-diffraction experiments. We thank Mr. T. Sekikawa for experimental assistance and Prof. K. Maeda, Prof. K. Domen, and Dr. K. Fujii for useful discussions. We thank JASCO Co. for the UV−vis measurements. A part of this work was financially supported by the Asahi Glass Foundation, the Ministry of Education, Culture, Sports, Science and Technology of Japan, through a Challenging Exploratory Research No. 25630365 and a Grant-in-Aid for Scientific Research (A) No. 24246107. Travel costs for the neutron experiments of U.F. and K.O. were partly supported by the Japanese Society for Neutron Science. The neutron-diffraction measurements were carried out as projects approved by the Bragg Institute, ANSTO (Proposal Nos. DB2018 and MI2340), which was transferred from (HERMES, JRR-3) with the approval of Institute for Solid State Physics, The University of Tokyo (proposal no. 11729, 11730, 11731, 11732, 11733, 11737), Japan Atomic Energy Agency, Tokai, Japan. The synchrotron experiments were performed as projects approved by the Photon Factory of KEK (Proposal Nos. 2011G185, 2011G640, 2010G144) and by the Japan Synchrotron Radiation Research Institute (JASRI) (Proposal Nos. 2011A1442, 2011B1995, and 2012A1415). Correspondence and requests should be addressed to M.Y.

## ■ REFERENCES


(1) Jin, S.; Tiefel, T. H.; McCormack, M.; Fastnacht, R. A.; Ramesh, R.; Chen, L. H. Thousandfold Change in Resistivity in Magnetoresistive La-Ca-Mn-O Films. *Science* **1994**, *264*, 413−415.

(2) Peña, M. A.; Fierro, J. L. G. Chemical Structures and Performance of Perovskite Oxides. *Chem. Rev.* **2001**, *101*, 1981−2017.

(3) Lufaso, M. S.; Woodward, P. M. Prediction of the Crystal Structures of Perovskites Using the Software Program SPuDS. *Acta Crystallogr., Sect. B* **2001**, *57*, 725−738.

(4) Wang, J.; Neaton, J. B.; Zheng, H.; Nagarajan, V.; Ogale, S. B.; Liu, B.; Viehland, D.; Vaithyanathan, V.; Schlom, D. G.; Waghmare, U. V.; et al. Epitaxial $BiFeO_3$ Multiferroic Thin Film Heterostructures. *Science* **2003**, *299*, 1719−1722.

(5) Yashima, M.; Nomura, K.; Kageyama, H.; Miyazaki, Y.; Chitose, N.; Adachi, K. Conduction Path and Disorder in the Fast Oxide-Ion Conductor $(La_{0.8}Sr_{0.2})(Ga_{0.8}Mg_{0.15}Co_{0.05})O_{2.8}$. *Chem. Phys. Lett.* **2003**, *380*, 391−396.

(6) Pârvulescu, V. I.; Grange, P.; Delmon, B. Catalytic Removal of NO. *Catal. Today* **2004**, *46*, 233−316.

(7) Kobayashi, K.-I.; Kimura, T.; Sawada, H.; Terakura, K.; Tokura, Y. Room-Temperature Magnetoresistance in an Oxide Material with an Ordered Double-Perovskite Structure. *Nature* **2007**, *395*, 677−680.

(8) Chen, Y.-C.; Yashima, M.; Ohta, T.; Ohoyama, K.; Yamamoto, S. Crystal Structure, Oxygen Deficiency and Oxygen Diffusion Path of Perovskite-type Lanthanum Cobaltites $La_{0.4}Ba_{0.6}CoO_{3-\delta}$ and $La_{0.6}Sr_{0.4}CoO_{3-\delta}$. *J. Phys. Chem. C* **2012**, *116*, 5246−5254.

(9) Fujii, K.; Kato, H.; Omoto, K.; Yashima, M.; Chen, J.; Xing, X. Experimental Visualization of the Bi−O Covalency in Ferroelectric Bismuth Ferrite ($BiFeO_3$) by Synchrotron X-ray Powder Diffraction Analysis. *Phys. Chem. Chem. Phys.* **2013**, *15*, 6779−6782.

(10) Marchand, R.; Pors, F.; Laurent, Y. Préparation et Characterisation de Nouveaux Oxynitrures à Structure Perovskite. *Rev. Int. Hautes Temp. Refract.* **1986**, *23*, 11−15.
(11) Bacher, P.; Antoine, P.; Marchand, R.; Lharidon, P.; Laurent, Y.; Roult, G. Time-of-Flight Neutron Diffraction Study of the Structure of the Perovskite-Type Oxynitride $LaWO_{0.6}N_{2.4}$. *J. Solid State Chem.* **1988**, *77*, 67−71.
(12) Fawcett, I. D.; Ramanujachary, K. V.; Greenblatt, M. Synthesis, Structure and Properties of the Oxynitrides $SrWO_2N$ and $SrMoO_{2.5}N_{0.5}$. *Mater. Res. Bull.* **1997**, *32*, 1565−1570.
(13) Weller, M. T.; Skinner, S. J. Neutron and X-Ray Powder Diffraction Studies of the Oxynitrides $SrW(O,N)_3$, $Ba_3W_2(O,N)_8$ and $Ba_3Mo_2(O,N)_8$. *Int. J. Inorg. Mater.* **2000**, *2*, 463−467.
(14) Jansen, M.; Letschert, H. Inorganic Yellow-Red Pigments without Toxic Metals. *Nature* **2000**, *404*, 980−982.
(15) Kasahara, A.; Nukumizu, K.; Hitoki, G.; Takata, T.; Kondo, J. N.; Hara, M.; Kobayashi, H.; Domen, K. Photoreactions on $LaTiO_2N$ under Visible Light Irradiation. *J. Phys. Chem. A* **2002**, *106*, 6750−6753.
(16) Kim, Y.-I.; Lee, E. Constant-Wavelength Neutron Diffraction Study of Cubic Perovskites $BaTaO_2N$ and $BaNbO_2N$. *J. Ceram. Soc. Jpn.* **2011**, *119*, 371−374.
(17) Kim, Y.-I.; Woodward, P. M.; Baba-Kishi, K. Z.; Tai, C. W. Characterization of the Structural, Optical, and Dielectric Properties of Oxynitride Perovskites $AMO_2N$ (A = Ba, Sr, Ca; M = Ta, Nb). *Chem. Mater.* **2004**, *16*, 1267−1276.
(18) Pastrana-Fábregas, R.; Isasi-Marín, J.; Cascales, C.; Sáez-Puche, R. Synthesis, Structure and Magnetic Properties of *R*−W−O−N (*R* = Nd and Eu) Oxynitrides. *J. Solid State Chem.* **2007**, *180*, 92−97.
(19) Moriga, T.; Aoki, D.; Nishida, Y.; Kitaji, K.; Takahara, K.; Murai, K.; Nakabayashi, I. Blue-Shift of Absorption Edge in $LaTiO_2N$ by Controlling the Anion Nonstoichiometry. *Phys. Status Solidi A* **2006**, *203*, 2818−2822.
(20) Logvinovich, D.; Bocher, L.; Sheptyakov, D.; Figi, R.; Ebbinghaus, S. G.; Aguiar, R.; Aguirre, M. H.; Reller, A.; Weidenkaff, A. Microstructure, Surface Composition and Chemical Stability of Partly Ordered $LaTiO_2N$. *Solid State Sci.* **2009**, *11*, 1513−1519.
(21) Ebbinghaus, S. G.; Abicht, H.-P.; Dronskowski, R.; Müller, T.; Reller, A.; Weidenkaff, A. Perovskite-Related Oxynitrides—Recent Developments in Synthesis, Characterisation and Investigations of Physical Properties. *Prog. Solid State Chem.* **2009**, *37*, 173−205.
(22) Yashima, M.; Saito, M.; Nakano, H.; Takata, T.; Ogisu, K.; Domen, K. *Imma* Perovskite-Type Oxynitride $LaTiO_2N$, Structure and Electron Density. *Chem. Commun.* **2010**, *46*, 4704−4706.
(23) Zhang, Y.-R.; Motohashi, T.; Masubuchi, Y.; Kikkawa, S. Local Anionic Ordering and Anisotropic Displacement in Dielectric Perovskite $SrTaO_2N$. *J. Ceram. Soc. Jpn.* **2011**, *119*, 581−586.
(24) Fuertes, A. Chemistry and Applications of Oxynitride Perovskites. *J. Mater. Chem.* **2012**, *22*, 3293−3299.
(25) Maeda, K.; Lu, D.; Domen, K. Oxidation of Water under Visible-Light Irradiation over Modified $BaTaO_2N$ Photocatalysts Promoted by Tungsten Species. *Angew. Chem., Int. Ed.* **2013**, *52*, 6616−6619.
(26) Nilsson, M.; Grins, J.; Käll, P.-O.; Svensson, G. Synthesis, Structural Characterisation and Magnetic Properties of $Gd_{14}W_4O_{33-x}N_y$($0 \le x \le 17 \pm 2$, $0 \le y \le 9 \pm 2$), A New Fluorite-Related Oxynitride. *J. Alloys Compd.* **1996**, *240*, 60−69.
(27) Gürmen, E.; Daniels, E.; King, J. S. Crystal Structure Refinement of $SrMoO_4$, $SrWO_4$, $CaMoO_4$, and $BaWO_4$ by Neutron Diffraction. *J. Chem. Phys.* **1971**, *55*, 1093−1097.
(28) Zhang, Y.; Holzwarth, N. A. W.; Williams, R. T. Electronic Band Structures of the Scheelite Materials $CaMoO_4$, $CaWO_4$, $PbMoO_4$, and $PbWO_4$. *Phys. Rev. B* **1998**, *57S*, 12738−12750.
(29) Cho, W.-S.; Yashima, M.; Kakihana, M.; Kudo, A.; Sakata, T.; Yoshimura, M. Room-Temperature Preparation of Crystallized Luminescent $Sr_{1-x}Ca_xWO_4$ Solid-Solution Films by an Electrochemical Method. *Appl. Phys. Lett.* **1996**, *68*, 137−139.
(30) Longo, V. M.; Orhan, E.; Cavalcante, L. S.; Porto, S. L.; Espinosa, J. W. M.; Varela, J. A.; Longo, E. Understanding the Origin of Photoluminescence in Disordered $Ca_{0.60}Sr_{0.40}WO_4$: An Experimental and First-Principles Study. *Chem. Phys.* **2007**, *334*, 180−188.
(31) Coppens, P.; Stevens, E. D. Accurate X-ray Diffraction and Quantum Chemistry: The Study of Charge Density Distributions. *Adv. Quantum Chem.* **1977**, *10*, 1−35.
(32) Yashima, M.; Yonehara, Y.; Fujimori, H. Experimental Visualization of Chemical Bonding and Structural Disorder in Hydroxyapatite through Charge and Nuclear-Density Analysis. *J. Phys. Chem. C* **2011**, *115*, 25077−25087.
(33) Yashima, M.; Yamada, H.; Nuansaeng, S.; Ishihara, T. Role of $Ga^{3+}$ and $Cu^{2+}$ in the High Interstitial Oxide-Ion Diffusivity of $Pr_2NiO_4$-Based Oxides: Design Concept of Interstitial Ion Conductors through the Higher-Valence $d^{10}$ Dopant and Jahn−Teller Effect. *Chem. Mater.* **2012**, *24*, 4100−4113.
(34) Yashima, M.; Omoto, K.; Chen, J.; Kato, H.; Xing, X. Evidence for (Bi,Pb)−O Covalency in the High $T_C$ Ferroelectric $PbTiO_3$−$BiFeO_3$ with Large Tetragonality. *Chem. Mater.* **2011**, *23*, 3135−3137.
(35) Yashima, M.; Lee, Y.; Domen, K. Crystal Structure and Electron Density of Tantalum Oxynitride, a Visible Light Responsive Photocatalyst. *Chem. Mater.* **2007**, *19*, 588−593.
(36) Yashima, M.; Ogisu, K.; Domen, K. Structure and Electron Density of Oxysulfide $Sm_2Ti_2S_2O_{4.9}$ as a Visible Light Responsive Photocatalyst. *Acta Crystallogr., Sect. B* **2008**, *64*, 291−298.
(37) Yashima, M.; Yamada, H.; Maeda, K.; Domen, K. Experimental Visualization of Covalent Bonds and Structural Disorder in a Gallium Zinc Oxynitride Photocatalyst $(Ga_{1-x}Zn_x)(N_{1-x}O_x)$, Origin of Visible Light Absorption. *Chem. Commun.* **2010**, *46*, 2379−2381.
(38) Kay, M. I.; Frazer, B. C.; Almodovar, I. Neutron Diffraction Refinement of $CaWO_4$. *J. Chem. Phys.* **1964**, *40*, 504−506.
(39) Izumi, F.; Momma, K. Three-Dimensional Visualization in Powder Diffraction. *Solid State Phenom.* **2007**, *130*, 15−20.
(40) Toraya, H.; Hibino, H.; Ohsumi, K. A New Powder Diffractometer for Synchrotron Radiation with a Multiple-Detector System. *J. Synchrotron Radiat.* **1996**, *3*, 75−84.
(41) Yashima, M.; Tanaka, M.; Oh-uchi, K.; Ida, T. A Compact Furnace for Synchrotron Powder Diffraction Measurements up to 1807 K. *J. Appl. Crystallogr.* **2005**, *38*, 854−855.
(42) Yashima, M.; Oh-uchi, K.; Tanaka, M.; Ida, T. A Compact Furnace for Synchrotron Powder Diffraction Experiments up to 1800 K. *J. Am. Ceram. Soc.* **2006**, *89*, 1395−1399.
(43) Izumi, F.; Dilanian, R. A. Structure Refinement Based on the Maximum-Entropy Method from Powder Diffraction Data. *Recent Res. Dev. Phys.* **2002**, *3*, 699−726.
(44) Momma, K.; Izumi, F. VESTA 3 for Three-Dimensional Visualization of Crystal, Volumetric and Morphology Data. *J. Appl. Crystallogr.* **2011**, *44*, 1272−1276.
(45) Nishibori, E.; Takata, M.; Kato, K.; Sakata, M.; Kubota, Y.; Aoyagi, S.; Kuroiwa, Y.; Yamakata, M.; Ikeda, N. The Large Debye−Scherrer Camera Installed at SPring-8 BL02B2 for Charge Density Studies. *Nucl. Instrum. Methods Phys. Res., Sect. A* **2001**, *467*−*468*, 1045−1048.
(46) Yashima, M.; Maeda, K.; Teramura, K.; Takata, T.; Domen, K. Crystal Structure and Optical Properties of $(Ga_{1-x}Zn_x)(N_{1-x}O_x)$ Oxynitride Photocatalyst ($x = 0.13$). *Chem. Phys. Lett.* **2005**, *416*, 225−228.
(47) Yashima, M.; Maeda, K.; Teramura, K.; Takata, T.; Domen, K. Crystal Structure Analysis of $(Ga_{0.93}Zn_{0.07})(N_{0.90}O_{0.10})$ Oxynitride Photocatalyst. *Mater. Trans.* **2006**, *47*, 295−297.
(48) Liss, K.-D.; Hunter, B.; Hagen, M.; Noakes, T.; Kennedy, S. Echidna—The New High-Resolution Powder Diffractometer Being Built at OPAL. *Physica B* **2006**, *385*−*386*, 1010−1012.
(49) Kresse, G.; Hafner, J. *Ab Initio* Molecular Dynamics for Liquid Metals. *Phys. Rev. B* **1993**, *47*, R558−R561.
(50) Kresse, G.; Furthmuller, J. Efficient Iterative Schemes for *Ab Initio* Total-Energy Calculations using a Plane-Wave Basis Set. *Phys. Rev. B* **1996**, *54*, 11169−11186.

(51) Kresse, G.; Joubert, D. From Ultrasoft Pseudopotentials to the Projector Augmented-Wave Method. *Phys. Rev. B* **1999**, *59*, 1758–1775.
(52) Blöchl, P. E. Projector Augmented-Wave Method. *Phys. Rev. B* **1994**, *50*, 17953–17979.
(53) Perdew, J.; Burke, K.; Ernzerhof, M. Generalized Gradient Approximation Made Simple. *Phys. Rev. Lett.* **1996**, *77*, 3865–3868.
(54) Monkhorst, H. J.; Pack, J. D. Special Points for Brillouin-Zone Integrations. *Phys. Rev. B* **1976**, *13*, 5188–5192.
(55) Shannon, R. D. Revised Effective Ionic Radii and Systematic Studies of Interatomic Distances in Halides and Chalcogenides. *Acta Crystallogr., Sect. A* **1976**, *32*, 751–767.
(56) Hong, Q. M.; Zhou, Z. H.; Hu, S. Z. Study on the Bond Valence Parameters for Tungsten-Oxygen Bonds. *Acta Chim. Sin. B* **2004**, *62*, 1733–1737.
(57) Brese, N. E.; O'Keeffe, M. Bond Valence Parameters for Solids. *Acta Crystallogr., Sect. B* **1991**, *47*, 192–197.

## ■ NOTE ADDED AFTER ASAP PUBLICATION

After this paper was published ASAP on August 27, 2013, a correction was made to the Acknowledgments. The corrected version was reposted August 29, 2013.

Journal of Alloys and Compounds 658 (2016) 147–151

Contents lists available at ScienceDirect

Journal of Alloys and Compounds

journal homepage: http://www.elsevier.com/locate/jalcom

# Enhancement of photoluminescence intensity and structural change by doping of $P^{5+}$ ion for $Ca_{2-x/2}(Si_{1-x}P_x)O_4:Eu^{2+}$ green phosphor

Shohei Furuya [a], Hiromi Nakano [a, *], Nobuyuki Yokoyama [a], Hiroki Banno [b, c], Koichiro Fukuda [b]

[a] Department of Environmental and Life Sciences, Toyohashi University of Technology, Toyohashi 441-8580, Japan
[b] Department of Materials Science and Engineering, Nagoya Institute of Technology, Nagoya 466-8555, Japan
[c] Research Fellow of Japan Society for the Promotion of Science, Japan

ARTICLE INFO

*Article history:*
Received 1 May 2015
Accepted 19 October 2015
Available online 22 October 2015

*Keywords:*
Oxide materials
Solid state reactions
Optical properties
Crystal structure
X-ray diffraction

ABSTRACT

The study of P-doped $Ca_2SiO_4$ ($C_2S$) structure has demonstrated that the incorporation of P effectively stabilizes the high-temperature phases. In this work, we synthesize a series of $(Ca_{2-x/2-y}Eu_y\square_{x/2})(Si_{1-x}P_x)O_4$ ($0 \le x \le 0.20$, $0.02 \le y \le 0.05$) green-light emitting phosphors and discuss the influence of P concentration on the luminescence intensity and structural change of the host material. The phosphor is synthesized by a solid–state reaction and heated at 498 K for 6 h, and then at 1273 K for 8 h in air. Doping of $Eu^{2+}$ is achieved by annealing the $Eu_2O_3$-containing materials at 1473 K for 3 h under a 90% $N_2$–10% $H_2$ reductive atmosphere. A phosphor with $x = 0.04$ and $y = 0.03$ shows the highest PL intensity, which is obviously higher than that of the P-free phosphor ($x = 0$) due to the structural change of the host material.



## 1. Introduction

Rare-earth doped dicalcium silicate ($Ca_2SiO_4$, $C_2S$) phosphors have been investigated for application to white LEDs [1,2]. The silicate family is an attractive material as a host material of the phosphor, since it has high chemical and thermal stability in the water-free environments and is available at low cost. Two types of phosphors have been reported: one is $Eu^{3+}$-doped $C_2S$ phosphor, and the other is $Eu^{2+}$-doped one. The former type emits red light due to the transition of $^5D_0$–$^7F_2$ for the $Eu^{3+}$ ion [3]. The red emission color was almost the same in the various host materials due to the f–f transition of the $Eu^{3+}$ ion. In general, the $Eu^{2+}$-doped $C_2S$ phosphor is useful for a wide range of applications, and the wavelength of the emission can be controlled by the structure and/or composition of the host material because of the f-d transition of the $Eu^{2+}$ ion. Recently, a crystal-site engineering technique has been reported to customize the luminescence color of the dicalcium silicate phosphor [4]. Green-yellow light emission was caused by a transition ($4f^7 \rightarrow 4f^65d^1$) of the $Eu^{2+}$ ion at the Ca site [2]. In the β-$C_2S$ structure (space group $P2_1/n$), there are two polyhedral calcium sites [5]. The phase composition at ambient temperature changes from β to $\alpha'_L$-$C_2S$ when a relatively large amount of Eu ion is doped in the $C_2S$. With increasing Eu-ion content, the red-light emission could be attributed to the transition of the $Eu^{2+}$ ion and the emission was strongly related to the peculiar coordination environments of $Eu^{2+}$ in the two types of Ca sites [4]. The phase-composition change from β to $\alpha'_L$-$C_2S$ also occurs by doping of Sr or P ions in the $C_2S$, which is related to the cell size [6–8]. Study of the P-doped $C_2S$ structure has demonstrated that the incorporation of P effectively stabilizes the high-temperature phases [8]. However, the relationship between photoluminescence (PL) intensity and crystal structure of P-doped $C_2S$ has not yet been clarified.

In the present study, we synthesized a series of $Ca_{2-x/2}(Si_{1-x}P_x)O_4:Eu^{2+}$ green-light emitting phosphors and discussed the influence of P concentration on the luminescence intensity and structural change of the host material.

## 2. Experimental procedure

The starting materials used were $CaCO_3$, $SiO_2$, $CaHPO_4 \cdot 2H_2O$, and $Eu_2O_3$ (>99.9% grade) to prepare the $Eu^{2+}$-doped $C_2S$ phosphors. The powders were weighted stoichiometrically in molar ratios of [Ca: Eu: Si: P] = [1.98−$x$/2: 0.02: 1−$x$: $x$] with $x$ from 0 to 0.2, corresponding to the general formula $(Ca_{1.98-x/2}Eu_{0.02}\square_{x/2})$

* Corresponding author.
*E-mail address:* hiromi@crfc.tut.ac.jp (H. Nakano).

http://dx.doi.org/10.1016/j.jallcom.2015.10.172
0925-8388/

$(Si_{1-x}P_x)O_4$. In the formula of $(Ca_{1.98-y}Eu_y\square_{0.02})(Si_{1.96}P_{0.04})O_4$, the powders were weighted in molar ratios of [Ca: Eu: Si: P] = [1.98−$y$: $y$: 1.96: 0.04] with $y$ = 0.02, 0.03, 0.04 and 0.05. These powders were thoroughly mixed with a small amount of acetone in a planetary ball mill (Pulverisette P-6, Fritsch, Germany). The materials were subsequently pressed into pellets, heated at 498 K for 6 h, 973 K for 2 h, and then at 1273 K for 8 h in air. Doping of $Eu^{2+}$ has been achieved by annealing the $Eu_2O_3$-containing materials at 1473 K for 3 h under a 90% $N_2$–10% $H_2$ reductive atmosphere.

Phase identification was made based on the X-ray powder diffraction (XRPD) data (CuKα), which were obtained on a RINT 2500 device (Rigaku Co., Ltd., Japan) operated at 40 kV and 200 mA. The phase compositions were determined from the X-ray profile intensity data (CuKα$_1$) collected on another diffractometer in the 2$\theta$ range of 25.0°–43.0° (X'Pert PRO Alpha-1, PANalytical B.V., Almelo, the Netherlands) operated at 45 kV and 40 mA. The intensity data were examined by the Rietveld method [9] using the computer program RIETAN-FP [10]. We quantitatively determined the phase compositions of the samples using the phase-analysis method based on Brindley's procedure [11], the subroutine of which was implemented in the program.

Excitation and emission spectra were obtained using a spectrometer (model FP-6500, JASCO). Quantum efficiency was measured by a spectral radiometer (model MCPD-7000, Otsuka Electronics Co., Ltd., Osaka, Japan).

## 3. Results and discussion

### 3.1. Photoluminescence property

We focused our investigation on the effect of the $P^{5+}$ ion on phosphors with a composition of $(Ca_{1.98-x/2}Eu_{0.02}\square_{x/2})(Si_{1-x}P_x)O_4$ ($0 \le x \le 0.20$) as a host material. Fig. 1 shows PL spectra of the phosphors with various P content. The excitation spectra, monitored at around 505 nm, appeared broad in the wavelength range of 250–450 nm. The broad excitation spectrum is composed of four bands at 310 nm, 340 nm, 360 nm and 400 nm, which is attributed to the location of the $Eu^{2+}$ ion at two different sites in the $Ca_2SiO_4$ lattice [2,12]. A green-light emission, excited at around 336 nm, was observed in the range from 450 to 580 nm. The spectrum is composed of two spectra at 502 nm and 523 nm, which is attributed to the transition of the $Eu^{2+}$ ion to the ground state [2]. Table 1 shows the chromaticity ($x$, $y$) of the phosphors with various P content. The chromaticity ($x$, $y$) is slightly different, and this might be related to the structural change of host materials.

Next, the optimal Eu concentration was determined for the composition of $(Ca_{1.98-y}Eu_y\square_{0.02})(Si_{1.96}P_{0.04})O_4$. Fig. 2 shows the excitation and emission spectra of the phosphors with various Eu contents. In the range of Eu concentration from 2 to 5 at%, all phosphors emitted green color and the optimal concentration was 3 at%.

Fig. 3 summarizes the relationship between PL intensity and P ($x$) content in $(Ca_{2-x/2-y}Eu_y\square_{x/2})(Si_{1-x}P_x)O_4$ with $Eu^{2+}$ ($y$) at 0.02, 0.03, 0.04 and 0.05. The emission or excitation wavelengths shown were measured by monitoring them at maximum wavelengths. The results reveal that the phosphor with $x$ = 0.04 and $y$ = 0.03 exhibited the highest PL intensity, which was about eight times higher than that of the P-free phosphor ($x$ = 0, $y$ = 0.02).

### 3.2. Phase identification

In order to determine the relationship between PL intensity and structure, structural analysis was performed using XRD patterns before and after annealing under a 90% $N_2$–10% $H_2$ reductive atmosphere at 1473 K for 3 h. Figs. 4 and 5 show the XRD patterns of

**Table 1**
Chromaticity ($x$, $y$) of the phosphors with compositions of $(Ca_{1.98-x/2}Eu_{0.02}\square_{x/2})(Si_{1-x}P_x)O_4$.

| P Content ($x$ value) | $x$ | $y$ |
|---|---|---|
| 0 | 0.222 | 0.508 |
| 0.01 | 0.217 | 0.530 |
| 0.04 | 0.222 | 0.528 |
| 0.06 | 0.220 | 0.528 |
| 0.1 | 0.218 | 0.507 |
| 0.2 | 0.207 | 0.486 |

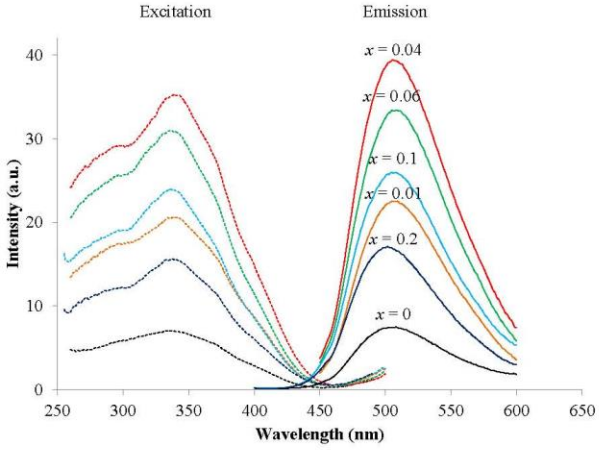


**Fig. 1.** Emission and excitation spectra of $(Ca_{1.98-x/2}Eu_{0.02}\square_{x/2})(Si_{1-x}P_x)O_4$ phosphor with $P^{5+}$ ($x$) at 0, 0.01, 0.04, 0.06, 0.1 and 0.2.

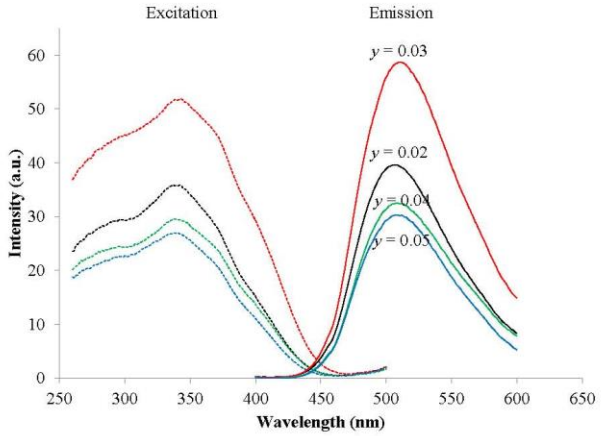


**Fig. 2.** Emission and excitation spectra of $(Ca_{1.98-y}Eu_y\square_{0.02})(Si_{1.96}P_{0.04})O_4$ phosphor with $Eu^{2+}$ ($y$) at 0.02, 0.03, 0.04 and 0.05.

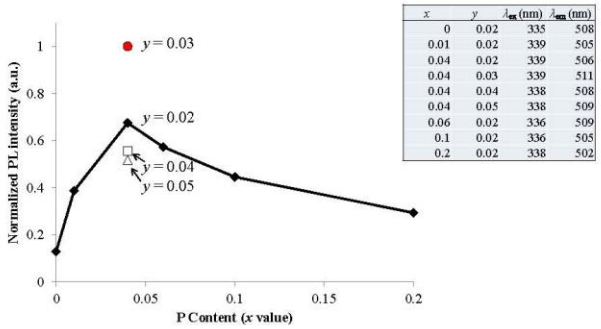


| $x$ | $y$ | $\lambda_{ex}$ (nm) | $\lambda_{em}$ (nm) |
|---|---|---|---|
| 0 | 0.02 | 335 | 508 |
| 0.01 | 0.02 | 339 | 505 |
| 0.04 | 0.02 | 339 | 506 |
| 0.04 | 0.03 | 339 | 511 |
| 0.04 | 0.04 | 338 | 508 |
| 0.04 | 0.05 | 338 | 509 |
| 0.06 | 0.02 | 336 | 509 |
| 0.1 | 0.02 | 336 | 505 |
| 0.2 | 0.02 | 338 | 502 |

**Fig. 3.** Relationship between PL intensity and P ($x$) content in $(Ca_{2-x/2-y}Eu_y\square_{x/2})(Si_{1-x}P_x)O_4$ with $Eu^{2+}$ ($y$) at 0.02, 0.03, 0.04 and 0.05. The emission or excitation wavelengths shown were measured by monitoring them at maximum wavelengths.

phosphors with various P content in the composition of $(Ca_{1.98-x/2}Eu_{0.02}\square_{x/2})(Si_{1-x}P_x)O_4$ before and after annealing, respectively. The before- and after-annealing structures were almost the same. Before annealing, no bright emission was observed by irradiation of UV-light. This implies that the $Eu^{3+}$ ion was reduced to the $Eu^{2+}$ ion after annealing without the structural change. The structure of the P-free phosphor ($x = 0$) was of the β-phase of $C_2S$. By doping of the P ion, the $\alpha'_L$-phase appeared and the amount of it increased with increasing P content in the host material. With doping $x = 0.06$, $Ca_5P_2SiO_{12}$ appeared obviously as a second phase. The structural transition from the β- to $\alpha'_L$-phase of $C_2S$ has been reported, and high-temperature modifications were stabilized by doping of the P ion [8]. Sato et al. reported that the structural transition β-phase→$\alpha'_L$-phase in the $Ca_{2-x}Eu_xSiO_4$ system occurs with a large amount of Eu ion between $x = 0.1$ and 0.2 [4]. In the case of (CaSr)$SiO_4$:$Eu^{2+}$, an enhancement of PL intensity was observed by doping of Sr ion in the host material due to the existence of the $\alpha'_L$-phase [13,14]. In this case, therefore, the $\alpha'_L$-phase should be stabilized by doping of a small amount of P and Eu ions. The results reveal that enhancement of PL intensity is caused by the appearance of the $\alpha'_L$-phase of $C_2S$. However, the PL intensity decreased gradually when the second phase of $Ca_5P_2SiO_{12}$ appeared.

Fig. 6 shows the XRD patterns of phosphors with various Eu content in the composition of $(Ca_{1.98-y}Eu_y\square_{0.02})(Si_{1.96}P_{0.04})O_4$ after annealing under a reductive atmosphere at 1473 K for 3 h. The structures were composed of the β-phase and $\alpha'_L$-phase of $C_2S$, and those structures were almost the same. Therefore, all phosphors emitted green color in the range of Eu concentration from 2 to 5 at%.

### 3.3. Phase compositions

We investigated the profile intensity data of the phosphor samples with $y = 0.02$, $x = 0$, 0.04 and 0.1 by the Rietveld method and determined the phase compositions, the structural parameters of which were taken from those reported by Jost et al. [15] for β-$C_2S$,

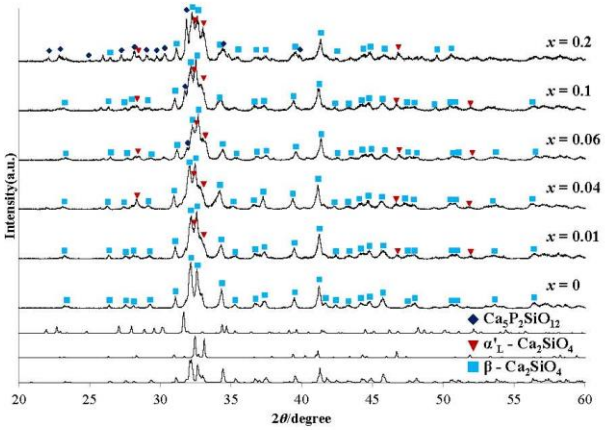


**Fig. 4.** XRD patterns of $(Ca_{1.98-x/2}Eu_{0.02}\square_{x/2})(Si_{1-x}P_x)O_4$ phosphor with $P^{5+}$ ($x$) at 0, 0.01, 0.04, 0.06, 0.1 and 0.2 before annealing under reducing atmosphere.

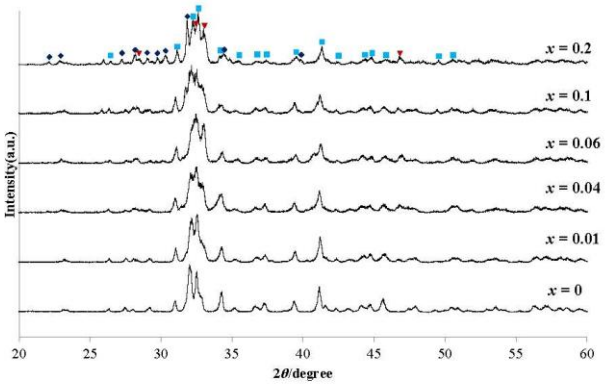


**Fig. 5.** XRD patterns of $(Ca_{1.98-x/2}Eu_{0.02}\square_{x/2})(Si_{1-x}P_x)O_4$ phosphor with $P^{5+}$ ($x$) at 0, 0.01, 0.04, 0.06, 0.1 and 0.2 after annealing under reducing atmosphere.

Udagawa et al. [16] for $\alpha'_L$-$C_2S$, and Dickens and Brown [17] for $Ca_5P_2SiO_{12}$. The sample with $x = 0$ was found to be composed exclusively of the β-phase (Fig. 7(a)). Each of the other samples, with $x = 0.04$ (Fig. 7(b)) and 0.1 (Fig. 7(c)), was made up of both β- and $\alpha'_L$-phases with a small amount of $Ca_5P_2SiO_{12}$. The phase composition of the former sample was, under the condition of effective particle radii being 5.00 μm, 82.9 mol% β, 14.5 mol% $\alpha'_L$ and 2.6 mol% $Ca_5P_2SiO_{12}$, and that of the latter was 68.3 mol% β, 27.7 mol% $\alpha'_L$ and 4.0 mol% $Ca_5P_2SiO_{12}$. With an increasing impurity phase of $Ca_5P_2SiO_{12}$ by doping of the P ion, the PL intensity clearly decreased. The results of phase composition analysis revealed that the coexistence of the $\alpha'_L$-phase and β-phase is effective for the enhancement of PL intensity. A more detailed structural analysis and theoretical calculations in this respect will be performed in the near future. We tentatively conclude that such small differences in the lattice site (site symmetry, lattice strain, bonding, etc.) would affect the emission energy of the $Eu^{2+}$ ions.

## 4. Conclusion

We succeeded in synthesizing a series of green-light emitting phosphors of $(Ca_{2-x/2-y}Eu_y\square_{x/2})(Si_{1-x}P_x)O_4$ with $x$-values ranging from 0 to 0.20 and $y$-values from 0.02 to 0.05. The phosphors were prepared by a solid–state reaction and heated at 498 K for 6 h, and then at 1273 K for 8 h in air. Doping of $Eu^{2+}$ has been achieved by annealing the $Eu_2O_3$-containing materials at 1473 K for 3 h under a 90% $N_2$–10% $H_2$ reductive atmosphere. The phosphor with composition of $\{Ca_{1.95}Eu_{0.03}\square_{0.02}\}\{Si_{1.96}P_{0.04}\}O_4$ showed the highest PL intensity, about eight times higher than that of the P-free phosphor ($x = 0$, $y = 0.02$) due to the structural change of the host material. The phase change of $\beta \rightarrow \alpha'_L$ was induced by doping of $P^{5+}$ and $Eu^{2+}$ ions in the crystal structure of $C_2S$. The results of phase composition analysis revealed that the coexistence of the $\alpha'_L$-phase and β-phase provided enhancement of PL intensity due to the effective environment of the $Eu^{2+}$ ion in the crystal structure.

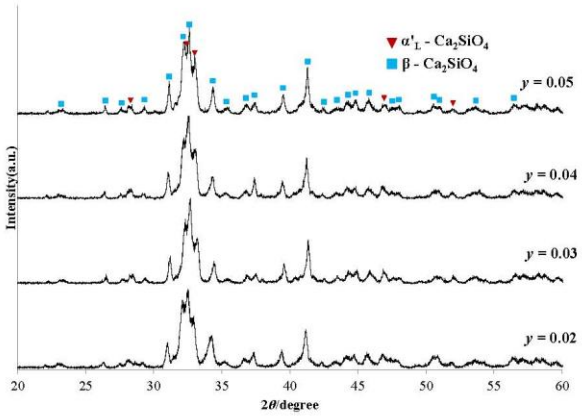


**Fig. 6.** XRD patterns of $(Ca_{1.98-y}Eu_y\square_{0.02})(Si_{1.96}P_{0.04})O_4$ phosphor with $Eu^{2+}$ ($y$) at 0.02, 0.03, 0.04 and 0.05 after annealing under reducing atmosphere.

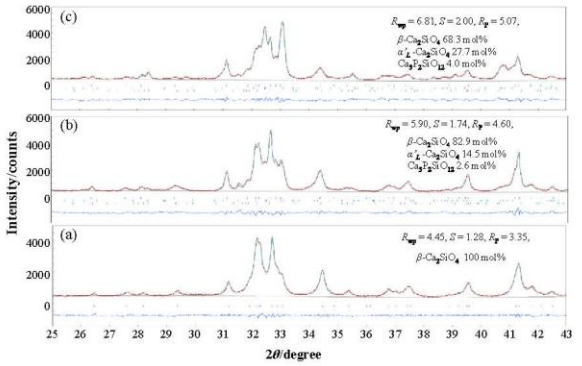


**Fig. 7.** Observed profile intensities (red symbol: +), the fitted patterns (green solid lines), and the difference curves (blue solid lines in lower part of diagrams) obtained from the phosphor samples with $y = 0.02$, $x =$ (a) 0, (b) 0.04 and (c) 0.1. The positions of possible Bragg reflections are indicated by vertical bars. (For interpretation of the references to color in this figure legend, the reader is referred to the web version of this article.)

## Acknowledgment

This work was partially supported by a Grant-in-Aid for Scientific Research (c) No. 25420709 (H. N.) by the Japan Society for the Promotion of Science and the 45th Kazuchika Okura Memorial Foundation.

## References

[1] S.-W. Choi, S.-H. Hong, J. Am. Ceram. Soc. 92 (9) (2009) 2025–2028.
[2] Y.Y. Luo, D.S. Jo, K. Senthil, S. Tezuka, M. Kakihana, K. Toda, T. Masaki, D.H. Yoon, J. Solid State Chem. 189 (2012) 68–74.
[3] Y. Zhang, J. Chen, Y. Li, H.J. Seo, Opt. Mater. 37 (2014) 525–530.
[4] Y. Sato, H. Kato, M. Kobayashi, T. Masaki, D.-H. Yoon, M. Kakihana, Angew. Chem. Int. Ed. 53 (2014) 7756–7759.
[5] K. Fukuda, I. Maki, S. Ito, J. Am. Ceram. Soc. 79 (11) (1996) 2925–2928.
[6] K. Fukuda, I. Maki, S. Ito, J. Am. Ceram. Soc. 79 (10) (1996) 2577–2581.
[7] K. Fukuda, I. Maki, S. Ito, J. Am. Ceram. Soc. 79 (11) (1996) 2969–2970.
[8] K. Fukuda, I. Maki, S. Ito, T. Miyake, J. Ceram. Soc. Jpn. 105 (2) (1997) 117–121.
[9] H.M. Rietveld, Acta Crystallogr. 22 (1967) 151–152.
[10] F. Izumi, K. Momma, Solid State Phenom. 130 (2007) 15–20.
[11] G.W. Brindley, Philos. Mag. 36 (1945) 347–369.
[12] K. Mori, R. Kiyanagi, M. Yonemura, K. Iwase, T. Sato, K. Ito, M. Sugiyama, T. Kamiyama, T. Fukunaga, J. Solid State Chem. 179 (2006) 3286–3294.
[13] W.J. Park, Y.H. Song, D.H. Yoon, Mater. Sci. Eng. B 173 (2010) 76–79.
[14] S. Tezuka, Y. Sato, T. Komukai, Y. Takatsuka, H. Kato, M. Kakihana, J. App. Phys. 6 (2013) 072101.
[15] K.H. Jost, B. Ziemer, R. Seydel, Acta Crystallogr. B33 (1977) 1696–1700.
[16] S. Udagawa, K. Urabe, T. Yano, K. Takada, M. Natsume, Chem. Assoc. Jpn. Rev. Gen. Meet. Tech. Sess. 33 (1979) 35–37.
[17] B. Dickens, W.E. Brown, Tschermaks Min. Petr. Mitt. 16 (1971) 1–27.